COMPUTER SIMULATION OF MOLECULAR SHAPE TRANSITIONS IN ADSORBED POLYMERS UNDER CONFINEMENT CONDITIONS

By

Jessica Elena Harrison

A thesis submitted in partial fulfillment
of the requirements for the degree of
Master of Science (MSc) in Chemical Sciences

The Faculty of Graduate Studies
Laurentian University
Sudbury, Ontario, Canada

THESIS DEFENCE COMMITTEE/COMITÉ DE SOUTENANCE DE THÈSE
Laurentian Université/Université Laurentienne
Faculty of Graduate Studies/Faculté des études supérieures

Title of Thesis
Titre de la thèse: COMPUTER SIMULATION OF MOLECULAR SHAPE TRANSITIONS IN ADSORBED POLYMERS UNDER CONFINEMENT CONDITIONS

Name of Candidate
Nom du candidat: Harrison, Jessica

Degree
Diplôme: Master of Science

Department/Program
Département/Programme: Chemical Sciences

Date of Defence
Date de la soutenance August 28, 2017

APPROVED/APPROUVÉ

Thesis Examiners/Examinateurs de thèse:

Dr. Gustavo Arteca
(Supervisor/Directeur(trice) de thèse)

Dr. Joy Gray-Munro
(Committee member/Membre du comité)

Dr. Jeff Shepherd
(Committee member/Membre du comité)

Dr. René Fournier
(External Examiner/Examinateur externe)

Approved for the Faculty of Graduate Studies
Approuvé pour la Faculté des études supérieures
Dr. David Lesbarrères
Monsieur David Lesbarrères
Dean, Faculty of Graduate Studies
Doyen, Faculté des études supérieures

ACCESSIBILITY CLAUSE AND PERMISSION TO USE

Abstract

The structural and dynamical properties of polymer-covered surfaces under confinement and crowding effects are key to many applications. Earlier work showed the occurrence of "escape transitions" in small uncompressed clusters (or "islands") even for repulsive polymers. These transitions involve a switch from evenly-compact configurations ("trapped chains"), to uneven compactness ("escaped chains"). Here, we address a complementary question: if the crowding is reduced by having fewer neighbours, can an external compression produce "escaped configurations"? To this end, we focused on the confinement of grafted polymers. At low compression, the inter-chain entanglement increases with excluded volume as chains swell and interpenetrate, up to a critical chain length where the behaviour is reversed. We conclude that, when few chains are present or if a larger ensemble of them is arranged symmetrically, compression induces chain avoidance without inducing escape transitions. The switch in mechanism depends mostly on crowding, and not on the applied pressure.

Keywords

Polymer islands, Monte Carlo simulations, self-avoiding walks, radius of excluded volume, escape transition, chain avoidance, entanglement complexity, coarse-grained, hard-sphere potential, Marsaglia algorithm, Metropolis-Hasting algorithm.

Acknowledgements

I would like to thank everyone for the help and support that they have provided throughout this research project. Firstly, I would like to express my deepest gratitude to my supervisor, Dr. Gustavo Arteca, for allowing me to do my graduate thesis in his lab. I am extremely grateful to him for his guidance, support, and patience that he has extended to me throughout this project.

I would like to thank my lab mates, Laura Laverdure and Michael Richer, for their advice and friendship. I will cherish our time spent in the lab and am so grateful for all the memories.

I would like to thank my thesis evaluation committee, Dr. Jeffrey Shepherd and Dr. Joy Gray-Munro. Thank you for your time and for providing constructive criticism on different aspects of my project. I would like to thank as well Dr. René Fournier, from York University, for his valuable suggestions and comments, acting as my external examiner.

I would like to thank the Chemistry and Biochemistry department for bestowing the Father Allaire scholarship, as well as the Henrik and Regina Waern bursary. In addition, I would like to thank Laurentian University for providing financial support through the graduate teaching assistantship.

I would especially like to thank my friends. Thank you for all your input and patience throughout this project, as well as just helping me relax and stay sane.

Finally, I would like to thank my family for their unceasing support and encouragement. Thank you for all the love and motivation.

Table of Contents

Abstract iii
Acknowledgements iv
Table of Contents v
List of Figures vii
List of Tables xiii
List of Appendices xiii
List of Abbreviations and Symbols xiv
Chapter 1 1
1. Introduction 1
1.1. Introduction to Polymer Chemistry 1
1.2. Applications of Polymer Covered Surfaces 5
1.3. Effect of Solvent and Temperature on Polymeric Brushes 7
1.3.1. Polymers in Solution 7
1.3.2. Theta (Θ) Temperature 8
1.4. Statistical Ensembles 10
1.5. Simulation Methods for the Investigation of Polymer Structure 12
1.5.1. Overview of Molecular Dynamics Simulation 12
1.5.2. Overview of Monte Carlo Simulation 14
1.6. Motivation and Organization of Thesis Objectives 15
1.6.1. Escape Transitions and Previous Research Conducted by our Lab 15
1.6.2. Objectives and Organization of this Thesis 18
Chapter 2 20
2. Methodology 20
2.1. Monte Carlo Simulations of Coarse-grained Polymer Islands 20
2.1.1. Coarse-grained Polymer Models 20
2.1.2. Overview of Excluded Volume and Self-Avoiding Walks 22
2.1.3. Metropolis-Hastings Algorithm 24
2.1.4. Marsaglia's Algorithm 26
2.2. Molecular Shape Descriptors 27
2.2.1. Polymer Chain Mean Size 27
2.2.2. Chain Anisometry 28
2.2.3. Chain Entanglement Complexity 29
2.3. Detailed Models and Algorithms used in this Thesis 32

2.3.1. Polymer Model.....32
2.3.2. Computational Details.....37
2.4. Configurational Search: A Summary.....41
Chapter 3.....42
3. Results.....42
3.1. Two Chains Under Compression.....42
3.2. Effect of Lateral Displacement on the Compression of Two Chains.....50
3.3. Two Chains with Different Length and Excluded Volume Under Compression.....56
3.4. Three Chains Under Compression.....62
3.5. Seven Chains Under Compression.....70
Chapter 4.....77
4. Summary of Observations and Further Discussion.....77
4.1. Two Chains Under Compression.....77
4.2. Two Shifted Chains Under Compression.....79
4.3. Two Chains with Different Length and Composition Under Compression.....80
4.4. Three Chains Under Compression.....82
4.5. Seven Chains Under Compression.....84
Chapter 5.....86
5. Conclusions and Further Work.....86
References.....89
Appendices.....98
Appendix 1: Monte Carlo Trajectory Generating Program.....98
Appendix 2: Molecular Shape Analysis Program.....108
Appendix 3: Inter-chain Entanglement Calculations Program Code.....122
Appendix 4: Two Chains Under Compression for Model in Figure 12.....135
Appendix 5: Two Shifted Chains Under Compression for Model in Figure 13.....137

List of Figures

Figure 1: Classification of polymers 2

Figure 2: Skeletal structure representation of a few different polymer architectures. Adapted from [Young & Lovell, 2011] 3

Figure 3: Transition between polymer "mushroom" and "brush" regimes. Adapted from [Brittain & Minko, 2007] 5

Figure 4: Lubrication between two surfaces. The diagram illustrates the microscopic role of the polymer with the gap. Adapted from [Haw & Mosey, 2012] 7

Figure 5: Example configuration of a single grafted homopolymer in 'good' and 'poor' solvent conditions. Adapted from [Arteca et al., 2001] 8

Figure 6: Schematic representation of an excluded volume interaction between two non-bonded monomer beads *i* and *j* in a self-avoiding walk model. The distance r_{ij} must be larger than r_{ex} for the configuration to be accepted 23

Figure 7: Schematic representation of a Markov chain. The process begins at State 1 and moves to State 2. The step is accepted and continues moving forward to State 3. If a criterion is not met for the new configuration at State 3, the configuration is rejected and restarts from State 2 25

Figure 8: Monte Carlo method to build a chain by using Marsaglia's algorithm to perform random sampling over the configurational space. A new bead position is located randomly on the unit circle. The accepted position "3" must also satisfy the excluded-volume condition to bead "1", *i.e.*, $||\bar{r}_3 - \bar{r}_1|| > r_{ex}$ 26

Figure 9: Schematic representation for the computation of the radius of gyration. The polymer configuration is specified by the monomer positions with respect to the centre of mass of the polymer chain. The three size descriptors h_{ee}, R_e, and R_g have the same statistical characteristics, but R_g has the smoother behaviour (i.e., less noise due to configurational space) 28

Figure 10: Schematic representation of chain asphericity. A polymer chain can adopt either an oblate (flattened, left) configuration, or a prolate (elongated, right) configuration. Prolate configurations are typical of high density brushes with repulsive interactions and no confinement. Oblate shape may appear in low-density brushes with repulsive and attractive interactions under compression 29

Figure 11: Schematic representation of projections that produce one overcrossing. In the right-hand side diagram, the overcrossing segments are closer to each other and yield a larger mean overcrossing number. Adapted from [Arteca et al., 2001b] 31

Figure 12: Two chains under compression. (The snapshot corresponds to n = 50 monomer beads, r_{ex} = 0.3Å, and constant bond length l =1.50Å) 32

Figure 13: Two shifted chains under compression (for n = 50 monomer beads, r_{ex} = 0.5Å, D = 8Å, and constant bond length l =1.50Å) 33

Figure 14: Two chains with different length and excluded volume under compression (for n_1 = 50 monomer beads (bottom), n_2 = 30 monomer beads (top), and constant bond length l =1.50Å) 34

Figure 15: Three chain packing geometries, A) linear, B) triangular. The black circles represent the anchor beads for the two chains on the top plane, while the green circle is the anchors for the bottom chain 35

Figure 16: Sliding simulation with three chains in a "linear" geometrical arrangement (*cf*. Figure 16), n = 50 beads per chain, r_{ex} = 0.5Å, D = 6Å, D' = 3Å 36

Figure 17: Model used for seven chains under compression. This representative snapshot corresponds to h = 15Å, n = 20 beads per chain, r_{ex} = 0.4Å, D = 10Å and l = 1.50Å 37

Figure 18: Input data file for the Monte Carlo trajectory generating program (Appendix 1)..... 38

Figure 19: Two chain plots of rejection versus r_{ex} for, A) various plate separation distances at n = 50 beads per chain, B) different number of beads per chain at h = 15Å. Observe that chain length has a bigger effect on rejection than confinement. Note that n > 50 beads cannot be handled at high confinement and excluded volume with the algorithms used in this thesis..... 40

Figure 20: Comparison of r_{ex} on asphericity [left] and radius of gyration [right] of n = 50 beads per chain at h = 15Å (high compression). The results are averaged over the two present chains, one grafted to each corresponding plate (model in Figure 12). Swelling causes the polymer chains to become more elongated in shape and expand in size 45

Figure 21: Comparison of r_{ex} on inter-chain [left] and intra-chain [right] entanglements at n = 50 beads per chain and h = 15Å (high compression). Swelling causes a polymer chain to untangle with itself, as well as with the neighbour chain on the top plane (model in Figure 12) 46

Figure 22: Effect of varying chain length, n, and r_{ex} on the inter-chain entanglement for the model of two grafted chains directly opposite to each other (model in Figure 12), [left] h = 30Å (low compression), and the [right] h = 15Å (high compression) 47

Figure 23: Effect of various plate separations (h) on inter-chain entanglement at n = 50 beads per chains (model in Figure 12) 48

Figure 24: Effect of compression on radius of gyration [left] and intra-chain entanglement [right], at n = 50 beads per chain (model in Figure 12) 49

Figure 25: Comparison of r_{ex} on radius of gyration [left] and inter-chain entanglement [right] for two sliding chains n = 50 beads at h = 15Å (model in Figure 13). The structural inserts illustrate typical shapes for different r_{ex} and D values. The inserts A) and B) correspond to r_{ex} = 1.0Å, while C) and D) correspond to r_{ex} = 0.5Å 52

Figure 26: Effect of r_{ex} on inter-chain entanglement at n = 50 beads per chain and h = 15Å (model in Figure 13)..... 53

Figure 27: Shear displacement trends at different chain lengths, n, on inter-chain entanglement at h = 15Å, for, n = 40 [left], n = 30 [right], (model in Figure 13). Note that the crossover effect for inter-chain entanglement disappears, for a given compression value, if the chains are sufficiently short..... 54

Figure 28: Comparing the effect of shearing of shorter chains at higher compression, n = 40 at h = 10Å [left], to longer chains at smaller compression, n = 50 at h = 15Å [right] on inter-chain entanglement (model in Figure 13). Note that short and long chains have approximately the same entanglement behaviour with their neighbour if the compression level is adjusted properly. 55

Figure 29: Comparison of two chains with different lengths, n_1 = 50 and n_2 = 20 beads, with the same r_{ex} on inter-chain entanglement at h = 15Å. The notation [30+30] and [20+20] refer to two systems, one with n_1 = 30 and n_2 = 30, and the other with n_1 = 20 and n_2 = 20, respectively, where n_1 refers to the bottom chain and n_2 to the top chain (model in Figure 14).....58

Figure 30: Comparison of two different chain lengths, n_1 = 50 and n_2 = 30 beads, with the same r_{ex} on inter-chain entanglement at h = 15Å. Note that [40+40] and [30+30] refers to two systems, one with n_1 = 40 and n_2 = 40, and the other with n_1 = 30 and n_2 = 30, respectively, where n_1 refers to the bottom chain and n_2 to the top chain (model in Figure 14).....59

Figure 31: Comparison of two different chain lengths, n_1 = 50 and n_2 = 40 beads, with the same r_{ex} on inter-chain entanglement at h = 15Å. Note that [50+50] and [40+40] refers to two systems, one with to n_1 = 50 and n_2 = 50, and the other with n_1 = 40 and n_2 = 40, respectively, where n_1 refers to the bottom chain and n_2 to the top chain (model in Figure 14).....60

Figure 32: Comparison of two different chain lengths, n_1 = 50 and n_2 = 30 beads, with different r_{ex} on inter-chain entanglement at h = 15Å. The results are rather inconclusive, given the large statistical noise and configurational fluctuations. However, it is clear that there is a range of chain lengths and excluded volumes where two chains with different length and excluded volume can produce equivalent levels of inter-chain entanglement 61

Figure 33: Individual chain shape properties for three chains (n = 50 beads) under compression (h = 15Å) in linear geometry (see insert), [on the left] radius of gyration, [on the right] intra-chain entanglement. D' = 3Å. (model in Figure 15). Recall, $O_{3,Bottom}$ = (0,D,0), $O_{1,Top}$ = (0,0,h), and $O_{2,Top}$ = (0,D',h), where D is varied 65

Figure 34: Individual chain shape properties for three chains (n = 50 beads) under compression (h = 15Å) in triangular geometry, [on the left] radius of gyration, [on the right] intra-chain entanglement. D' = 3Å (model in Figure 15). Recall, $O_{3,Bottom}$ = (D,0,0), $O_{1,Top}$ = (0,-D'/2,h), and $O_{2,Top}$ = (0,+D'/2,h), where D is varied.....66

Figure 35: Inter-chain entanglement trends between chains 1 and 2 for three chains (n = 50 beads) under compression (h = 15Å), [on the left] linear geometry, [on the right] triangular geometry. D' = 3Å (model Figure 15). Recall that "Linear" is characterized by $O_{3,Bottom}$= (0,D,0), $O_{1,Top}$= (0,0,h), and $O_{2,Top}$= (0,D',h); while "Triangular" corresponds to $O_{3,Bottom}$= (D,0,0), $O_{1,Top}$= (0,-D'/2,h), and $O_{2,Top}$= (0,+D'/2,h), where D is varied.....67

Figure 36: Inter-chain entanglement trends between chains 1 and 3 for three chains (n = 50 beads) under compression (h = 15Å), [on the left] linear geometry, [on the right] triangular geometry. $D' = 3Å$ (model Figure 15). Recall that "Linear" is characterized by $O_{3,Bottom}$= (0,D,0), $O_{1,Top}$= (0,0,h), and $O_{2,Top}$= (0,D',h); while "Triangular" corresponds to $O_{3,Bottom}$= (D,0,0), $O_{1,Top}$= (0,-D'/2,h), and $O_{2,Top}$= (0,+D'/2,h), where D is varied.....68

Figure 37: Inter-chain entanglement trend between chains 2 and 3 for three chains (n = 50 beads) under compression (h = 15Å) for linear geometry. D' = 3Å. Despite the statistical noise and configurational fluctuations, we can clearly observe a region of D and r_{ex} values that produce a maximum in inter-chain entanglements 69

Figure 38: Schematic of the uncompressed seven polymer chain model. This model provides a reference to compare the results for the two-plane system in Figure 17. (The left-hand side diagram shows the anchor geometry on the bottom plane and the model variable D) 70

Figure 39: Average radius of gyration over seven chains, n = 20 beads per chain, uncompressed chains and chains compressed at h = 15Å. (Note that the "compressed" system corresponds to the model in Figure 17, while the "uncompressed" state corresponds to the system in Figure 38) 73

Figure 40: Average asphericity over seven chains, n = 20 beads per chain, uncompressed chains and chains compressed at h = 15Å. (Note that the "compressed" system corresponds to the model in Figure 17, while the "uncompressed" state corresponds to the system in Figure 38) 74

Figure 41: Average intra-chain entanglement over seven chains, n = 20 beads per chain, uncompressed chains and chains compressed at h = 15Å. (Note that the "compressed" system corresponds to the model in Figure 17, while the "uncompressed" state corresponds to the system in Figure 38).....75

Figure 42: Average inter-chain entanglement over the six bottom chains with chain 1, n = 20 beads per chain, uncompressed chains and chains compressed at h = 15Å. (Note that the "compressed" system corresponds to the model in Figure 17, while the "uncompressed" state corresponds to the system in Figure 38).....76

Figure 43: Schematic representation of the effect of chain length and r_{ex} on inter-chain entanglement (model in Figure 14) 82

Figure 44: Asphericity of n = 50 beads per chain at various plate separation distances (model in Figure 12) 135

Figure 45: Radius of gyration of n = 50 beads per chain at h = 15Å at different r_{ex}-values (model in Figure 13) 137

Figure 46: Asphericity of n = 50 beads per chain at h = 15Å at different r_{ex}-values (model in Figure 13) 138

Figure 47: Intra-chain entanglement of n = 50 beads per chain at h = 15Å at different r_{ex}-values (model in Figure 13) 138

Figure 48: Inter-chain entanglement for two chains n = 20 beads per chain and h = 15Å, as a function of their relative displacement (model in Figure 13) 138

Figure 49: Inter-chain entanglement for two chains n = 30 beads per chain and h = 10Å, as a function of their relative displacement (model Figure 13). 138

List of Tables

Table 1: Comparing inter-chain entanglements $\langle \overline{N}_{inter} \rangle_{1,2}$ and $\langle \overline{N}_{inter} \rangle_{1,3}$, when chain (3) is directly between chains (1 and 2), for the two geometries shown in Figure 15, (*i.e.*, "Linear" and "Triangular") displayed with the 95% confidence intervals 64

List of Appendices

Appendix 1: Monte Carlo Trajectory Generating Program 98

Appendix 2: Molecular Shape Analysis Program 108

Appendix 3: Inter-chain Entanglement Calculations Program Code 122

Appendix 4: Two Chains Under Compression for Model in Figure 13 135

Appendix 5: Two Shifted Chains Under Compression for Model in Figure 14 137

List of Abbreviations and Symbols

Ω	Asphericity (*i.e.*, mean deviation from spheroidal shape)
l	Bond length (measured in Ångström, Å)
CPU	Central Processing Unit
D	Distance away from origin (*i.e.*, shear displacement)
$\overline{N}_{\text{inter}}$	Inter-chain entanglement complexity (*i.e.*, mean overcrossing number for bonds between chains with different length and excluded volume)
$\overline{N}_{\text{intra}}$	Intra-chain entanglement complexity (*i.e.*, mean overcrossing number for bonds within a chain)
MD	Molecular Dynamics
MC	Monte Carlo
n	Number of beads per chain (*i.e.*, chain length)
h	Plate separation (*i.e.*, the distance between the grafting and compression planes)
PEG	Polyethylene Glycol
PVC	Polyvinyl Chloride
r_{ex}	Radius for the excluded volume interaction
R_g	Radius of gyration (*i.e.*, mean chain size)
SAW	Self-avoiding walk

Chapter 1

1. Introduction

1.1. Introduction to Polymer Chemistry

Polymers are made of small structural subunits (or monomers) which are connected by covalent bonds via polymerization reactions, thereby resulting in structures with large molecular weights [Flory, 1953], [Vollhardt & Schore, 2011]. The term 'polymer' is applied to an enormous assortment of materials which can have drastically different structure, and thus, diverse properties or function. Although the structure of polymers varies greatly, with respect to structural subunits, polymers may typically possess either one particular type of monomer (*i.e.*, homopolymers) or combinations of a limited number of different monomers (*i.e.*, heteropolymers) [Flory, 1953]. To differentiate the vast array of polymers into smaller categories, we can use several different conventions based on the methods of polymerization and the chemical nature of the monomer units. The method of polymerization will influence the polymer length and its topology (*e.g.*, a linear or ring polymer, a dendrimer, a grafted polymer, etc.). The dominant interaction between monomers will influence, on the other hand, its size and shape [Arteca, 1996a]. In this thesis, we contribute to understanding some aspects of how the shape of a polymer is determined by the underlying interaction and constraints imposed by available space and the presence of neighbouring chains. An important caveat is that a polymer may belong to several of the categories; each category represents a method of studying or comparing polymers (see **Figure 1**).

Polymers are ubiquitous; we find natural biopolymers such as DNA, proteins, cellulose, as well as materials such as wool and silk [Vollhardt & Schore, 2011]. The antithesis of natural polymers are synthetic polymers, such as nylon, polyethylene, polyester, Teflon, epoxy, and resins [Vollhardt & Schore, 2011]. We also find semi-synthetic polymers altered or modified from natural sources. Some examples are cellulose acetate (rayon), cellulose nitrate (nitrocellulose), and volcanized rubber [Vollhardt & Schore, 2011].

Polymers can also be classified in terms of the intermolecular forces involved and can be divided into four sub-categories, **Figure 1**. The first type are *elastomers*, *i.e.*, polymers that can easily return to their original shape after an applied force is removed [Misra, 1993]. The reason is simple: chains are held together by weak intermolecular forces, and they can be easily

stretched (or untangled) by applying a small stress. As the stress is removed, they relax and regain their original shape. A representative example of elastomers is natural rubber.

The second type are *fibers* which exhibit strong intermolecular interactions (*e.g.*, hydrogen bonds or dipole-dipole interactions between chains) [Misra, 1993]. In this case, the chains can be packed together closely (possibly including cross-linking between chains); the resulting fiber shows a typically large tensile strength and less elasticity. Some examples of fibers include Nylon 66, dacron, and silk, which can be used to produce thin thread woven into fabric [Misra, 1993].

The third type are *thermoplastics*. These polymers can be repeatedly softened and hardened by subjecting them to cycles of heating and cooling ([Hull and Clyne, 1996], [Harper, 2002]). In thermoplastics, the intermolecular forces are intermediate in strength to those found in elastomers and fibers; typically, there is no cross-linking. When heated, thermoplastics become more fluid and thus can be molded and then cooled to get a desired product shape. Examples of thermoplastics include polyethylene, polystyrene, polyvinyl chloride (PVC), and Teflon [Hull and Clyne, 1996].

The final type are the *thermosetting polymers*. Upon heating, these species undergo a permanent change which makes them very hard and impossible to melt. When heated, thermosetting polymers cross-link extensively, which renders them permanently rigid and very strong materials [Harper, 2002]. Some examples include epoxy resins, phenolic resins, melamine formaldehyde, and polyester resin. [Harper, 2002].

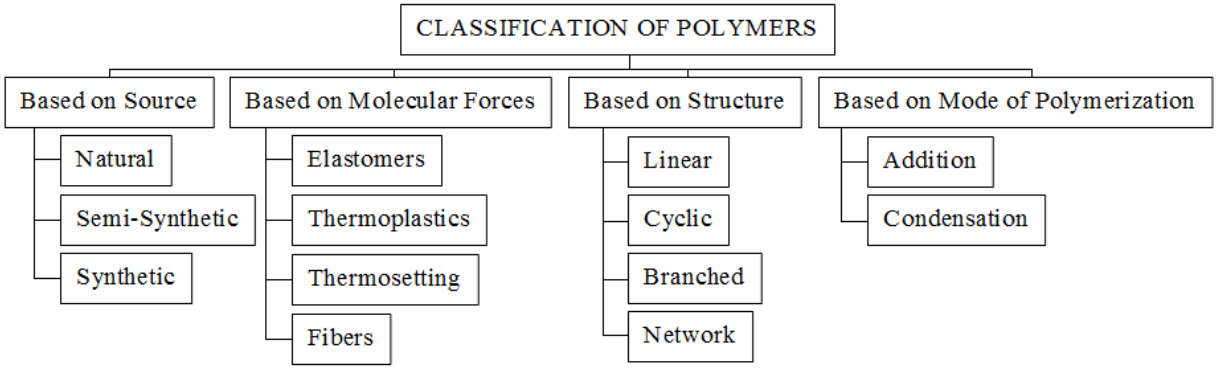

Figure 1: Classification of polymers

Polymers can also be compared in terms of architecture (or "topology") and can be divided into four sub-categories, **Figure 1**. The number of bond-forming functional groups

determines the reactivity of the monomer. Monomers need to contain two or more "bonding sites" in order to form a polymer chain or a network. The first and simplest architecture type is that of *linear polymers*, where bifunctional monomers are connected to one another in a linear fashion (*i.e.*, no branching) [Flory, 1953], [Teraoka, 2002]. Another architecture that can be formed by these bifunctional monomers are *cyclic polymers, i.e.*, those which adopt a closed ring structure. Simple cyclic chains can adopt nontrivial *knotted* topologies, while multiple rings can give rise to *link* and *braided* topologies.

The third architecture type is that of *branched polymers* which are composed of a main chain with one or more substituent side chains (*i.e.*, the "branch") [Flory, 1953], [Teraoka, 2002]. The degree of branching affects the chains ability to slide past one another and can alter the bulk physical properties. A special example of the branching architecture are dendrimers. This architecture can be scaled up to form a *polymer network* which consists of a high degree of cross-linking. Sufficiently high cross-linking may lead to the formation of infinite networks where all of the chains are linked to another molecule (*e.g.*, the case of a gel) [Teraoka, 2002]. In this case, the physical properties of the system are dominated by the nature and distribution of the "holes" in the network. Such systems are used in many applications, involving diffusion and separation of compounds drifting in the lattice (*e.g.*, chromatography and gel electrophoresis).

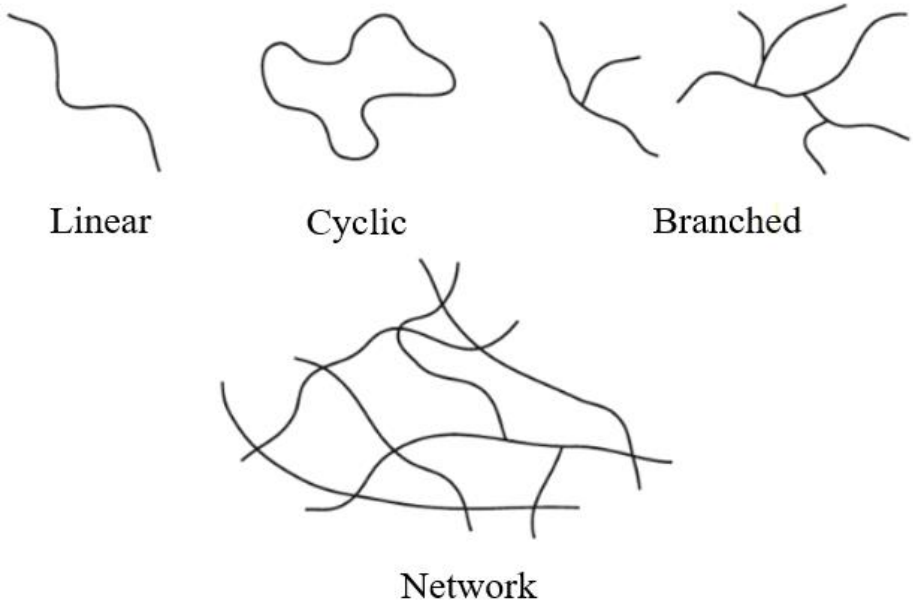

Figure 2: Skeletal structure representation of a few different polymer architectures. Adapted from [Young & Lovell, 2011].

The four architecture types are sketched in **Figure 2**.

Polymers can also be classified by the method used for their synthesis, *i.e.*, via addition and condensation polymerization reactions, **Figure 1**. Addition polymers are formed by the reaction of unsaturated monomers, where there is bond formation without the loss of a by-product. These processes follow typical chain-reaction mechanisms with three main reaction steps: initiation, propagation, and termination [Vollhardt & Schore, 2011]. Some examples of polymers formed in this manner include polyethylene, polystyrene, and PVC. On the other hand, condensation polymers may be formed by monomers that are joined together through the loss of a by-product, typically water [Flory, 1953], [Vollhardt & Schore, 2011]. Two common examples of condensation polymers are polyamides and polyesters.

Addition mechanisms typically produce homopolymers of different length and topology, while condensation leads to various forms of copolymers and block polymers that include two or more different monomers. Homopolymers, heteropolymers, and copolymers have very different chemical and structural properties. For instance, homopolymers like polyethylene or polyethylene glycol (PEG) have a distribution of populated conformers at a given temperature without the dominance of a single structure. On the other hand, heteropolymers have the potential to yield a dominant narrow range of stable conformers, such as the case of the native state of proteins. Copolymers, on the other hand, can present a different array of shapes, as solvents typically interact differently with each type of monomer.

This interplay between monomer interactions, chain architecture, and environment (such as temperature, solvent, neighbours, pressure, and geometrical confinement) regulate the shape and behaviour of the polymer. The goal of our work is to explore and understand some aspects of this interplay, using simplified polymer models and computer simulations. This thesis will investigate the shape transitions of linear end-grafted homopolymers that are attached to a hard surface and under confinement by a second polymer covered surface. In particular, we investigate the conditions in which the structure can be altered from a polymer mushroom like-regime to a polymer brush like-regime, **Figure 3**. Note that a polymer brush regime is formed when the chains are at sufficiently high density to overlap and stretch away from the surface [Weir & Parnell, 2011], [Carlsson *et al*., 2011a], [Carlsson *et al.*, 2011b]. The polymer chains are forced to stretch away along the direction normal to the grafting sites, thereby lowering the monomer concentration in the layer and increasing the layer thickness [Zhao & Brittain, 2000],

[Minko, 2006]. In the polymer mushroom regime, each chain is essentially isolated from the others, **Figure 3**.

Homopolymer brushes can be divided into neutral polymer brushes and charged polymer brushes. This thesis will focus on neutral homopolymer shape transitions, in particular the case where repulsions dominate, *e.g.*, nonpolar polymers such as polyethylene. Finally, polymer brushes may also be classified in terms of rigidity of the polymer chain and would include flexible polymer brushes, semiflexible polymer brushes and liquid crystalline polymer brushes [Zhao & Brittain, 2000], [Hsu *et al.*, 2014], [Egorov *et al.*, 2015]. We have recently carried out work on uncompressed repulsive polymer brushes [Harrison, 2014], where we explored the role of neighbouring chains as another form of geometrical confinement. In this thesis, we expand this analysis by including a confining plane and a top brush.

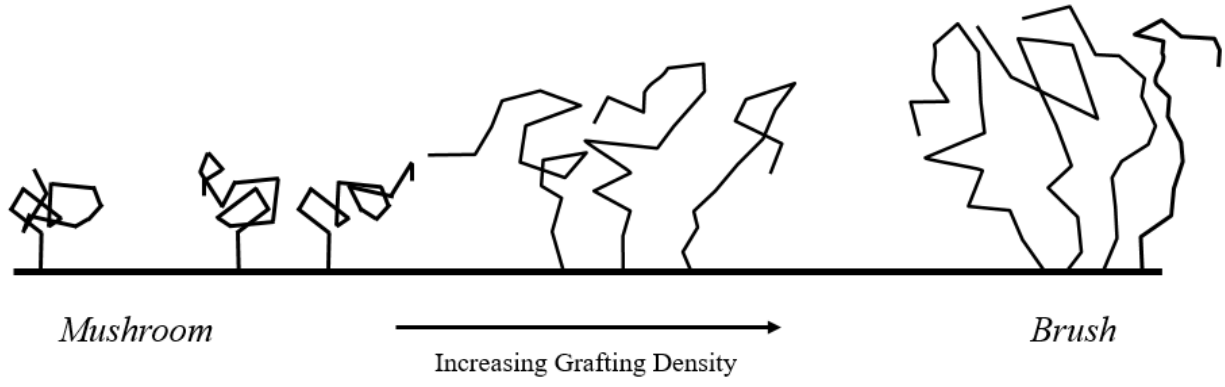

Figure 3: Transition between polymer "mushroom" and "brush" regimes. Adapted from [Brittain & Minko, 2007].

1.2. Applications of Polymer Covered Surfaces

The structural and dynamical properties of polymers can be significantly altered by confinement into small spaces, as well as grafting onto stationary surfaces [Arteca *et al*., 2001], [Edvinsson *et al*., 2002], [Coles *et al*., 2010]. In particular, the behaviour of these grafted polymers under confinement is crucial for experimental settings that involve diffusion in small spaces, compression, adhesion, flow, and shear displacements [McHugh & Johnston, 1977], [de Gennes, 1979], [Kneller *et al*., 2005]. Understanding the properties of polymer-covered surfaces

is important for a number of industrial and experimental applications that include lubrication, protective coatings, chromatography, and others [Coles *et al*., 2010], [Haw & Mosey, 2012].

Polymers and polymer networks and melts are penetrable and allow diffusion of small molecules. This characteristic can be exploited in chromatography to separate samples into its components. The polymers act as the stationary phase, allowing the separation of components of the mobile phase based on their retention times.

Polymeric brushes are applied in colloidal stabilization through the utilization of excluded volume between the polymeric chains [Grest & Murat, 1993]. In a solvent, colloidal particles collide with each other due to Brownian motion. By introducing polymers, either in the solvent or coating the particle surface, the two approaching particles may resist overlapping and aggregation, preventing flocculation [Zhao & Brittain, 2000], [Brittain & Minko, 2007].

Polymers can act as a protective coating, shielding the material surface from the external environment, thereby preventing corrosion and many other undesired reactions. For the polymer to function as a protective coating it must covalently bond to the surface to ensure stable deposition. Protective coatings may also provide physical protection to the surface, preventing scratches and reducing wear damage to the material. Additionally, polymer brushes can exhibit conformational changes that may be exploited to produce useful biomimetic effects to protect a surface from protein adsorption, improve drug delivery, and others [Chen & Fwu, 2000], [Weir & Parnell, 2011].

Polymeric foams are commonly used in impact-absorbing applications and thermal-acoustic insulating devices [Avalle *et al*., 2001], [Viot *et al*., 2005]. The polymeric foams can undergo large compressive deformation, dissipating the impact energy. Additionally, the foams can be divided into either thermoplastic or thermosetting; the latter are more difficult to recycle due to crosslinks between polymers. Polymeric foams have low apparent density, great design flexibility, and are relatively inexpensive [Avalle *et al*., 2001].

Polymers can be used as a film of lubricant that is placed between surfaces that move relative to each other. Lubricant molecules experience stress-induced changes in their structure during compression and shear deformation [Haw & Mosey, 2012], **Figure 4**. Thus, mitigating wear or decomposition of the lubricant, as well as the minimizing loss of energy during movement, are essential for efficiency [Coles *et al*., 2010]. Whether or not a polymer can

achieve the desired properties depends on the nature of the conformational transitions that can take place under the constrained geometry. This is one of the issues we address in this thesis.

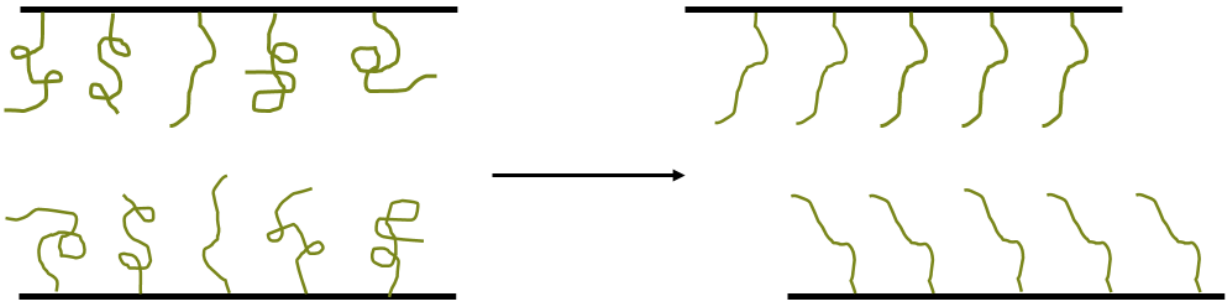

Figure 4: Lubrication between two surfaces. The diagram illustrates the microscopic role of the polymer with the gap. Adapted from [Haw & Mosey, 2012].

1.3. Effect of Solvent and Temperature on Polymeric Brushes

1.3.1. Polymers in Solution

Rheology is concerned with the deformations and flow of matter, in particular, non-Newtonian flow. In general, polymeric materials display viscoelastic properties, where the material exhibits both viscous and elastic characteristics when undergoing deformation. The materials resist shear flow and strain when a stress is applied, but also they may be able to return to their original shape when the stress is removed [Yamakawa, 1971], [Larson *et al.*, 1999].

The surface properties of polymeric brushes can be tuned using environmental conditions such as temperature and pH, to induce conformational changes [Weir & Parnell, 2011]. For instance, the collapse transition in a single random homopolymer is a well-known process triggered by a change in solvent quality [Flory, 1953], [de Gennes, 1979]. Solvent quality is of course a relative term that depends on the prevalent interactions or affinity between solvent and monomer. In good solvents, polymer coils swell, whereas under poor solvent conditions they contract into a ball, **Figure 5** [Arteca *et al*., 2001], [Espinosa-Marzal *et al.*, 2013]. This polymer "collapse", when followed by aggregation, leads to precipitation and phase separation.

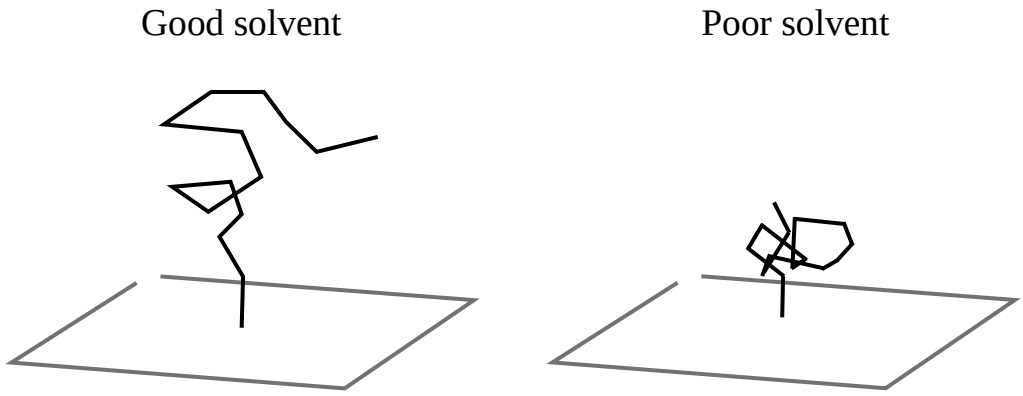

Figure 5: Example configuration of a single grafted homopolymer in 'good' and 'poor' solvent conditions. Adapted from [Arteca *et al*., 2001].

In good solvent conditions, the chains follow a self-avoiding walk statistic [Madras & Slade, 1993] and the mean size of the grafted chains scales with the number of monomers (n) as: $\langle R_g^2 \rangle^{1/2} \sim n^{0.588}$ [Minko, 2006], [Paturej *et al*., 2013], where $\langle R_g^2 \rangle^{1/2}$ is the configurationally-averaged mean radius of gyration. Thus, the brush is swollen and forms a homogeneous layer of stretched tethered chains.

Alternatively, under poor solvent conditions, the chains have self-attracting coil statistics and the mean size scales as: $\langle R_g^2 \rangle^{1/2} \sim n^{1/3}$. As a result, the chains contract and undergo a phase separation into two phases: almost pure solvent and concentrated polymer solution of overlapping Gaussian coils [Minko, 2006]. Under the so-called Θ-solvent condition, where repulsion and attraction are balanced, one finds $\langle R_g^2 \rangle^{1/2} \sim n^{1/2}$, *i.e*., the result for random walks [de Gennes, 1979].

Note that the polymer brush can exhibit a more complicated response to solvent quality compared to the polymer mushroom, since it can be affected by the density and geometrical arrangement of the neighbouring chains.

1.3.2. Theta (Θ) Temperature

The theta point of macromolecules is viewed as the point at which repulsive interactions (*e.g.*, the excluded volume interactions discussed in **2.1.2**) exactly cancel the attractive interactions between monomers of the chain, behaving as an unperturbed chain [Yamakawa,

1971], [Sheng & Liao, 2003]. The Θ temperature is conceptually equivalent to the Θ-solvent in terms of the resulting polymer chain shapes adopted; in both cases, one observes random walk configurations resulting from the balance of attractive and repulsive interaction. Note, however, that the correlation does not extend to the role of temperature in collapsing or swelling of a polymer. In nonpolar polymers, $T > \Theta$ typically will populate higher energy, more open conformers leading thus to swelling. In contrast, in thermoresponsive grafted polymers with a more complex monomer structure, $T > \Theta$ may induce desolvation (*e.g.*, partial dewetting) in a polymer, thus leading to polymer collapse instead of swelling.

The Θ-points are determined through two different definitions: the point where the second virial coefficient vanishes ($B_2 = 0$) [Yamakawa, 1971], or where one finds the quasi-ideal behaviour of the radius of gyration $\langle R_g^2 \rangle \sim n$ [Zhao & Brittain, 2000], [Minko, 2006].

Let A_1 be the Helmholtz free energy of a single chain at infinite dilution in a solvent, $A_2(\xi)$ the Helmholtz free energy of a system composed of the same solvent and two identical polymer molecules with center of mass distance ξ, k is Boltzmann's constant, and n is the chain length [Sheng & Liao, 2003]. Then, the Θ-temperature is defined by:

$$B_2 = 2\pi \int \left(1 - \exp\left[-\frac{A_2(\xi) - 2A_1}{k\Theta}\right]\right) \xi^2 d\xi = 0 \qquad (1.1)$$

In other words, at the Θ point the monomer-monomer interactions are the same as the monomer-solvent interactions and the polymer chain has "unperturbed dimensions" (*i.e.*, essentially a random walk at infinite dilution). At temperatures below the Θ-point, the monomer-monomer attractions dominate resulting in a negative second virial coefficient B_2 [Yamakawa, 1971], [Bhattacharjee *et al.*, 2013]. Thus, when the solvent is poor the polymer chains assume a more compact, entangled configuration [de Gennes, 1979]. In a good solvent the polymer chain adopts an expanded conformation and the radius of gyration is larger [Zhao & Brittain, 2000]. In the case of simple nonpolar non-grafted polymers, when the temperature increases above the Θ-temperature, interactions of the monomers with the solvent molecules are energetically favored over interactions with other segments within the polymer in solution, thus leading to swelling.

In order to narrow the scope of this project, whose goal is to model compressed polymer islands, we will impose a series of more specific conditions:

1) Polymer islands are adsorbed, with each chain permanently anchored to the surface by a terminal bead.

2) Polymers are in a "formal" solution (*i.e.*, subject to a simplified monomer-solvent interaction), and thus able to move about their anchor, within the available configurational space.
3) Solvent effects will be limited to use of excluded volume interaction (*i.e.*, a merely repulsive interaction).

1.4. Statistical Ensembles

Statistical mechanics connects microscopic details of a system to physical observables, such as thermodynamic properties, transport coefficients, and the interpretation of spectroscopic data [Allen & Tildesley, 1991], [Fehske *et al.*, 2008]. Many individual microscopic configurations of a very large system lead to the same macroscopic properties, implying it is not necessary to know the precise detailed motion of every particle in a system in order to predict its equilibrium properties. The behaviour and structural properties can be extracted from a statistical ensemble that represents a probability distribution for the states of the system. It is therefore sufficient to average over many replicas of the system, each in a different microscopic configuration, in order to study the macroscopic observables of a system expressed in terms of ensemble averages [Fehske *et al.*, 2008]. Statistical ensembles are usually characterized by fixed values of thermodynamic variables such as total internal energy E, temperature T, pressure P, volume V, number of particles N, or chemical potential μ. Three important thermodynamic ensembles are the microcanonical ensemble, the canonical ensemble, and the grand canonical ensemble. The first two are relevant to the work in this thesis.

The microcanonical (*NVE*) ensemble is a statistical ensemble where the number of particles, the volume, and the total internal energy are fixed to particular values (a so-called "energy-shell" ensemble). The system must remain isolated (preventing matter and energy from being exchanged) in order to stay in statistical equilibrium. Note that kinetic and potential energy may vary to maintain a constant total energy. Each different configuration (i) has the *same energy* E_i but different physical properties A_i, such as mean size or shape. In the case of a set of Ω degenerate states, we have:

$$\langle A \rangle_{NVE} = \frac{1}{\Omega} \sum_{i=1}^{\Omega} A_i \qquad (1.2)$$

where Ω is the microcanonical degeneracy or "partition function".

The canonical (*NVT*) ensemble is a statistical ensemble where the number of particles, the volume, and the temperature are fixed to specific values. The canonical system is appropriate for describing a non-isolated closed system (preventing exchange of matter) that is in contact with a heat bath to stay in statistical equilibrium. Each configuration has different energy but identical composition. In this case, the equilibrium mean value of the property "A" is given by:

$$\langle A \rangle_{NVT} = \frac{1}{Q_N(V,T)} \sum_{i=1}^{\infty} A_i g_i e^{\frac{-E_i}{KT}} \quad (1.3)$$

$$Q_N(V,T) = \sum_{i}^{\infty} g_i e^{\frac{-E_i}{KT}} \quad (1.4)$$

where $Q_N(V,T)$ is the canonical partition function.

The grand canonical (μVT) ensemble is a statistical ensemble where the chemical potential, the volume, and the temperature are fixed to specific values. Since the total internal energy and number of particles are not fixed, the grand canonical ensemble describes open systems, permitting the transfer of energy and matter. The corresponding equilibrium mean value of property "A" is then:

$$\langle A \rangle_{\mu VT} = \frac{1}{\Xi} \sum_{N=0}^{\infty} A_N(V,T) e^{\frac{\mu N}{KT}} Q_N(V,T) \quad (1.5)$$

$$\Xi = \sum_{N=0}^{\infty} e^{\frac{\mu N}{KT}} Q_N(V,T) \quad (1.6)$$

where $\Xi(\mu,V,T)$ is the macro canonical partition function.

The assumption that a system, given an infinite amount of time, will explore the entire configurational space is known as the ergodic hypothesis [Fehske *et al.*, 2008]. An ergodic system is one that evolves in time indefinitely to explore all accessible configurations. The ergodic hypothesis, states that the time average equals the ensemble average

$$\langle\langle A(t) \rangle\rangle = \langle A \rangle_{ensemble} \quad (1.7)$$

In this work, we deal with a continuum of polymer configurations, in principle, consistent with a canonical *NVT* ensemble. However, as explained later in the methodology section, the polymer model used involves only hard-sphere interactions between monomers (and formally, the solvent). As a result, all accessible configurations are de facto degenerate, in other words, our simulations are reduced in this model to the analysis of a microcanonical ensemble of degenerate, equal-probability configurations [Arteca, 1994].

1.5. Simulation Methods for the Investigation of Polymer Structure

Molecular simulations may be defined as the determination of the macroscopic properties of a system by using a microscopic model of particle interactions [Fehske et al., 2008]. Simulation techniques are based on the laws of statistical mechanics and molecular dynamics, which give us the theoretical basis to make the connection between microscopic modelling and macroscopic behaviour (shown in previous section).

Two essentially different kinds of molecular simulations are typically performed. The first is a deterministic time-dependent approach: Newtonian molecular dynamics method produces trajectories in configurational space leading to both static and dynamic properties (such as the distribution of kinetic energy or self-diffusion coefficients). The second is a stochastic approach, this includes stochastic molecular dynamics simulation (*e.g.*, Brownian and Langevin dynamics) as well as purely stochastic, time-independent configuration searches. The archetypical example of the latter is the Monte Carlo method where, the configurational space of the system is randomly sampled, leading to the evaluation of mean properties within the desired statistical ensemble. In all these techniques, the positions of all the particles are known at each step. As a result, molecular simulations are advantageous in deducing local structure of the system.

1.5.1. Overview of Molecular Dynamics Simulation

Molecular dynamics (MD) simulations are a computational method that calculates the time-dependent behavior of a molecular system followed by integrating their equation of motion with the appropriate boundary conditions of the system [Jorgensen & Tirado-Rives, 1996], [Fehske et al., 2008]. MD simulations can provide detailed information on the fluctuations and structural (*i.e.*, conformational) changes in polymer systems with respect to time, as well as determine rates of reactions, solid state structures, and defect formations in materials [Fehske *et al.*, 2008], [Edens *et al.*, 2012]. This is accomplished by using Newton's equations of motions to determine atomic positions and velocities as a function of time, possibly including the solvent explicitly. In contrast to the purely stochastic methods discussed in Sec. **1.5.2**, MD provide insight into the detail (time-dependent) mechanism underlying the configurational transitions.

MD simulations require the interaction potential (or force field) for the particles, as well as the equation of motion governing the dynamics of the particles in order to calculate the

microscopic behaviours of the system. The MD technique begins with Newton's equation of motion for atom *i* in a system of *N* atoms where m_i is the mass of the atom, $\boldsymbol{a}_i$ is the vector acceleration, and $\boldsymbol{F}_i$ is the force vector acting on it (due mainly to the interactions of other atoms), equation 1.8:

$$\boldsymbol{F}_i = m_i \boldsymbol{a}_i = -\nabla_i U = m_i \ddot{\boldsymbol{r}}_i \tag{1.8}$$

$$\boldsymbol{a}_i = \frac{\mathrm{d}\boldsymbol{v}_i}{\mathrm{d}t} = \frac{\mathrm{d}\boldsymbol{r}_i}{\mathrm{d}t} \tag{1.9}$$

Knowing the atomic forces and masses, we are then able to solve for the atomic positions using a series of small time steps on the order of femtoseconds, shorter than a typical fast bond stretching vibration. If the time step involved in the numerical integration is too large (without constraining degrees of freedom), the numerical integration becomes unstable [Pande *et al.*, 2008]. At each time step the forces on the atoms are computed and combined with the current positions and velocities to generate new positions for the next time step. The atoms are then moved to the new position and a new set of forces are computed [Fehske *et al.*, 2008]. Once a full trajectory is evaluated over time ($t < \tau$), we can compute the desired property of the system (say, property "A") at each time step. Finally, the MD corresponding mean value $\langle\langle \mathrm{A} \rangle\rangle$ is computed as:

$$\langle\langle \mathrm{A} \rangle\rangle = \lim_{\tau \to \infty} \frac{1}{\tau} \int_0^{\tau} \mathrm{A(t)dt} \tag{1.10}$$

The canonical characteristics of a system can also be incorporated into Newtonian MD by a method that provides temperature regulation. This is done in a rough approximation by introducing some form of temperature scaling [Allen & Tildesley, 1991]. The so-called Berendsen thermostat [Berendsen *et al.*, 1984] is one such regulation procedure, where the velocity scaling is introduced so that the system follows Newton's cooling law, by being coupled to a formal thermostat at the target temperature.

Another approach to modelling the dynamics of molecular systems is Langevin (or Brownian) dynamics. Langevin dynamics is an extension of Newtonian MD and takes into consideration a frictional term which accounts for perturbations of the molecules of the system. The frictional term is associated with the interactions of the system with a solvent,

$$-\boldsymbol{\nabla}_i U = m_i \ddot{\boldsymbol{r}}_i + \bar{F}_i(\boldsymbol{r}_i) \tag{1.11}$$

where $\bar{F}_i$ is a dissipative term, that includes the solvent viscosity via the Stokes law, and a random kick term associated to Brownian motion.

1.5.2. Overview of Monte Carlo Simulation

Monte Carlo (MC) simulation is a conformational sampling technique that relies on repeated random searches, a random number generator, and a probability distribution to produce a very large sample of possible outcomes. Monte Carlo's main uses are in understanding and controlling complex stochastic systems (*i.e.* those whose behavior emerges from random processes) [Metropolis *et al.*, 1953], [Hastings, 1970], [Jorgensen & Tirado-Rives, 1996].

MC samples the configurational space using a sequence of "accepted" configurations known as Markov chains (see eq. 1.4 and 1.5 in previous section). A new configuration is generated by selecting a random move in configurational space that involves translations, rotations, and internal structural variations, and then checking whether the move is accepted or rejected using the Metropolis algorithm (discussed in **2.1.3**) [Fehske *et al.*, 2008]. Each move in a canonical ensemble would have the probability P_j of encountering the particular configuration j when making a random observation of the system given by:

$$P_j = \frac{g_i e^{-E_j/kT}}{Q_N(V,T)} \qquad (1.12)$$

where g_i is the degeneracy of the energy level E_i, and $Q_N(V,T)$ the canonical partition function (eq. 1.4).

Within the context of this work, the Metropolis algorithm for the generation of an acceptable configurational in a grafted polymer chain in a coarse-grained "bead" model is as follows:

(i) Starting with the bead anchored to the adsorbing plane, the potential energy ("force-field") of the system (configuration j) is calculated

(ii) A tentative bead position is proposed for every monomer in the model.

(iii) Next the potential energy of the system is calculated for the candidate configuration (j + 1).

(iv) The probability of the candidate configuration is compared and either accepted or rejected using the Metropolis-Hastings algorithm (see eq. 1.13), where the relative probabilities are compared with a random number $\xi \in [0,1]$.

$$\frac{P_{j+1}}{P_j} = e^{\frac{-\Delta E_{j\rightarrow j+1}}{kT}} \qquad (1.13)$$

(v) The process continues and every new configuration is constructed in the same way from the last accepted configuration. In chapter 2 we discuss in more detail how this is implemented for polymers with excluded volume interaction.

Like MD, MC has a similar system setup that requires force fields for potential energy terms, as well as implementation of periodic boundary conditions [Jorgensen & Tirado-Rives, 1996]. MC is valuable in studying systems that are often not feasible to control by other methods due to their complexity. Similarly, MC must be used for strictly quantum systems where it is not possible to evaluate classical velocities and forces, as required in MD. The calculation of the physical properties of such a system is often unfeasible using conventional numerical methods due to its complexity, so one must resort to a probabilistic approach and calculate the mean physical properties from a randomly-generated, weighted set of configurations of the system. (From the technical point of view it is important that the random numbers are not repeated, which could distort the results).

As stated in equation 1.8, we work under the assumption that a system, given an infinite amount of time, will cover the entire configurational space, known as the ergodic hypothesis [Fehske *et al.*, 2008]. Consequently, MD and MC simulations produce the same equilibrium results.

1.6. Motivation and Organization of Thesis Objectives

1.6.1. Escape Transitions and Previous Research Conducted by our Lab

As commented earlier, this thesis uses computer simulations to study how confinement conditions affect some aspects of polymer shape. We are interested in characterizing how structure and shape of grafted chains is affected by the presence of neighbours and compression. In particular, we want to probe these effects in the case of chains with repulsive interactions (*e.g.*, nonpolar linear polymers), which represent one of the least understood systems given that they exhibit the subtlest structural responses.

To provide a contrast for one of the main motivations for this research, it is important to consider some recent work in the literature, part of it is done in our laboratory.

A pair of studies conducted by Carlsson *et al*. in 2011 used MD to investigate the off-equilibrium responses of grafted polymer chains with respect to compression in a randomly

covered single-surface polymer brush. They found that chain entanglement complexity, as well as other molecular shape properties of adsorbed polymer islands, depend more strongly on surface coverage than on the nature of the dominant monomer-monomer interaction. More significantly, it was found that the same trends in shape descriptors as a function of packing density and compression were observed in polymer chains with both excluded volume interactions, as well as in polymers with attractive intra- and inter-chain interactions [Carlsson *et al*., 2011a], [Carlsson *et al*., 2011b]. For example, it was found that during fast compression, individual chains in densely-packed polymer brushes adopt smaller shapes than chains in loosely-packed brushes. While this is a logical response to the available space in the case of attractive chains (which have the ability to collapse unto themselves under compression), it was a surprising result in the case of repulsive chains. This result indicates that, under some conditions, adopting compact shapes may also be possible in absence of monomer-monomer attraction, provided that the favorable confinement conditions are present.

Following those conclusions, we investigated in our lab polymer islands constructed by means of freely-jointed chains with excluded volume interactions and investigated the effects of not only surface coverage but also packing geometry on the equilibrium shape properties [Harrison, 2014]. In that project, we characterized the structural and shape properties of the polymer islands in terms of size, anisometry, entanglement complexity, and chain orientation, when the chains were free from compression (*i.e.*, no confining top plate). All these properties are explained in detail in chapter 2. We found that when breaking the symmetry in geometrically packed chains, it was possible to create sufficient space to allow a polymer chain to produce the type of unusual, nonuniform conformations found in the so-called "escape transitions" or "coil-to-flower transitions", previously seen only in polymers with attractive interactions [Subramanian *et al*., 1995]. (Actual physical escape is not possible since the chains are permanently grafted to the surface [Arteca, 1997a]).

Unusual polymer deformations can be induced by hydrodynamic flow as well as interaction of the chains with a surface [Guffond *et al*., 1997]. However, while a polymer can be stretched or elongated evenly under flow in a narrow channel, the presence of a finite-size object can elicit the formation of configurations with uneven stretching, a so-called "escape transition" where a grafted polymer undergoes a conformational transition that allows it to "dodge" the approaching obstacle.

An "escape" transition of a polymer mushroom occurs when the polymer is compressed by a finite-size disk (*e.g.*, the bottom of an AFM tip) of radius *R*, that exceeds the chains radius of gyration but is smaller than the chain length [Milchev *et al*., 2007], [Paturej *et al*., 2013]. The transition is driven by a gain in configurational entropy due to geometric confinement as part of the chain escapes [Milchev *et al*., 2007], [Mökkönen *et al*., 2015]. The result is a so-called "flower" conformation. These structures are characterized by a nonuniform distribution of monomers, exhibiting an elongated swollen tether (or "stem") under the compressing obstacle, and re-compactified sub-region outside the obstacle (or "flower"). These transitions have been predicted theoretically [Subramanian *et al*., 1995] and observed experimentally later [Abbou *et al*., 2006] but not yet in polymers with repulsive interactions. The result again highlights that, under particular confinement conditions, repulsive polymers can adopt molecular shapes thought to be only accessible in the presence of attractive interactions.

This thesis project seeks to extend our earlier work by gaining insight into the nature of dominant configurations for chain avoidance (*i.e.*, escape). In this project, we explored the effects elicited by confinement due to the presence of an upper surface which is covered by a second polymer brush, as well as shape transitions occurring during shear displacements (*i.e.*, lubrication). Using MC, we study the equilibrium configurations between the surfaces in terms of molecular shape descriptors for individual and relative chain shape. Much work was spent tuning the controlled variables (*e.g.*, plate separation, chain length, excluded volume and chain location) in order to determine the conditions that disfavor chain interpenetration, *i.e.*, determining where configurations switch from high inter-chain entanglement (interaction between chains) to high intra-chain entanglement (self-entangled). As discussed by Carlsson *et al*. [2011a, b], a descriptor of chain entanglement characterizes better the formation of conformations with nonuniform local folding features, than a descriptor of mean size or asphericity. More significantly, a measure of inter-chain entanglement is the only efficient simple tool for characterizing changes in relative chain orientation, *i.e.*, changes of shape that arise from reorganizations between chains that leave the individual chain shape characteristics unchanged.

Much of the previous work conducted by our laboratory has focused on testing whether the mean overcrossing number could be used to monitor the evolution of folding features as well as the occurrence of configurational "escape" transitions [Arteca, 1997a], [Edvinsson *et al*.,

2000], [Arteca *et al*., 2001], [Arteca *et al*., 2001a], [Arteca *et al*., 2001b], [Edvinsson *et al*., 2002], [Arteca, 2003]. A pair of studies conducted by Arteca *et al*. in 2001, investigated structural transitions in lysozyme proteins in vacuo using MD simulations (**Figure 1** in [Arteca *et al*., 2001a], and [Arteca *et al*., 2001b]). The proteins were made to undergo phase transitions from a compact (*i.e.*, native states) to unfolded states by decreasing the attractive forces between their monomers, and then return back to the native states by undoing the changes. Depending on the nature of the protein (or polymer), folding can occur via two different mechanisms, involving distinct manifolds of reaction paths and sequences of configurations. The first occurs where local secondary structure were formed prior to compaction, thus leading to a growth in entanglement complexity (*i.e.*, larger $\overline{N}$), and small changes in global globularity (*i.e.*, nearly constant Ω). The second occurs when chains undergo a partial polymer collapse with little development of the secondary structure (**Figure 1** in [Arteca *et al*., 2001a], and [Arteca *et al*., 2001b]), leading first to a rapid decrease in Ω with small change in $\overline{N}$. One of our objectives in this project is to analyze whether that chain entanglement complexity, in particular inter-chain entanglement, is a sensitive descriptor to detect molecular shape changes and configurational transitions that may occur when chains, grafted to opposing surfaces, are brought nearer to each other (either through compression or shear displacement).

1.6.2. Objectives and Organization of this Thesis

In this project, we use MC simulations of adsorbed polymer islands to study structural and shape transitions that occurred due to confinement by a second polymer covered surface (or "plate"). The polymer islands were built as coarse-grained self-avoiding walks (SAWs), with only repulsive (hard excluded-volume) interactions. The equilibrium configurations generated are characterized in terms of molecular shape descriptors for individual and relative chain shape. Using these structures, we address the following objectives:

(i) Study equilibrium configurations between surfaces using molecular shape descriptors for individual and relative chain shape (*e.g.*, comparing intra- *vs* inter-molecular shape as two repulsive mushrooms are brought closer by compression).

(ii) Determine how shape is affected by plate separation (*i.e.*, the distance between the grafting planes), chain length, chain location, and the strength of the excluded volume interaction.

(iii) Gain insight into the nature of dominant configurations for chain avoidance by observing chain entanglement complexity, in particular inter-chain entanglements. In particular, study whether escape transitions (*i.e.*, coil-to-flower configurational changes) are induced by compression in the presence of a few neighbouring chains. As discussed before, escape transitions can take place in repulsive polymers in the absence of compression if there is an asymmetric, sufficiently-dense, arrangement of chains coordinating the "escaping" chain. In this thesis, we analyze whether compression changes this situation.

The thesis is organized as follows. The next chapter presents the methodology, in particular, the method to build the polymer configurations by using the Monte Carlo method and the techniques used to characterize their structure and shape. After, we discuss the details of the algorithms to implement those methods and illustrate them in examples. The following chapters present our general results, our main observations and the conclusions that can be extracted with respect to the stated objectives.

Chapter 2

2. Methodology

2.1. Monte Carlo Simulations of Coarse-grained Polymer Islands

In our case, as explained below, the equilibrium configurations for end-grafted polymer chains are created using Monte Carlo simulations with Marsaglia's algorithm [Marsaglia, 1972]. The proposed configurations are either 'accepted' or 'rejected' using the Metropolis algorithm [Metropolis et al., 1953], [Hastings, 1970]; in our case we consider only hard-sphere excluded-volume interactions (*i.e.*, self-avoiding walks) [Madras & Slade, 1993]. Polymers are thus built as coarse-grained self-avoiding walks where the first bead (each bead representing an "effective" monomer) is anchored to a surface and successive monomers are added to the previous bead with fixed bond lengths, but randomly oriented in space and subjected to the constraints of excluded volume to all other beads, either bounded or not. The full algorithm is explained in sections **2.1.2-2.1.4**.

2.1.1. Coarse-grained Polymer Models

The use of full quantum mechanical atomistic models in simulation have shown great success in reproducing experimentally observed behaviors of polymers and proteins. However, they are computationally demanding since the calculations needed involve many atom-atom interactions. For this reason, they are usually limited to relatively small systems and time scales [Edens *et al.*, 2012]. Consequently, coarse-grained models can be used to represent groups of atoms as spherical beads, thereby allowing larger systems to be studied that would be impractical with atomistic models. Of course, coarse-grained models eliminate degrees of freedom and thus can only be used to study qualitative global behaviour and not local structural details.

By choosing an appropriate resolution for each feature, very large biological systems can be modeled over long times [Harmandaris *et al.*, 2006], [Müller-Plathe, 2002]. There are several coarse-grained geometrical models such as: rod-and-bead, bead and spring, and pearl necklace, that are useful in predicting how the physical properties of entire polymer chains in solution depend on chain length, concentration, and the repulsive forces between monomers [Teraoka, 2002]. In this thesis, a version of the rod-and-bead model is used where each bead represents the center of a monomeric unit and the "rods" represent the connectivity between beads (in our case, all bond lengths are the same). Thus, the model appears as a coarse-grained (lower resolution)

version of the atomistic model. The bond and dihedral angles are restricted only by the repulsive force between monomers (refer to excluded volume discussed in **2.1.2**). In absence of excluded volume, this model is known as a freely-jointed chain [Bhattacharjee *et al.*, 2013]. When excluded volume is present, the model is a self-avoiding walk in the continuum [Madras & Slade, 1993].

Another important consideration is the choice of interaction potential U (*i.e.*, potential energy or "force field") of the system of atoms or coarse-grained particles. To describe complex molecules, a large set of inter-atomic potentials are used to describe intra- and inter-molecular interactions [Fehske *et al.*, 2008]. The potential energy is divided into terms arising from connected atoms and non-bonded terms (typically, long-distance electrostatic and Van der Waals forces). The standard form is:

$$U(\bar{r}) = U_{\text{bond}} + U_{\text{angle}} + U_{\text{torsion}} + U_{\text{nonbonded}} \quad (2.1)$$

where:

1) U_{bond} describes the pair-potential energy related to changes in the bond length (*i.e.*, stretching).
2) U_{angle} describes the potential energy associated with bond angle vibrations (*i.e.*, a three-body potential).
3) U_{torsion} describes the potential energy associated with the rotation between parts of the molecule relative to each other (*i.e.*, a four-body potential). The generic vector $\bar{r}$ (in eq. 2.1) indicates all relevant atomic, or bead coordinates.

The last $U_{nonbonded}$ term is frequently modeled using the two-parameter Lennard-Jones potential, involving a long-distance attraction due to induced dipole-dipole interaction, and a strong short-distance repulsion [Lennard-Jones, 1924], [Allen & Tildesley, 1991]:

$$U_{LJ}\left(\{\bar{r}_{ij}\}\right) = 4\epsilon\left[\left(\frac{\sigma_{ij}}{r_{ij}}\right)^{12} - \left(\frac{\sigma_{ij}}{r_{ij}}\right)^{6}\right] \quad (2.2)$$

where ϵ is the strength of the interaction, and σ_{ij} represents the effective shortest distance for the pair of i and j beads.

Another frequently used model (used in this thesis) is the hard-sphere potential U_{HS}. The hard-sphere potential mimics the strong repulsion that atoms and molecules experience at very close distances. In this case, the potential energy of the molecule is then either zero, if no

overlaps exist, or infinite if one or more beads overlap [Stellman & Gans, 1972], [Allen & Tildesley, 1991]:

$$U_{HS} = \begin{cases} 0 & if\ |r_i - r_j| > \sigma \\ \infty & if\ |r_i - r_j| < \sigma \end{cases} \qquad (2.3)$$

As a result, the beads are forbidden from overlapping.

In this case, all acceptable configurations are effectively degenerate, $U_{HS} = 0$, thus constituting a *de facto* microcanonical ensemble.

2.1.2. Overview of Excluded Volume and Self-Avoiding Walks

In polymer science, excluded volume refers to the idea that one part of a long chain cannot occupy the space that is already occupied by another part of the same chain [Flory, 1953], [de Gennes, 1979], [Grosberg & Khokhlov, 1997]. Excluded-volume or steric interactions arise from the mutual impenetrability of finite-size particles [Edwards, 1965], [Bruna & Chapman, 2012]. As mentioned earlier, the model is built according to a rod-and-bead polymer chain, whose shape is then characterized using the configurationally-averaged shape descriptors as a function of the excluded volume and chain length, in addition to the physical parameters associated with the confinement conditions.

The grafted self-avoiding walks studied in this thesis are built as follows:

1) The first bead is grafted permanently to the surface,
2) The second bead is attached to the first at a fixed distance *l* along a direction perpendicular to the surface (taken as the *z*-axis). In order to produce molecular size comparable to those of short polyethylene chains, we choose l = 1.50Å as a constant bond length. In this case, each "polymer bead" can be seen as a coarse-grained version of a methylene group, (*i.e.*, -CH_2-).
3) A third bead is attached to the second bead at a distance *l*, but with an arbitrary and tentative location in space using the Marsaglia algorithm. (This method provides a random distribution of points on a sphere, thus a fixed bond length but arbitrary bond angles). (See section **2.1.4)**. We include, in addition, a hard-sphere interaction with all involved planes, either for grafting and compression; no bead can touch or penetrate any bottom or top plane. Bead positions with non-bonded neighbours at distances smaller than the so-called radius of excluded volume (r_{ex}) are rejected. This radius, r_{ex},

corresponds to the *diameter* of a sphere around each identical bead that the *centres of other beads* cannot penetrate, **Figure 6**. Accordingly, we check the distance between the centres of the third and first bead; if the distance is smaller than the excluded volume radius (r_{ex}), the configuration is rejected and the self-avoiding walk restarts from the beginning [Arteca, 1994].

4) If the conformation is accepted, another bead (*i.e.*, a fourth bead) is linked to the previous in the same approach, and the contacts with the non-bonded beads are checked (*i.e.*, with beads 1 and 2). The procedure continues until a successful configuration with *n* beads has been generated.

At every step, we also checked that no tentative bead-center positions lie above the top grafting plane or below the bottom grafting plane; any such position is rejected and the building of the chains recommences *from scratch*. Each additional chain within the polymer cluster is built by the same process, always checking that the excluded volume interaction is not violated within a chain and among chains. Since each accepted configuration is built independently of the others, we can use every single one of them to compute configurational averages, without any bias or correlations.

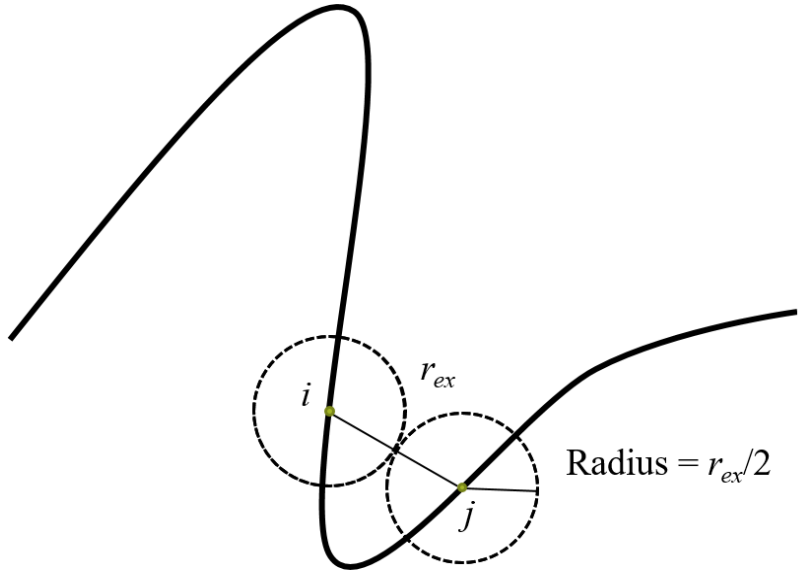

Figure 6: Schematic representation of an excluded volume interaction between two non-bonded monomer beads *i* and *j* in a self-avoiding walk model. The distance r_{ij} must be larger than r_{ex} for the configuration to be accepted.

Note that the excluded volume radius can have a maximum value of $2l$ (where l is the bond length), at which point the chain would be forced to adopt a single linear, rigid rod conformation configuration [Arteca, 1994], which would be stochastically unachievable (having zero entropy, and zero random probability). For $r_{ex} < 2l$, the chain can adopt an infinite number of configurations. However, as r_{ex} approaches $2l$, the searches become more time consuming, and eventually computationally unfeasible. As discussed before, the changes in the nature of the polymer configurations with excluded volume are analogous to the effects of temperature and solvent on polymers [Flory, 1953], [de Gennes, 1979], [Grosberg & Khokhlov, 1997]. Under 'poor' solvent conditions the chains adopt compact configurations, whereas under 'good' solvent conditions the chains take on an extended or swollen configuration [Edvinsson *et al.*, 2002]. Remember, however, that the correspondence between good solvent and high temperature is not necessarily valid for nonpolar polymers.

2.1.3. Metropolis-Hastings Algorithm

The self-avoiding walk used to construct the macromolecular chains fall into a broader category of randomized algorithms which are represented by Markov chains [Hastings, 1970]. Markov chains belong to a class of random processes that look exclusively at the previous outcome to determine the effects on the new outcome [Häggström, 2002]. A Markov chain can be described as having several "states"; in our case, these correspond to the accepted configurations of our chain or set of chains. The process begins at one state and then moves to another state in a process called "a step". Each step has an associated probability that depends only on the previous state, not on the entire chain of events. In other words, a Markov chain is said to have "no memory". The steps are governed by a transition kernel, which is the mechanism that describes the probability of moving to another state based on its current state (**Figure 7).**

One of the most common Markov-chain procedures is the MC method that uses the Metropolis-Hastings algorithm, to 'accept' or 'reject' each new state of the cluster of polymer chains [Metropolis *et al*., 1953], [Hastings, 1970], and [Chib & Greenburg, 1995]. MC performs random sampling over the configurational space and proposes new configurations. Starting from a configuration "i", a new configuration "$i + 1$" is tested using the Metropolis-Hastings method which compares the Boltzmann factor $e^{(-\Delta E_{i,i+1}/kT)}$ with a random number $\xi \in (0,1)$, where

$\Delta E_{i,i+1} = E_{i+1} - E_i$ is the energy difference between the states (*i.e.*, the last "accepted" configuration "*i*" and next tentative configuration "*i* + 1"). If *j* is accepted, we move on to create the next tentative state *i* + 2. If the *j*-move is rejected, the configuration is abandoned and MC restarts from the *i*-configuration and develops a new tentative (*i* + 1)-configuration.

The criterion for acceptance and rejection works as follows: if the energy of the new configuration is lower, the configuration is always accepted. If the energy of the transition is higher, (*i.e.*, $\Delta E_{i,i+1} = E_{i+1} - E_i > 0$), the new configuration has a $e^{(-\Delta E_{i,i+1}/kT)}$ probability of being accepted, and the decision is made drawing a random number $\xi \in (0,1)$. Since $e^{(-\Delta E_{i,i+1}/kT)} < 1$ if $\Delta E_{i,i+1} > 0$, then if $\xi \leq e^{(-\Delta E_{i,i+1}/kT)}$, then the "*i* + 1" configuration is accepted. If $\xi > e^{(-\Delta E_{i,i+1}/kT)}$, it is rejected.

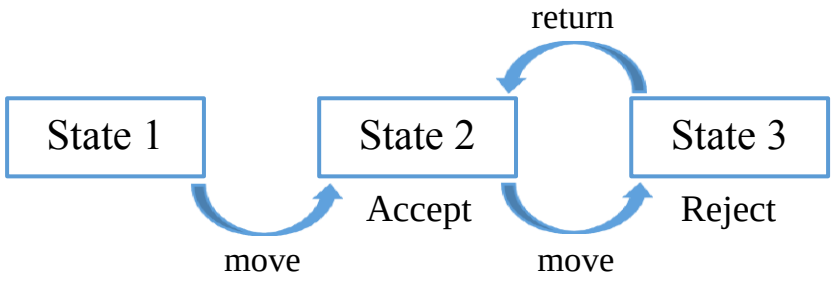

Figure 7: Schematic representation of a Markov chain. The process begins at State 1 and moves to State 2. The step is accepted and continues moving forward to State 3. If a criterion is not met for the new configuration at State 3, the configuration is rejected and restarts from State 2.

In our present case, when using a hard-sphere type of excluded-volume interaction, the situation is easier since all accepted SAW configurations have the same energy value ($E_i = 0 \; \forall \; i$), while all rejected configurations have infinite energy. As a result, as stated before, the statistical weighting of all sampled configurations is exactly the same, and there is no bias towards generating any particular shapes. In the resulting configurational ensemble, the fluctuation in all properties is determined strictly by sample size as $\sigma = \frac{1}{\sqrt{N}}$. In our case, we use N = 2500 independent configurations, which produces an intrinsic fluctuation of $\sigma = \frac{1}{50}$ (*i.e.*, a 2% uncertainty), in all mean values for the properties. (This is aside from the numerical error in estimating each property; the more computationally intensive and having the largest error is the mean overcrossing number that describes entanglements). The final result is that all the accepted

chains have the same energy, while the rejected states have energies that are infinitely large. For this reason, the MC canonical search produces, in the case of hard-sphere interactions (or excluded volume), a *de facto* microcanonical ensemble.

2.1.4. Marsaglia's Algorithm

We use the Marsaglia's algorithm to locate a bead randomly on the surface of a sphere with *l*-radius [Marsaglia, 1972]. Marsaglia's algorithm generates two independent uniform distributions V_1 and V_2 on (-1, 1) so that:

$$S = V_1^2 + V_2^2 < 1 \qquad (2.4)$$

We use a pseudo-random number generator to create a quasi-uniform distribution of points on the sphere; these are the tentative positions for the monomer beads before we apply the excluded volume condition, **Figure 8**. In our case, we use the L'Écuyer random number generator combined with the Bays-Durham shuffling technique which ensures approximately 2×10^{18} quasi-random values [L'Écuyer, 1990], [Press *et al*., 1992].

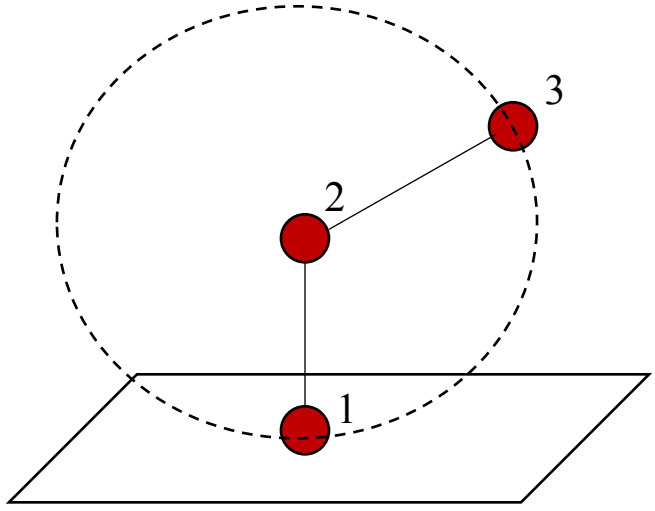

Figure 8: Monte Carlo method to build a chain by using Marsaglia's algorithm to perform random sampling over the configurational space. A new bead position is located randomly on the unit circle. The accepted position "3" must also satisfy the excluded-volume condition to bead "1", *i.e.*, $\|\bar{r}_3 - \bar{r}_1\| > r_{ex}$.

2.2. Molecular Shape Descriptors

In order to describe the large-scale shapes of macromolecular chains, it is crucial to develop molecular shape descriptors that characterize the size, anisometry (or globularity), and chain-entanglement of the rigid polymer configurations [Arteca, 1996a]. A simple array of nuclei in space is specified by the molecular geometry, and the resulting molecular geometry descriptors do not depend on chain connectivity [Arteca, 1994]. Some geometrical descriptors for polymer structure polymers are the end-to-end chain distance, the radius of gyration, and the measures of anisotropy derived from them (*e.g.*, asphericity) ([Rudnick & Gaspari, 1986], [Arteca, 1996a]). However, a purely geometrical approach to studying polymer properties is not sufficient, since it is often impossible to recognize folding features and the connectivity of the different conformations. In some cases, such as those of polymer chains with topological defects (*e.g.*, knots), these descriptors fail to capture the essential or most important properties. In these cases, other descriptors must be used, those that incorporate connectivity, in addition to purely geometrical information.

An alternative approach is to use topologic methods to describe the shape of a polymer for entire subsets of configurations, independent of the size and compactness of the polymer. However, a purely topological approach is often also insufficient to study polymer properties as it does not distinguish between conformations [Ziabicki, 1976], [Arteca 1994]. Consequently, a hybrid technique is used which combines elements of the chains geometry and topology, in order to characterize properly the polymer configurations in terms of static and dynamic entanglement.

2.2.1. Polymer Chain Mean Size

The first descriptor is the radius of gyration (R_g), which represents the polymer chain's mean size. Radius of gyration is affected by chain length and solvent quality and can be used to measure, to some extent, the compactness of a polymer chain [Flory, 1953]. The number of atoms is proportional to the backbone contour length, also referred to as the chain length. For convenience, the geometric center of the single homopolymer chain is chosen as the origin. The radius of gyration is described in the equation below, where n represents the number of beads in the chain, $\boldsymbol{r}_i$ is the position vector for the beads measured from the chains centroid (here the center of mass) as origin:

$$R_g^2 = \frac{1}{\mathrm{n}}\sum_{i=1}^{n}\|\boldsymbol{r}_i\|^2 \qquad (2.5)$$

In this case, the radius of gyration is mass independent; in heteropolymers or block copolymers, different atomic masses must be taken into consideration. A dimensionless ratio of radius of gyration becomes the descriptor for molecular size of the polymer chain:

$$\langle R_g^2 \rangle^{1/2} / \ll \|b\| \gg \quad (2.6)$$

where $\ll \|b\| \gg$ is the mean bond length. This ratio is used to describe the compactness of polymer chains due to the geometry, the density of packing, as well as the effect of excluded volume interactions. Other related size descriptors appear in **Figure 9**.

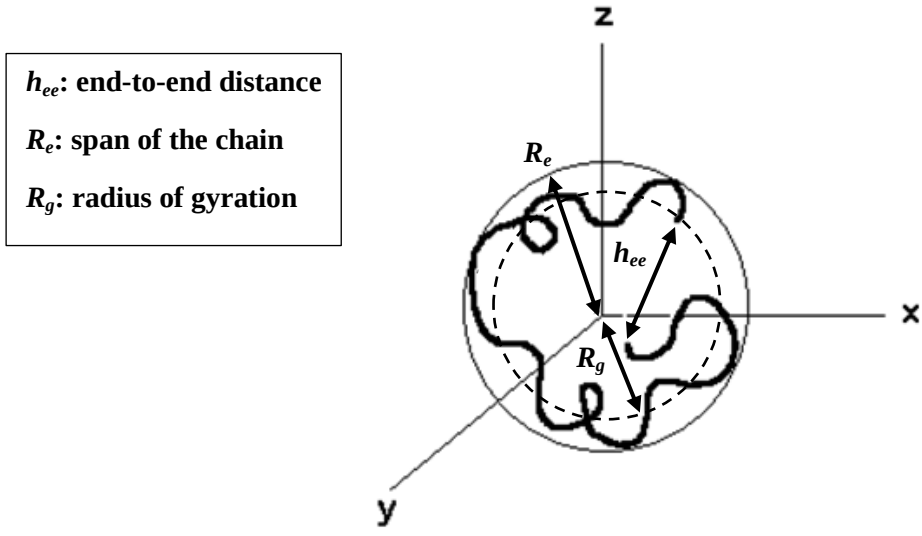

Figure 9: Schematic representation for the computation of the radius of gyration. The polymer configuration is specified by the monomer positions with respect to the centre of mass of the polymer chain. The three size descriptors h_{ee}, R_e, and R_g have the same statistical characteristics, but R_g has the smoother behaviour (*i.e.*, less noise due to configurational fluctuations).

2.2.2. Chain Anisometry

Chain anisometry (or "anisotropy") is usually represented by a descriptor of asphericity; *i.e.*, the deviation of the chain shape away from that of a sphere, (that is, an object with three equal principal moments of inertia) [Rudnick & Gaspari, 1986]. Asphericity describes the degree of oblateness or prolateness using the three principal moments of inertia, as follows:

$$\Omega = \frac{\{(\lambda_1-\lambda_2)^2+(\lambda_1-\lambda_3)^2+(\lambda_2-\lambda_3)^2\}}{2(\lambda_1+\lambda_2+\lambda_3)^2} \quad (2.7)$$

where $\{\lambda_i\}$ are the eigenvalues of the inertia matrix (or "principal moments of inertia"). An oblate shape is defined as being compressed or flattened along one of the axes, $\Omega \geq 0$, while a prolate shape is described as being elongated along one of the axes (**Figure 10**). The limits of asphericity in equation (4) are: $0 \leq \Omega \leq \frac{1}{4}$, where $\Omega = 0$ corresponds to a spherical shape and the limit $\Omega \to \frac{1}{4}$ corresponds to the limit prolate shape approaching that of a rigid rod.

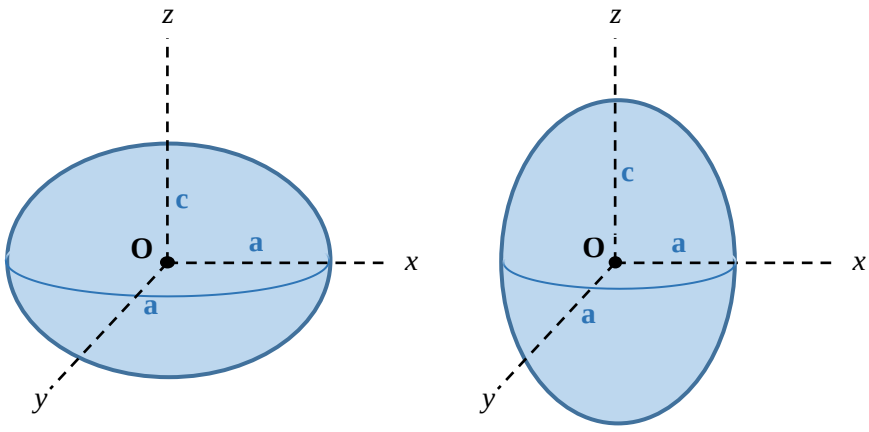

Figure 10: Schematic representation of chain asphericity. A polymer chain can adopt either an oblate (flattened, left) configuration, or a prolate (elongated, right) configuration. Prolate configurations are typical of high density brushes with repulsive interactions and no confinement. Oblate shape may appear in low-density brushes with repulsive and attractive interactions under compression.

2.2.3. Chain Entanglement Complexity

While the radius of gyration describes the mean molecular size, it does not include connectivity information for the polymer. In order to capture part of the topological confirmation, we can use a descriptor of entanglement. Chain entanglements are due to polymer chains interpenetrating each other (or themselves), possibly leading to either permanent or transient geometrical and topological constraints in chain motion [Arteca, 1999]. Entanglement complexity is a geometrical property that depends on both monomer positions and chain connectivity. By measuring the complexity of the entanglements within the chain, it is possible to discriminate among polymer configurations with similar size and globularity, yet different spatial organization and interpenetration patterns of chain loops.

Very often polymer chains adopt configurations with distinctive three-dimensional organizations or 'folds' with essentially the same molecular size and asphericity. These large-scale folding features are often elusive to quantify, even if they are visually apparent. A descriptor of chain entanglement captures some of these characteristics, in particular their interrelations in the presence of confinement (*cf.* the work done in the case of a single compressed polymer mushroom [Arteca, 1996b]).

Entanglements can refer to actual topological features such as knots or links in closed loops (ring polymers) [Arteca, 1999]. In open chains we find, however, *transient* entanglements between the chains, for example, by the formation of "tangles" (*i.e.*, "local knots") in linear chains [Kneller *et al.*, 2005]. Self-entanglements and inter-chain entanglements are normally characterized by the 'mean overcrossing number' (or 'average crossing number') using the projected bond-bond crossings, denoted by $\overline{N}$ [Arteca, 1994], [Arteca *et al*., 2001b] (see **Figure 11**).

The mean overcrossing number $\overline{N}$ measures the number of projected bond-bond crossings in a two-dimensional projection of the chain, averaged over all possible spatial projections [Arteca, 1999]. $\overline{N}$ is a convenient translationally and rotationally invariant descriptor of polymer shape. The probability of observing overcrossings increases as the chain becomes more entangled [Arteca, 1994].

To properly characterize the polymer brush, the descriptor $\overline{N}$ must be separated into intra-chain and inter-chain entanglements. The intra-chain contribution, for the C_k-chain among a set of N_C chains of length n is computed as [Arteca, 1999]:

$$\langle \overline{N}_{\text{intra}} \rangle_k = 2 \sum_{i=1}^{n-3} \sum_{j=i+2}^{n-1} \overline{N}_{ij} \quad \text{where } i, j \in C_k\text{-chain}, k=1,2,\ldots,N_C \qquad (2.8)$$

where the pair contribution $\overline{N}_{ij}$, corresponding to the mean overcrossing number between bond $i \to i+1$ and $j \to j+1$, is given by:

$$\overline{N}_{ij} = \frac{1}{4\pi} \int_0^1 \int_0^1 \frac{|(\dot{\boldsymbol{\gamma}}_i(s) \times \dot{\boldsymbol{\gamma}}_j(t)) \cdot (\boldsymbol{\gamma}_i(s) - \boldsymbol{\gamma}_j(t))|}{\|\boldsymbol{\gamma}_i(s) - \boldsymbol{\gamma}_j(t)\|^3} \mathrm{d}s\mathrm{d}t \qquad (2.9)$$

where γ_i represents the parameterized form of the bond vector connecting the i and $i+1$ monomers, while $\dot{\gamma}_i$ represents its parametric derivative.

$$\gamma_i : [0,1] \to \mathbb{R}^3, \gamma_i(0) = \mathbf{r}_i, \gamma_i(1) = \mathbf{r}_{i+1} \qquad (2.10)$$

In a polymer brush, the mean overcrossing number $\langle \overline{N}_{\text{intra}} \rangle$ measures the chain entanglement complexity by averaging over all chains and configurations (eq. 2.8), where N_C represents the number of polymers:

$$\langle \overline{N}_{intra} \rangle = \frac{1}{N_C} \sum_{k=1}^{N_C} \langle \overline{N}_{intra} \rangle_k \qquad (2.11)$$

In contrast, the average inter-chain entanglement $\langle \overline{N}_{\text{inter}} \rangle$ is determined by taking the summation of pair contribution $\overline{N}_{ij}$ over all different pairs of bond vectors belonging to two different molecules, chain *k,k'* [Carlsson *et al.*, 2011b]:

$$\langle \overline{N}_{\text{inter}} \rangle_{k,k'} = 2 \sum_{i=1}^{n-1} \sum_{j'=1}^{n-1} \overline{N}_{ij'} \text{ where } i \in C_k\text{-chain}, j' \in C_{k'}\text{-chain}; k' > k \qquad (2.12)$$

Contrary to intra-chain entanglements, *i* and *j'* in equation (2.12) refer to the bond crossings of different molecules. The inter-chain entanglement can be used to describe the bond-bond crossings within a given polymer island, and between different islands when introducing a second polymer covered surface.

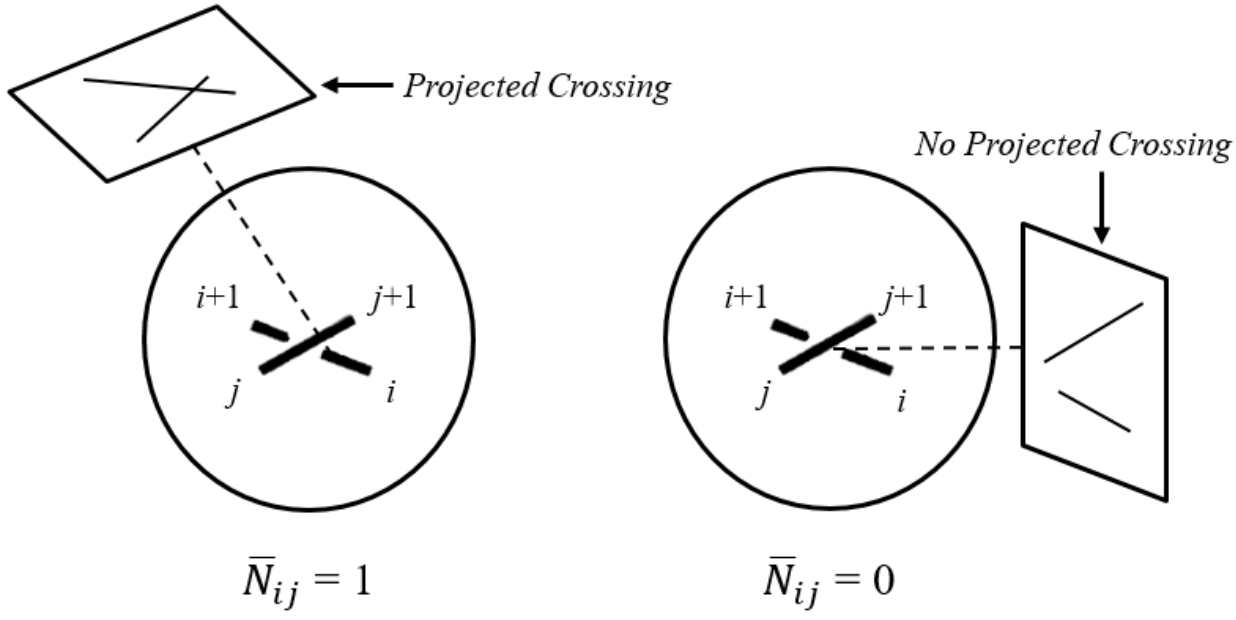

Figure 11: Schematic representation of projections that produce one overcrossing. In the right-hand side diagram, the overcrossing segments are closer to each other and yield a larger mean overcrossing number. Adapted from [Arteca *et al.*, 2001b].

The chain overcrossings are checked between all non-connected bonds since connected bonds are coplanar and cannot overcross. (See summation limits in eq. 2.8 and 2.12). For the

numerical computation of $\langle \overline{N}_{\text{intra}} \rangle_k$ and $\langle \overline{N}_{\text{inter}} \rangle_{k,k'}$ we use again the Marsaglia algorithm. With this technique, we choose a random viewing direction from where we construct a plane, tangent to sphere that encloses the entire polymer (Arteca, [1993], Arteca, [1996b]). All bond vectors are projected to this plane in order to determine the local number of overcrossings. Finally, the mean number of overcrossings is computed as an average over all viewing directions.

2.3. Detailed Models and Algorithms used in this Thesis

2.3.1. Polymer Model

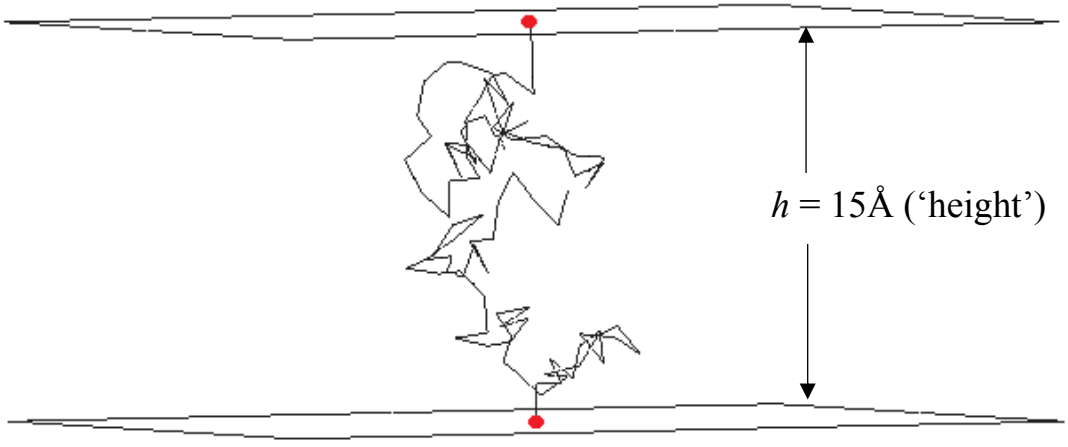

Figure 12: Two chains under compression. (The snapshot corresponds to *n* = 50 monomer beads, r_{ex} = 0.3Å, and constant bond length *l* =1.50Å. The two chains have the same *n*, r_{ex}, and *l* parameters.)

We first build a model consisting of two repulsive end-grafted chains placed directly above each other to study the effects of spatial confinement, **Figure 12**. Their equilibrium configurations were determined as explained in **2.2** as a function of the plate separation height (h), the number of beads per chain (n), and the r_{ex} value (the same for both chains).

In the first series of simulations, we examined chains with n = 20, 30, 40, and 50 beads per chain, at a constant bond length of l = 1.50Å. The anchoring position for the chains was fixed, and each n was tested under a variety of r_{ex}-values ranging from 0.1Å to 1.0Å at a fixed

plate separation. The simulations were then repeated at h values between 15Å and 50Å to determine an optimal height for inter-chain interactions.

In the second set of simulations, we studied two shifted chains under compression and observed their dependence on r_{ex}, h, and n (**Figure 13**). The bottom polymer chain was left unaltered, while the top chain was shifted away from the "local origin" at a distance (D) which varied from 1Å to 20Å. In this case, the "local origin" refers to the anchoring point of the top chain. The global laboratory-frame origin is at the anchor point of the bottom chain. In other words, the coordinates for the bottom anchor (bead 1) are (0,0,0), while the top anchor has (0,D,h), where D = 0 corresponds to the first series of simulations above (model in **Figure 12**). The same cases of n were studied as from the previous set of simulations, over a range of r_{ex} and h values.

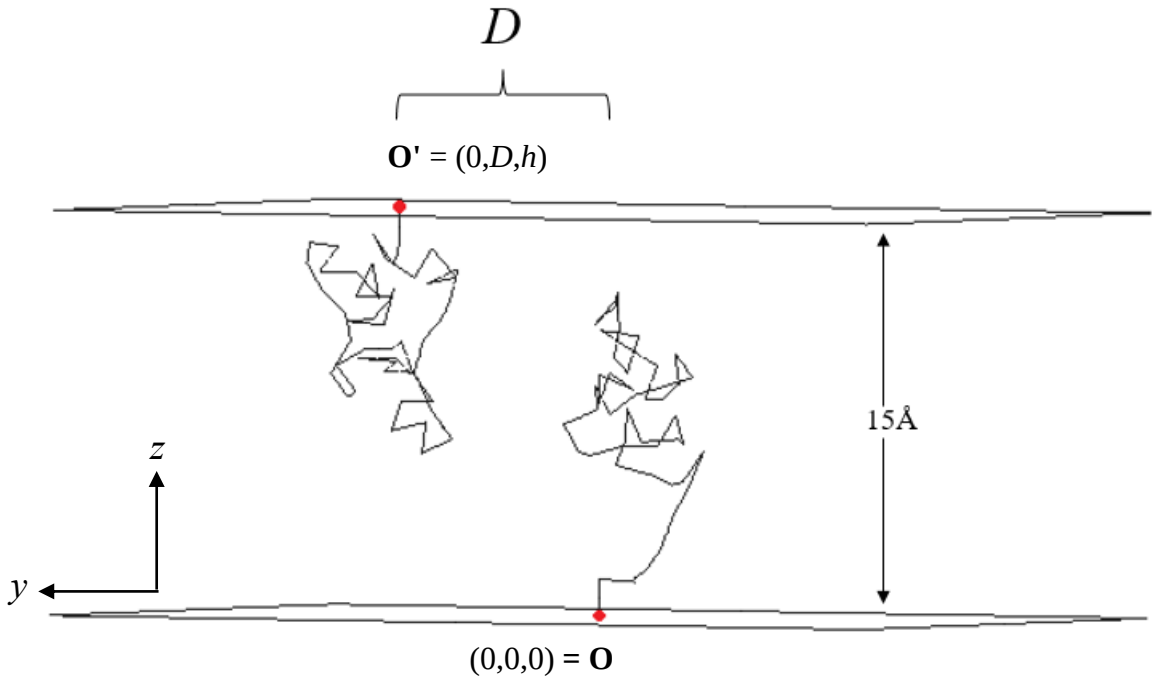

Figure 13: Two shifted chains under compression. (For n = 50 monomer beads, r_{ex} = 0.5Å, D = 8Å, and constant bond length l =1.50Å. The two chains have the same n, r_{ex}, and l parameters.)

In the third set of simulations, we studied two chains under compression and observed their dependence on the distinct chain lengths n_1 (bottom) and n_2 (top), as well as different r_{ex} interactions (**Figure 14**). The two chains were placed directly above each other with a constant

bond length l =1.50Å and h = 15Å. The bottom polymer chain (n_1) was kept at 50 beads throughout the simulation set, while the top chain (n_2) was tested at 20, 30, and 40 beads. Initially, we compared the different chain lengths (n_1 and n_2) at the same r_{ex} values, ranging from 0.1Å to 1.0Å. We also considered the case of n_1 = 50 and n_2 = 30 beads and varied the r_{ex} interactions between the two chains to observe the regions of high and low inter-chain interpenetration or entanglement (**Figure 14**).

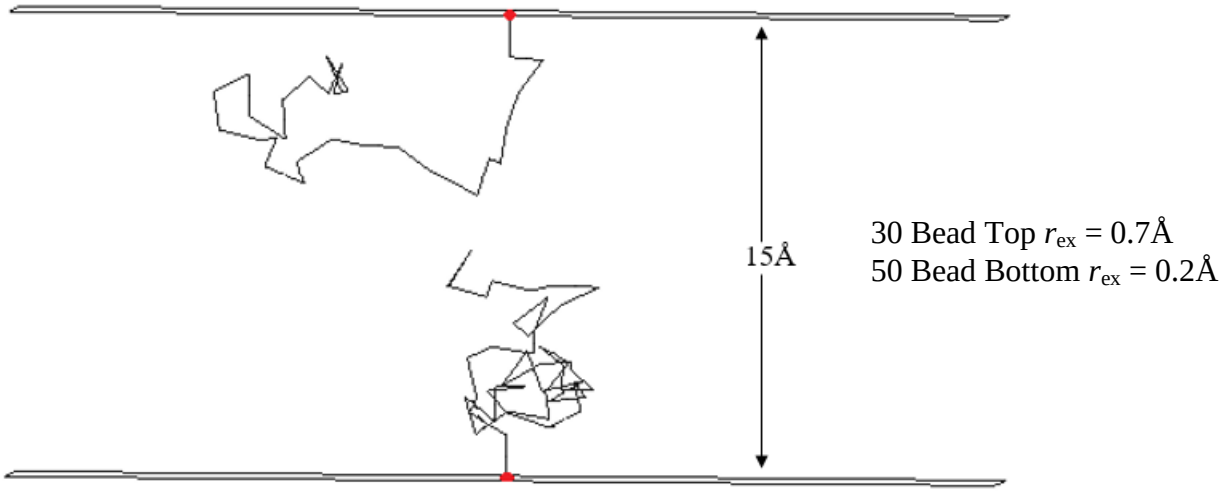

Figure 14: Two chains with different length and excluded volume under compression (for n_1 = 50 monomer beads (bottom), n_2 = 30 monomer beads (top), and constant bond length l =1.50Å).

In the fourth set of simulations, we studied three chains under compression and observed their dependence on their relative geometry (*i.e.*, the location of their anchoring point), r_{ex}, and D, (**Figure 15** and **Figure 16**). The chains were kept at n = 50 beads per chain at h =15Å and a constant bond length l = 1.50Å. Two geometries were compared, (**Figure 15**):

1) In one case, the grafting beads are in a plane perpendicular to the confining surface ("linear configuration", **Figure 15**, left),
2) In the second case, the anchoring beads are in a non-perpendicular plane ("triangular configuration", **Figure 15**, right).

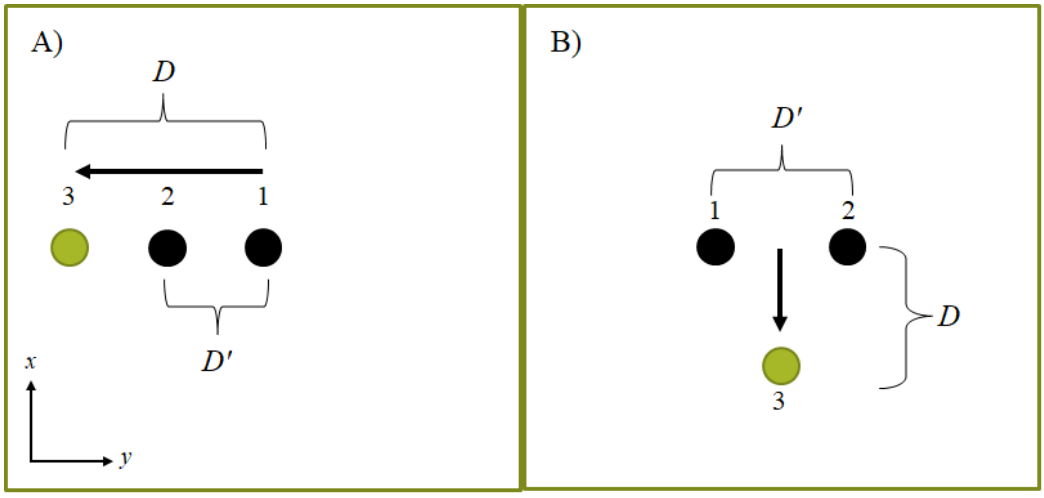

Figure 15: Three chain packing geometries, A) linear, B) triangular. The black circles represent the anchor beads for the two chains on the top plane, while the green circle is the anchor for the bottom chain.

Throughout both simulation sets, the anchoring positions of the top chains were fixed, while the bottom chain was moved a distance (D) ranging from 0Å to 6Å. In the first case, **Figure 15A**, the first top chain (chain 1) is anchored at the origin while the second top chain (chain 2) is anchored at a fixed distance (D') 3Å away. In the second case, **Figure 15B**, the two top chains (chains 1 and 2) are still separated by 3Å, however the anchoring location was shifted away from the origin by 1.5Å, left and right, allowing the bottom chain (chain 3) to pass through the origin, when seen from above. The r_{ex}-values for both geometries was varied from 0.1Å to 0.5Å. The location of the corresponding anchor beads is as follows:

"Linear": $O_{3,Bottom} = (0,D,0)$ $O_{1,Top} = (0,0,h)$ $O_{2,Top} = (0,D',h)$

"Triangular": $O_{3,Bottom} = (D,0,0)$ $O_{1,Top} = (0,-\frac{D'}{2},h)$ $O_{2,Top} = (0,+\frac{D'}{2},h)$

A representative configuration for the 3-chain system in "linear configuration" appears in **Figure 16**.

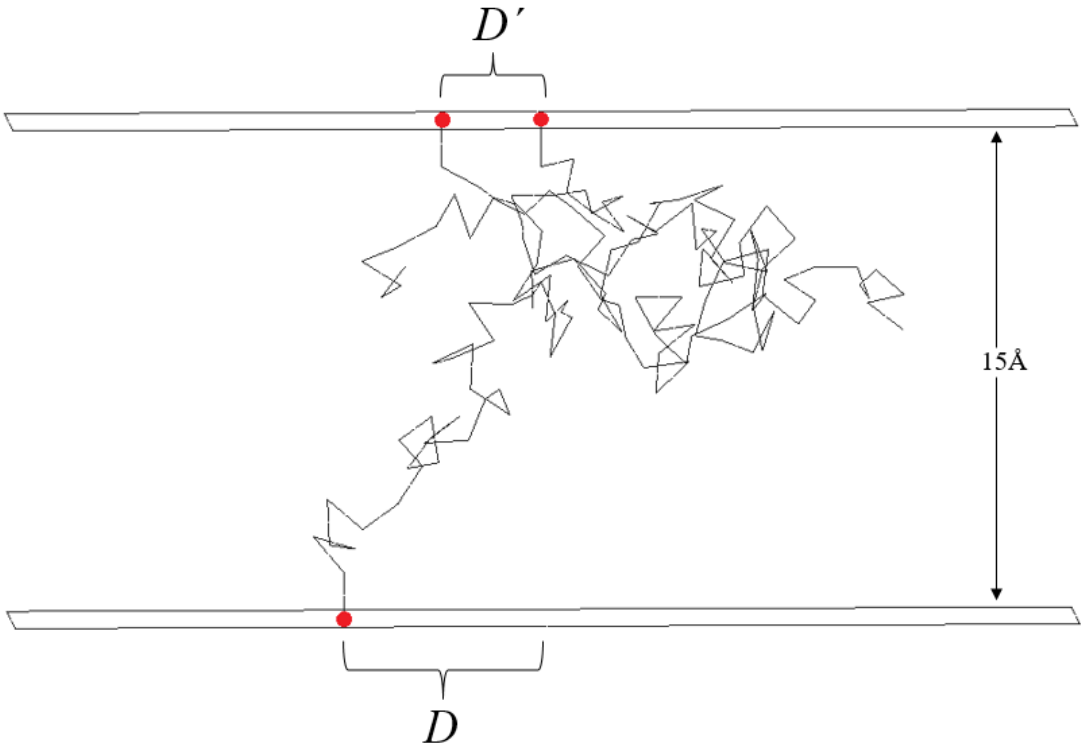

Figure 16: Sliding simulation with three chains in the "linear" geometrical arrangement (*cf.* Figure 16), n = 50 beads per chain, r_{ex}=0.5Å, D = 6Å, D'= 3Å

In the fifth set of simulations, we investigated the molecular shape of seven identical polymers chains when they are compressed by a coated top wall at h = 15Å (**Figure 17**). In this case, chain 1 is anchored at the top plane, while chains 2-7 are anchored at the bottom, with their grafting points arranged in a regular hexagonal configuration. In this particular simulation series, each chain had n = 20 beads, excluding the anchors. The distance D between the bottom anchors and the center of the hexagon varied from 3Å (high confinement) to 15Å (low confinement). The top chain is anchored at a point that is vertically (along the z-direction) above the center of the hexagonal arrangement of anchors on the bottom plane.

We test this condition, at several r_{ex}-values ranging from 0.1Å to 0.4Å. The case, r_{ex} = 0.5Å was not performed since the number of rejected configurations makes any calculation with D < 5Å computationally impractical at high compression. For instance, the equilibrium calculation for D = 5Å at h = 15Å (high confinement) requires over 72 hours of CPU in our computers.

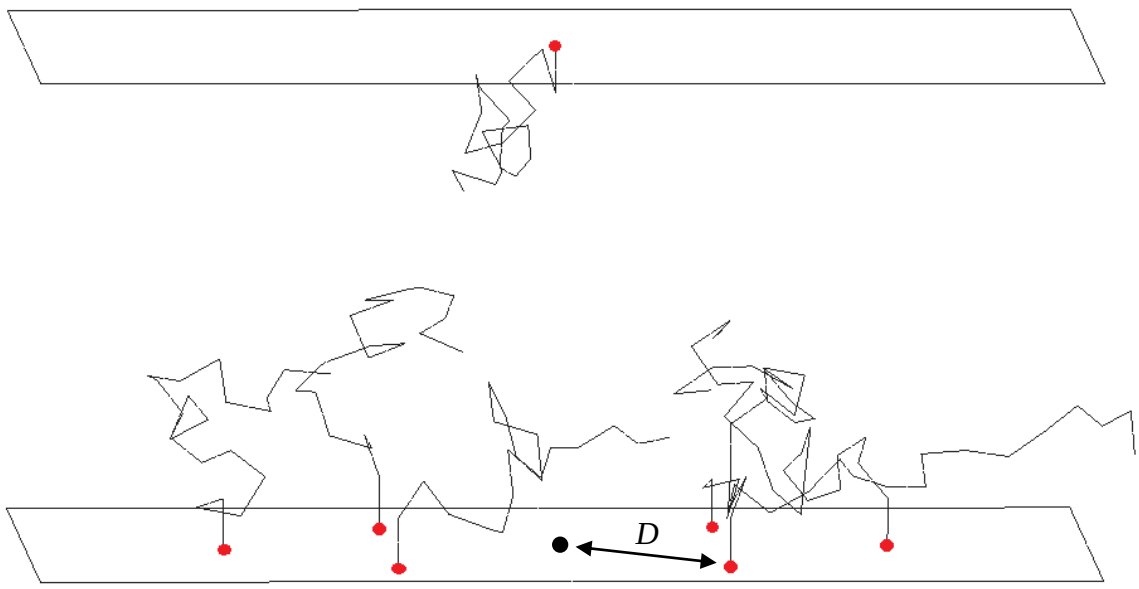

Figure 17: Model used for seven chains under compression. This representative snapshot corresponds to h = 15Å, n = 20 beads per chain, r_{ex} = 0.4Å, D = 10Å and l = 1.50Å.

In chapter 3 we relate the results from this series of simulations to trajectories run without spatial confinement (*i.e.*, without an upper wall) conducted previously in our laboratory [Harrison, 2014], [Richer *et al*., 2017]. In this case, we looked at the equilibrium shapes of seven polymer chains grafted in a hexagonal arrangement on one plane (*i.e.*, the "pivot" chain located in the middle of the hexagonal configuration at the bottom plane). In this thesis, we examine the effects of bringing chain 1 (*i.e.*, top grafted chain) closer to the bottom polymer island (chains 2-7) and study how the chains reorient themselves with respect to each other in order to accommodate the loss in space. We use the uncompressed seven chain results as a "baseline" to qualitatively compare the series conducted in this thesis.

2.3.2. Computational Details

All simulations were conducted using three FORTRAN-programs written by Dr. Arteca, with modifications and input-output adaptations done by myself. The first program (*MC_polymer-trajectory_generator_2-plates_Lecuyer_siv2_Gustavo_v5_TEST.f*) generates the MC trajectories for the repulsive polymers using the Marsaglia algorithm (**Appendix 1**). The

program creates a chosen number of chain configurations and writes them to an output file as a series of *x*, *y*, *z* coordinates. An illustrative example of input data for the trajectory generating program is given in **Figure 18**.

```
6                |        Number of chains bottom (n_chainb)
2500             |        Number of conformers per trajectory (n_conf) (having top and bottom chains)
1                |        Number of trajectories (n_traj)
20               |        Number of beads per chains (n_lengthb, excluding anchor), top/bottom may be unequal
1.50d0           |        Constant bond length (r_bondb)
0.40d0           |        Excluded volume (r_exclb)
075403           |        i2_seed for RNG (ran_2)
'Traj_04_top-plate-15_beads-20_7-chains_dist-6_excl-0.4.dat'   |        Full output file with all trajectories
1                |        Full restart-1 vs restarting with same bottom-2 (Restart_answer)
YES              |        YES/NO to the presence of the top wall (Wall_answer)
15.d0            |        Distance/height of the top wall (height_L)
1                |        Number of chains top (n_chaint)
20               |        Number of beads per chains (n_lengtht, excluding anchor)
1.50d0           |        Constant bond length (r_bondt)
0.40d0           |        Excluded volume (r_exclt)
-3.0     5.1961524     0.0      |    First grafting anchor bottom
 3.0     5.1961524     0.0      |    Second grafting anchor bottom
 6.0     0.0           0.0
 3.0    -5.1961524     0.0
-3.0    -5.1961524     0.0
-6.0     0.0           0.0
 0.0     0.0          15.0
```

Figure 18: Input data file for the Monte Carlo trajectory generating program (Appendix 1)

The second program named (*allxs-scan-trajectory_inter-intra_overcrossings_Gustavo_v4_GENERALIZED.f*), uses the output from the first program and then characterizes the size, anisometry, and entanglement complexity of each chain as well as the average values and statistical fluctuations in the MC set to another output file (**Appendix 2**). The final program (*allxs-scan-trajectory_version_with_interchain_overcrossings_for_the_pivot_Gustavo_v3_GENERALIZED.f*) evaluates the mean inter-chain entanglements between each polymer chain and the pivot chain, which is specified in the command file, to a third output file (**Appendix 3**). The computation of the inter-chain descriptor $\langle \overline{N}_{inter} \rangle$ is performed by a different program; program 2 computes properties averaged *per chain*, while program 3 deals with *pairs of chains*.

For all the simulations performed in this thesis, the constant bond length was set to l = 1.50Å, which is comparable to an average carbon-carbon single bond. Recall that the radius of the excluded volume can have a maximum value of 2l, *i.e.*, r_{ex} = 3Å, before the chain is forced to adopt a single linear configuration. In practice, the large number of rejections due to excluded

volume renders the conformation search impractical for r_{ex} > 1.0Å, in the case of two chains. For r_{ex} = 1.0Å, the MC calculations required over 24 hours of CPU time on a SUN-UNIX workstation to generate 2500 independent configurations for each chain. The computational demand would be much greater for larger r_{ex}-values, as well as for more crowded chain configurations (*i.e.*, more chains) since the decreasing available configurational space by compression, or increasing the number of beads per chains, increases rapidly the number of rejected configurations. As a result, the maximum excluded volume we could handle in the three chain simulations was r_{ex} = 0.5Å (72 hours of CPU time). For illustration, **Figure 19** shows the typical exponential growth in the number of rejected configurations in our simulations.

The smallest excluded volume used throughout this thesis was r_{ex} = 0.1Å, which produces nearly random walks (that is, chains slightly above the Θ-temperature).

The figures shown in the previous section **2.3.1** (excluding **Figure 15**), illustrate typical snapshots from each simulation model under the various confinement conditions. These representations were completed using the program HyperChem 8.0 [Hypercube Inc.]. The output from the MC program was translated for HyperChem using a fourth program named (*trans-hin-3d_multichain_Gustavo.f*), which was written by Dr. G. Arteca.

Equilibrium configurations were determined from a full sequence of 2500 MC independent and uncorrelated configurations. This sequence constitute an 'MC trajectory', since it is the limit of the Metropolis algorithm (Sec. 2.1.3) for a hard-sphere potential (Sec. 2.1.4). Each different initial configuration and geometrical arrangement involved a new independent MC trajectory. For each trajectory, different initial random seed numbers were used to avoid any repetitions. Using this approach, we computed the average size, self-entanglement, anisometry, and relative chain orientation. WinSCP was used to transfer the files from UNIX to Microsoft Windows, and the text documents were imported into Microsoft Excel. The mean value for each descriptor was calculated along with the fluctuation taken at 95% confidence.

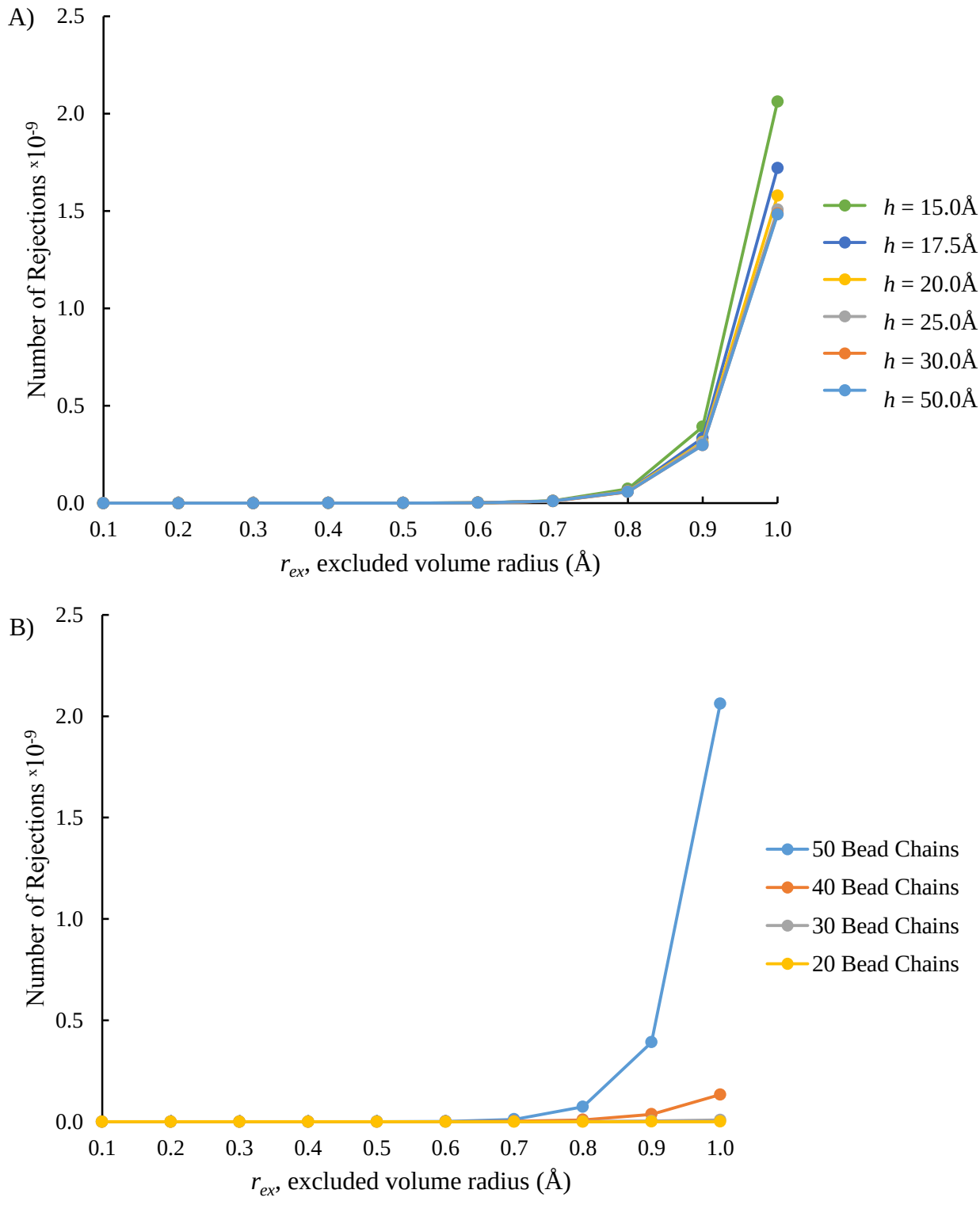

Figure 19: Two chain plots of rejection versus r_{ex} for, A) various plate separation distances at n = 50 beads per chain, B) different number of beads per chain at h = 15Å. Observe that chain length has a bigger effect on rejection than confinement. Note that n > 50 beads cannot be handled at high confinement and excluded volume with the algorithms used in this thesis.

2.4. Configurational Search: A Summary

For completeness, we summarize here the algorithm for generating the configurations. Note again that in presence of hard-sphere (or "excluded-volume") interactions, the Metropolis-Hastings algorithm in Sec. **2.1.3** is reduced to the simplified search detailed in Sec. **2.1.4** (often called a 'naïve Monte Carlo approach" [Allen & Tildesley, 1991]):

1) The first bead is grafted to the surface at a specified location (with a height $z = 0$).
2) The second monomer is attached to the first with the same x and y coordinates but at a height $z = 1.50$ Å.
3) From the third monomer, the bead is located on a sphere of radius l=1.50 Å with a centre at the second bead using the Marsaglia algorithm (**Figure 8**). The remaining beads are located from the previous one using the Marsaglia algorithm, subject to the check of excluded volume.

As discussed earlier, the distance between the third and first bead is checked; if the distance is smaller than the radius of excluded volume the configuration is rejected and the walk restarts. If the distance is greater, the partial geometry is accepted and another bead is linked to the previous in the same approach, and the contacts with all non-bonded beads are checked. The procedure continues until a successful complete configuration with n beads has been generated (**Figure 6**). Each new chain in the polymer cluster is built in a similar fashion (top chains are built with the anchor bead set at $z = h$, corresponding to the height of the top plate). In all cases, we check if the excluded volume condition is satisfied with the already accepted chains and in all cases we maintain the impenetrability of the confining and grafting planes.

Chapter 3

3. Results

The two main objectives of this thesis were:

1) To determine the conditions that disfavor chain interpenetration (in terms of inter-chain entanglements) as a function of plate separation height (h), chain length (n), excluded volume (r_{ex}), chain location (D), and finally the geometry of neighbouring chains.
2) To determine the nature of the dominant configurations observed in any of these conditions, as characterized in terms of various shape descriptors.

Throughout this chapter, we examine the effects produced by confinement between two polymer covered surfaces. (Refer to section **2.3.1** for details of the polymer models used). Throughout sections **3.1** to **3.3**, we studied the molecular shape descriptors when each surface was coated with one polymer mushroom. In section **3.4** we examine three chains under compression and compare intra- *vs*. intermolecular shape, as well as the role of chain geometry on the chains shape. Finally, in section **3.5** we study seven chains under compression in hexagonal packing and compare the results to data previously obtained in our lab for a similar arrangement without compression.

Throughout each set of simulations, we gather insight into the nature of dominant configurations for chain avoidance. **Figures 20-42** represent a selection of the main results generated from our computer simulations. A brief introduction to the significance and interpretation of these results is provided at the start of each subheading, in addition to the figure captions provided. A more detailed discussion is found in chapter 4. Note that all results are presented with 95% confidence intervals, with the exceptions of **Figures 32** and **37**.

3.1. Two Chains Under Compression

To begin, we look at two chains, l =1.50Å, grafted to opposite planar hard surfaces and studied their molecular shape. (The two chains have the same n and r_{ex} parameters, but they are generated always in different configurations.) In **Figure 20**, we compare the molecular shape descriptors, asphericity (shown on the left) and radius of gyration (shown on the right) of two identical 50-bead chains, located directly above one another at a plate separation distance of 15Å. As r_{ex} increases, the chains begin to swell and we observe that asphericity and radius of

gyration both increase at a similar rate. Thus, the chains become both longer (with respect to mean size) and more prolate in shape.

In **Figure 21**, we compare inter-chain (shown on the left) and intra-chain (shown on the right) entanglements, measured in terms of mean overcrossing numbers for two identical 50-bead chains at a plate separation distance of 15Å (same case as previous figure). As r_{ex} increases, the intra-chain entanglements (or "self-entanglements") decrease, thereby indicating that individual chains swell and begin to disentangle. The intermolecular shape is affected in a subtler way. From the figure, we observe that the inter-chain entanglement decreases slightly (compared to intra-chain). Given that all chains swell and disentangle, the decrease in inter-chain entanglement suggests *chain avoidance*.

Next, we look at varying compression and chain length to observe the consequences on inter-chain entanglements. In **Figure 22**, we compared the inter-chain entanglement at two different plate separation heights, 30Å (weak compression, shown on the left) and 15Å (strong compression, shown on the right) at several chain lengths (20, 30, 40, and 50 beads per chain). Examining the larger plate height, h = 30Å, we observe also an increase in the inter-chain entanglement for all the chain lengths as r_{ex} increases (*i.e.*, chains swell). As expected, we note also longer chains entangle more with each other.

Comparing those results to h = 15Å, the shorter chains (20 and 30 beads) follow the same trend as in h = 30Å, whereby they *entangle more* with each other as they swell with increasing r_{ex}. However, for 50-bead chains (seen previously in **Figure 21**) the inter-chain entanglement *decreases* with r_{ex}. This difference in behaviour implies that the chains swell but do not overlap under confinement, *i.e.*, the chains avoid each other. The inter-chain entanglement trend for 40 beads per chain (at h = 15Å) is notable since the inter-chain entanglement is *nearly constant*, indicating some chain avoidance is occurring but to a far lesser extent than for the longer chains. In other words, when confinement is imposed we observe that there is a critical length (possibly $n \cong 40$) at which swelling chains switch from *entangling more* with each other as they overlap, to *entangling less* by avoiding each other. It is possible that a similar critical chain length exists for h = 30Å, but it will be for $n > 50$.

Consequently, we investigate the longest chain length (n = 50 beads) at several plate separation heights to determine at what height we begin to observe chain avoidance. **Figure 23** compares the effect of compression and r_{ex} on inter-chain entanglement for two chains on

opposite plates. At the lowest compression (h = 50Å), chains are too far away, so as r_{ex} increases and chains swell, there is no appreciable effect of inter-chain entanglement. For h = 30Å to h = 20Å, the inter-chain entanglement still increases with increasing r_{ex}. However, at h = 17.5Å, the inter-chain entanglement plateaus in the same way as the case of 40 beads per chain for h = 15Å, **Figure 22**. Finally, at h = 15Å the inter-chain entanglement decreases with r_{ex} due to stronger chain avoidance. This result complements the observation in **Figure 22**, as it shows that, for a fixed chain length, there is a critical compression (*i.e.*, a critical h-value) at which we see the switch from *chain overlap* to *chain avoidance*.

Figure 24 shows how compression affects the intramolecular shape of the chains. We compared the radius of gyration (shown on the left) and intra-chain entanglement (shown on the right) of n = 50 bead case at several heights (15, 20, and 25Å, respectively) to see how the individual chain shape was affected. As observed in earlier figures, chain swelling (increasing r_{ex}) resulted in a larger mean chains size as the chains untangled, decreasing in intra-chain entanglement. Overall, the effect elicited by compression on individual chain shape is minimal, excluded volume being the main controlling factor for chain shape. Comparing the three different plate heights, the mean chain size increased slightly with reduced compression while the chain self-entanglement produced essentially the same trend. These trends indicate that the role of compression in changing the inter-chain entanglement is not due to a qualitative change in configuration (as it is in the case of escape transitions) but rather the relative rotation of chains trying to avoid each other.

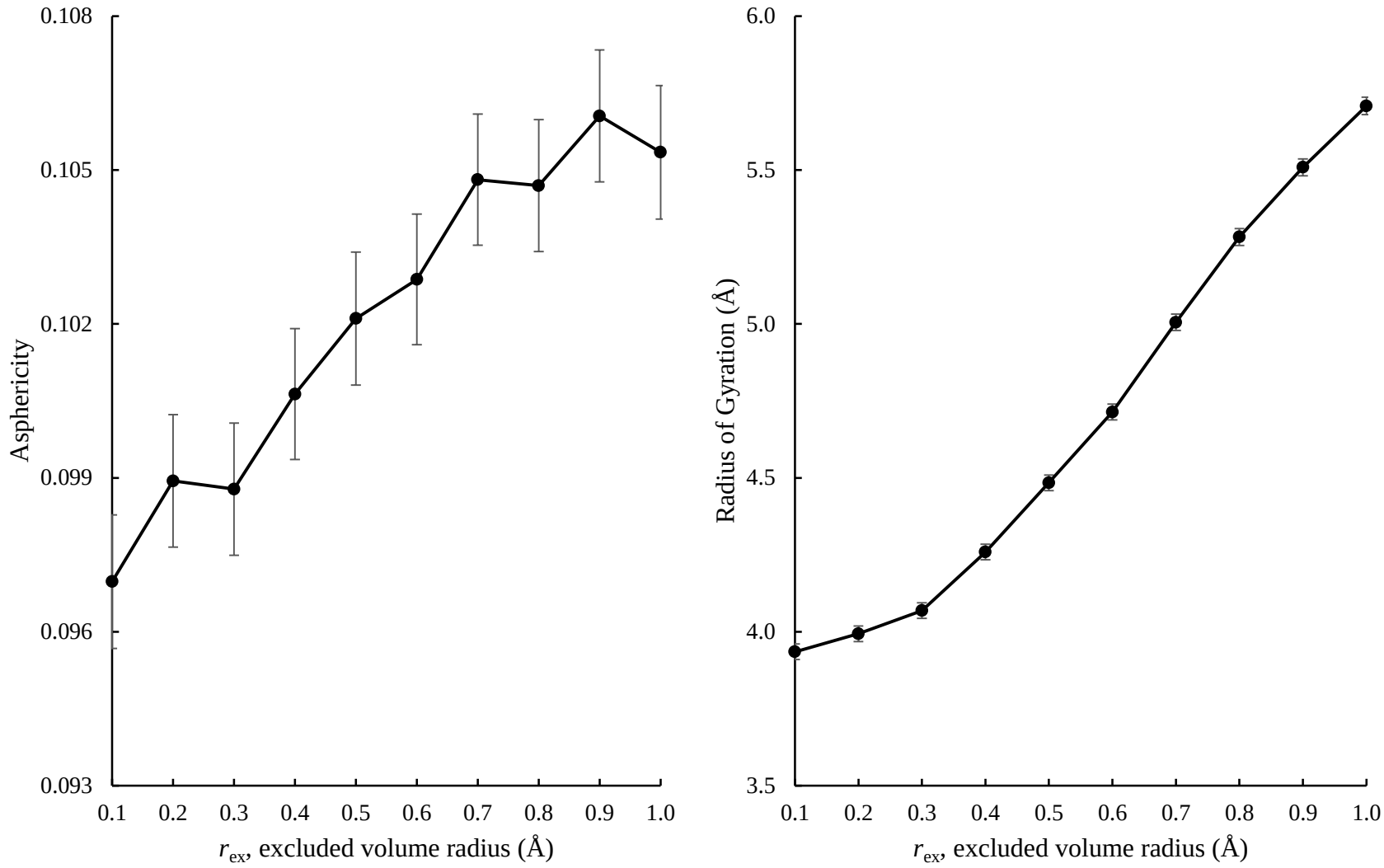

Figure 20: Comparison of r_{ex} on asphericity [left] and radius of gyration [right] of n = 50 beads per chain at h = 15Å (high compression). The results are averaged over the two present chains, one grafted to each corresponding plate (model in Figure 12). Swelling causes the polymer chains to become more elongated in shape and expand in size.

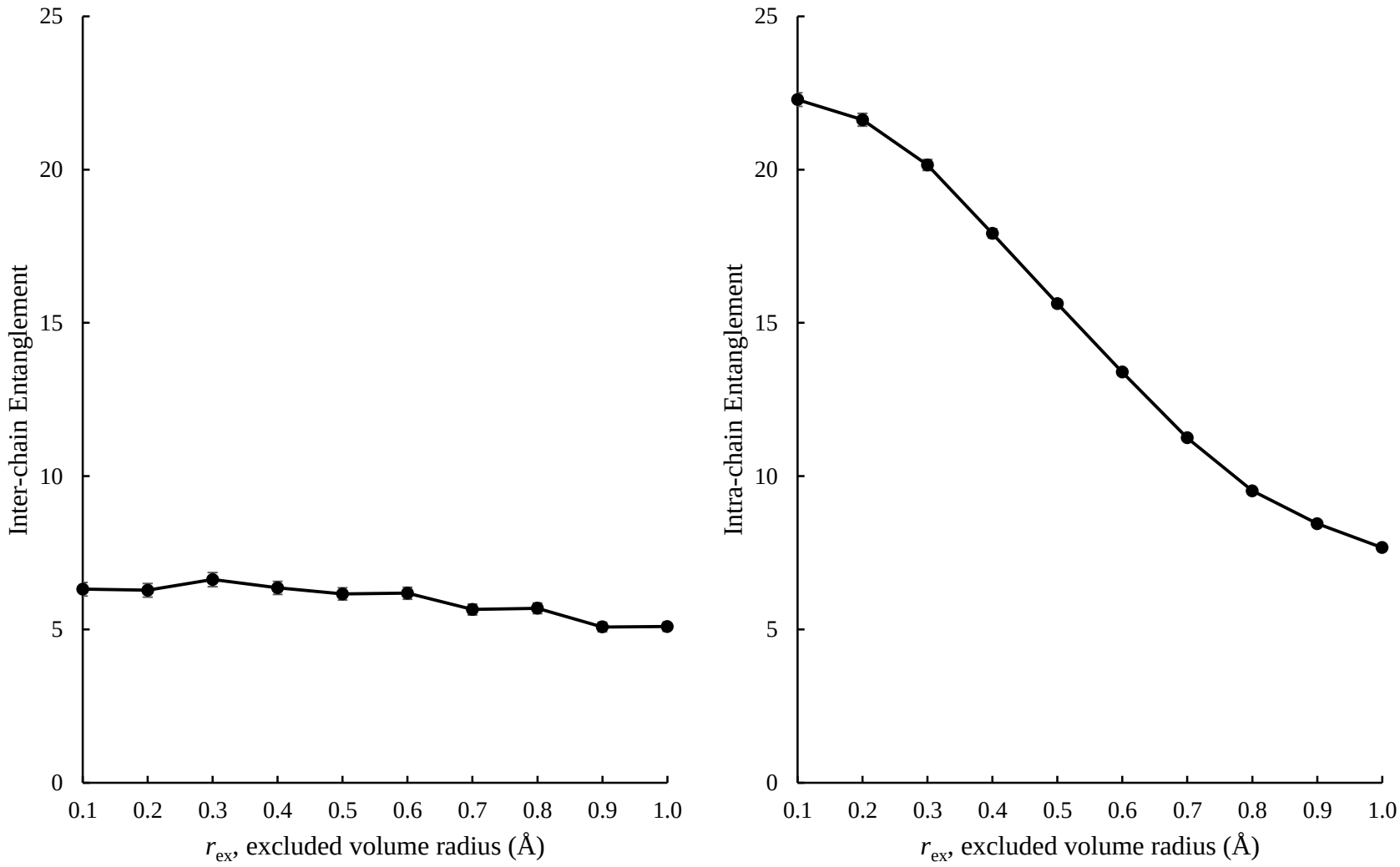

Figure 21: Comparison of r_{ex} on inter-chain [left] and intra-chain [right] entanglements at n = 50 beads per chain and h = 15Å (high compression). Swelling causes a polymer chain to untangle with itself, as well as with the neighbour chain on the top plane (model in Figure 12).

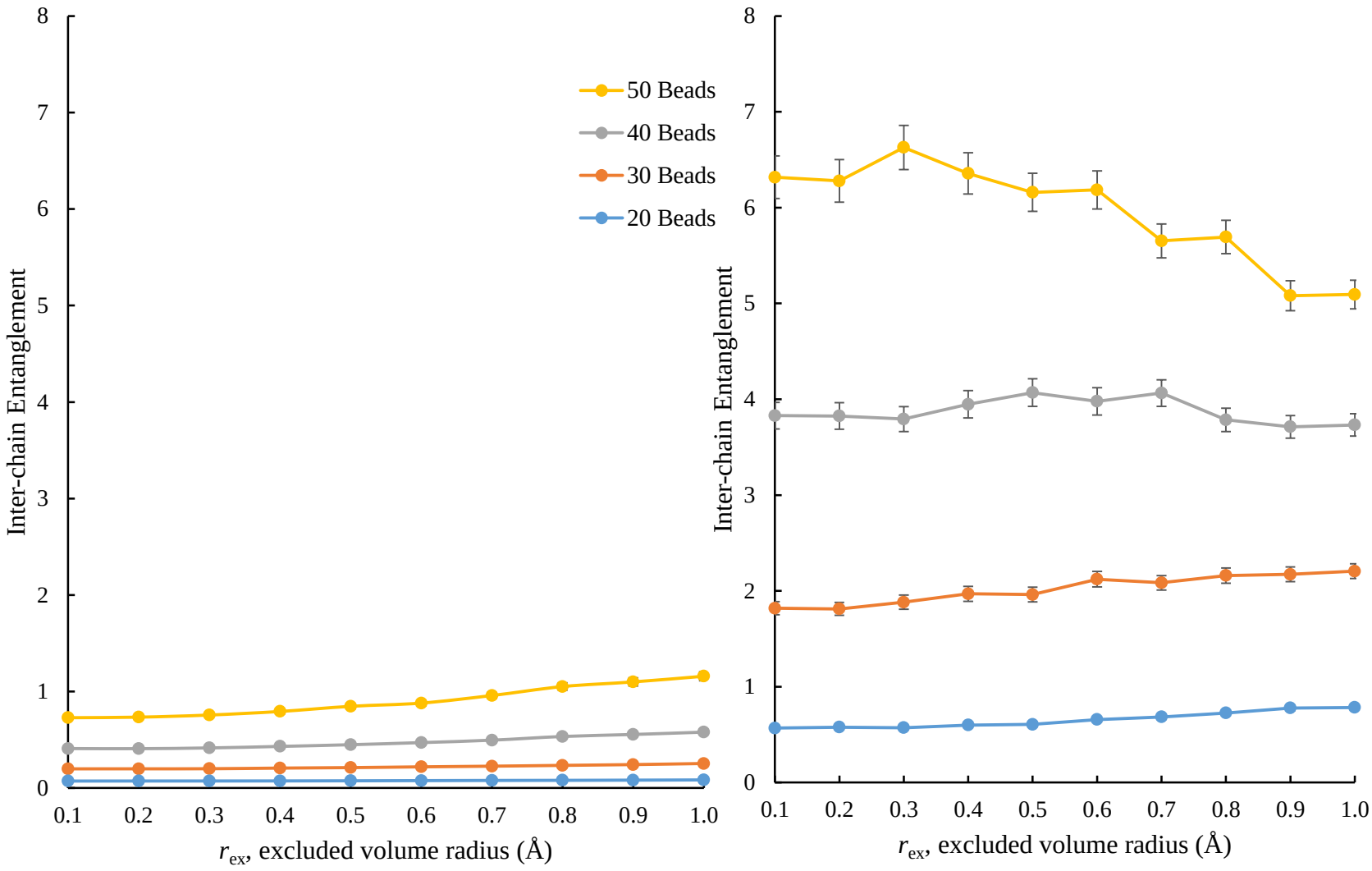

Figure 22: Effect of varying chain length, *n*, and r_{ex} on the inter-chain entanglement for the model of two grafted chains directly opposite to each other (model in Figure 12), [left] *h* = 30Å (low compression), and the [right] *h* = 15Å (high compression).

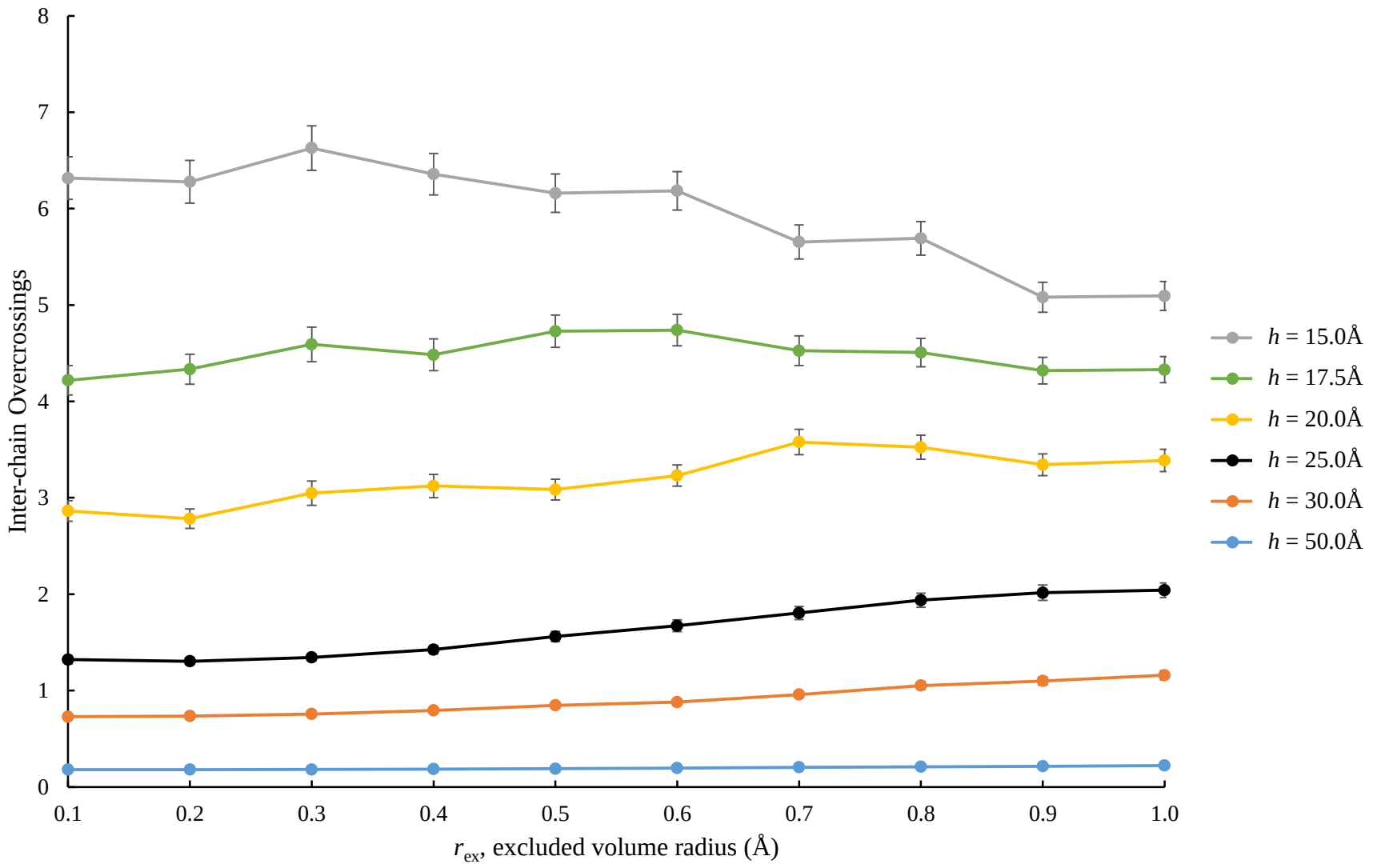

Figure 23: Effect of various plate separations (*h*) on inter-chain entanglement at *n* = 50 beads per chains (model in Figure 12).

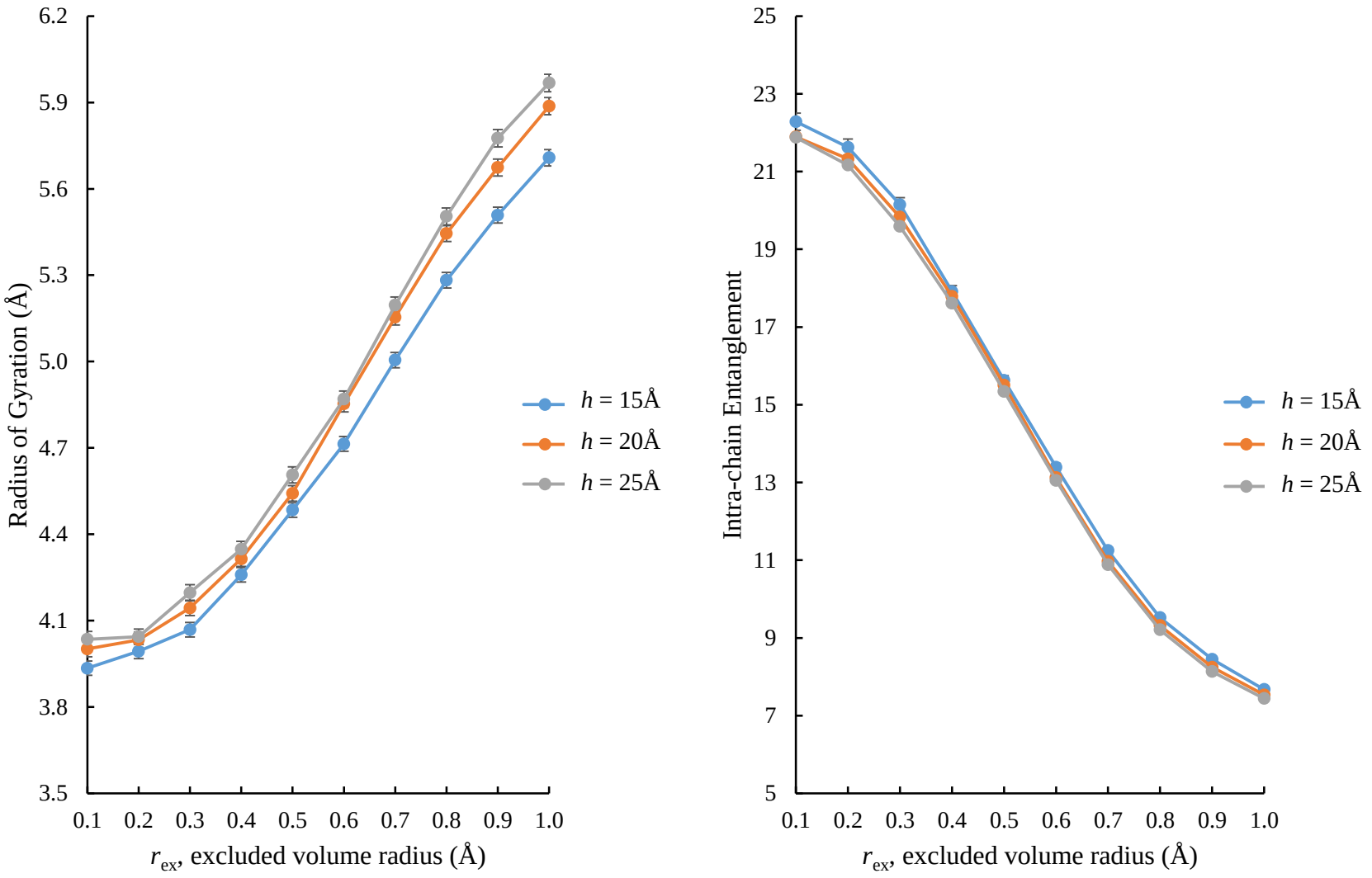

Figure 24: Effect of compression on radius of gyration [left] and intra-chain entanglement [right], at *n* = 50 beads per chain (model in Figure 12).

3.2. Effect of Lateral Displacement on the Compression of Two Chains

In **Figure 25**, we compare radius of gyration (shown on left) and inter-chain entanglement (shown on right) of n = 50 beads at h =15Å and two different r_{ex}-values (0.5 and 1.0Å), as the top chain slides away from the origin, D, as explained for the model in **Figure 13**.

In terms of mean size, as expected, the larger r_{ex} value produces the largest chains. (See typical structures illustrated with the visualization insert generated with the HyperChem program). The inserts correspond to pairs of chains shifted at D = 4Å (A and C) and D = 14Å (B and D), for the two values of excluded volume. It is interesting to note that intramolecular structure is *unaffected* by shear displacements while the inter-chain entanglements are affected in both value and trend. Note that the less swollen chains (r_{ex} = 0.5Å) entangle more when the chains are closer to one another, D < 9 Å; beyond this distance, the more swollen chains (r_{ex} = 1.0Å) entangle more. Given that the left-hand side diagram in **Figure 25** indicates that the individual chain shape is unaffected, the change in inter-chain entanglement has to be the result of how chains are positioned relative to each other, *i.e.*, in terms of overlapping or avoiding each other. The smaller number of entanglements of the swollen chains at D < 9Å can be attributed to chain avoidance while, at D > 9Å swelling allows chains to reach each other and to interact more. In other words, at short D-values, swollen chains (*i.e.*, r_{ex} = 1.0Å) must rotate away from each other as a result of inter-chain excluded volume, leaving the small inter-chain entanglements. On the other hand, for large D-values, only longer and larger chains can overlap each other when displaced away, hence it is the more compact chains (*i.e.*, r_{ex} = 0.5Å) that entangle less with each other. The right-hand side of **Figure 25** indicates that there is a critical distance D at which a crossover between these two trends takes place. Eventually, at very large D-values we will have two isolated polymer mushrooms.

In **Figure 26**, we examine the effect of different r_{ex}-values (0.3Å and 0.4Å) and shear displacements on inter-chain entanglement at n = 50 beads per chain to see if they would also display the crossover behaviour and at which distances it occurred. Like the previous figure, the compact chains entangled more when the chains are near one another, D < 9Å, while swollen chains entangled more at greater shearing displacement, D > 9Å. The inter-chain entanglements cross at approximately the same r_{ex}-value, possibly indicating a critical distance at which chain avoidance becomes the prevalent factor on $\langle \overline{N}_{inter} \rangle$.

Figure 27 complements the above analysis, by showing the results for shorter chains, n = 40 beads (shown on left) and n = 30 beads (shown on right). **Figure 27** shows that at h = 15Å, the longer chains (40 beads per chain) still display the crossover effect, seen in **Figure 26**; however, this effect is lost for the shorter chains (30 beads). The more compact chains (r_{ex} = 0.5Å) always entangle less than swollen chains (r_{ex} = 1.0Å) if they are sufficiently short. For longer chains (like n = 40 beads), the compact chains entangle more if they are grafted sufficiently close to each other (*i.e.*, D < 6Å), while at greater distances swollen chains entangle more.

These results confirm the picture of inter-chain entanglement arising from the interplay between chain avoidance and overlap: if short chains are too far apart, no amount of swelling will be sufficient for overlap. On the other hand, it is possible that the behaviour for n = 30 in **Figure 27** (right) will exhibit a similar trend as that for n = 40 in **Figure 27** (left) if the compression were stronger (*i.e.*, h < 15Å). Ultimately, however, no amount of physically reasonable compression will be sufficient for the inter-chain entanglement of short, isolated mushrooms.

Finally, **Figure 28**, compares longer chains at smaller compression (n = 50 beads at h = 15Å, shown on right) to shorter chains at higher compression, (n = 40 beads at h = 10Å, shown on left). In terms of value and trend, the two cases resemble each other very closely: they both cross at approximately the same distance ($D \approx 9$Å) and the $\langle \overline{N}_{inter} \rangle$-values are comparable (except that shorter chains entangle less for small D and r_{ex} values). As in previous figures, when the chains are less swollen (r_{ex} = 0.5Å) and at sufficiently close distances, they entangle more than the more swollen chains (r_{ex} = 1.0Å) at low D values. The behaviour is inverted at large D values, since only the more swollen are able to reach each other to entangle to any significant extent.

This coincidence, and the comparable values of inter-chain entanglement, suggest that n = 50 at h = 15Å is found in a sort of "equivalent configurational state" to the chain with n = 40 at h = 10Å. Loosely speaking, this resembles the thermodynamic case of two real gases with different molecular interactions yet producing the same observable (*e.g.*, pressure) at different values of the control variables (*e.g.*, temperature or volume). In our case, chains with similar interactions but different lengths are found at the same "configurational corresponding state" at different levels of compression.

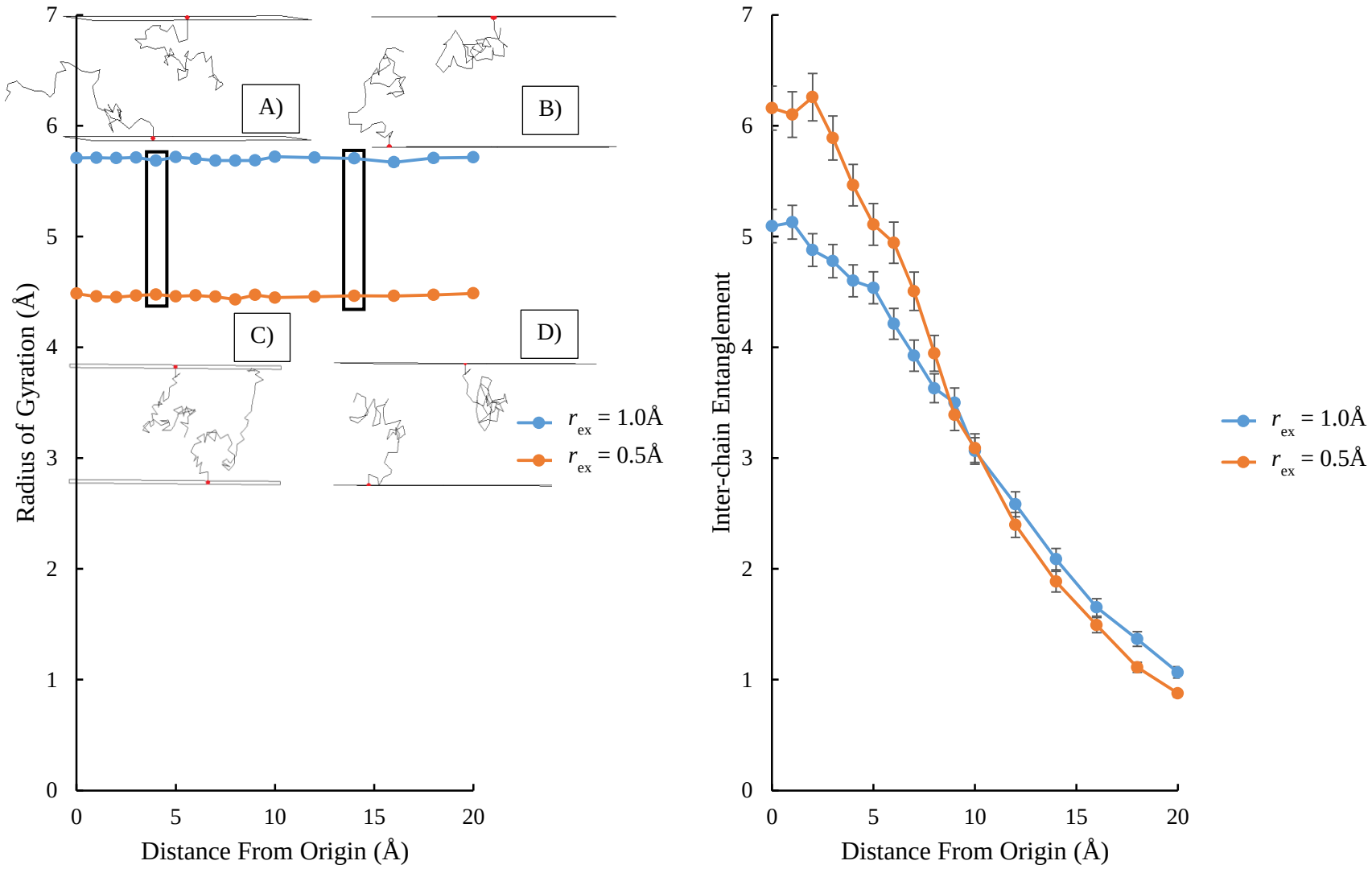

Figure 25: Comparison of r_{ex} on radius of gyration [left] and inter-chain entanglement [right] for two sliding chains n = 50 beads at h = 15Å (model in Figure 13). The structural inserts illustrate typical shapes for different r_{ex} and D values. The inserts A) and B) correspond to r_{ex} = 1.0Å, while C) and D) correspond to r_{ex} = 0.5Å.

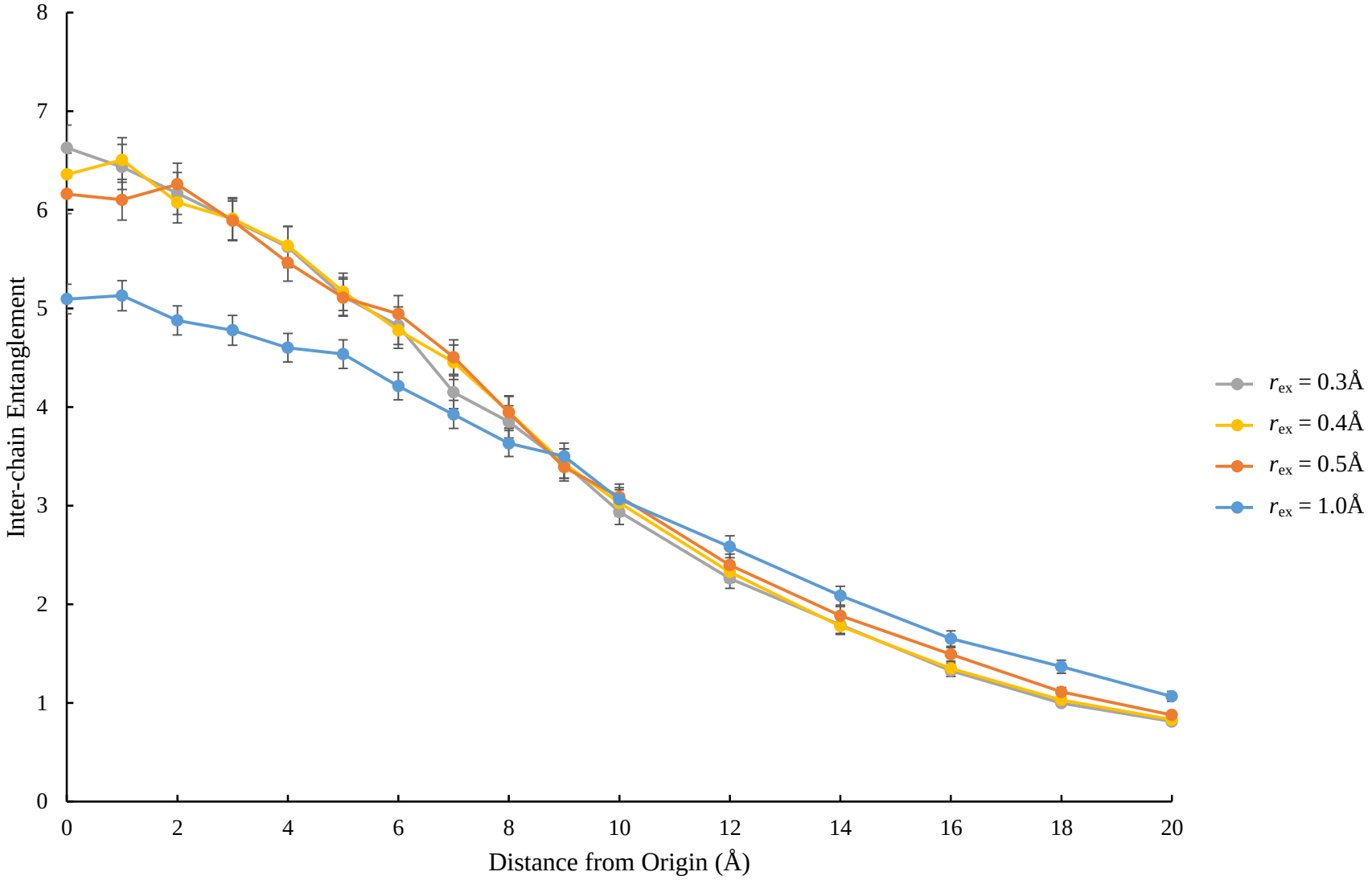

Figure 26: Effect of r_{ex} on inter-chain entanglement at n = 50 beads per chain and h = 15Å (model in Figure 13).

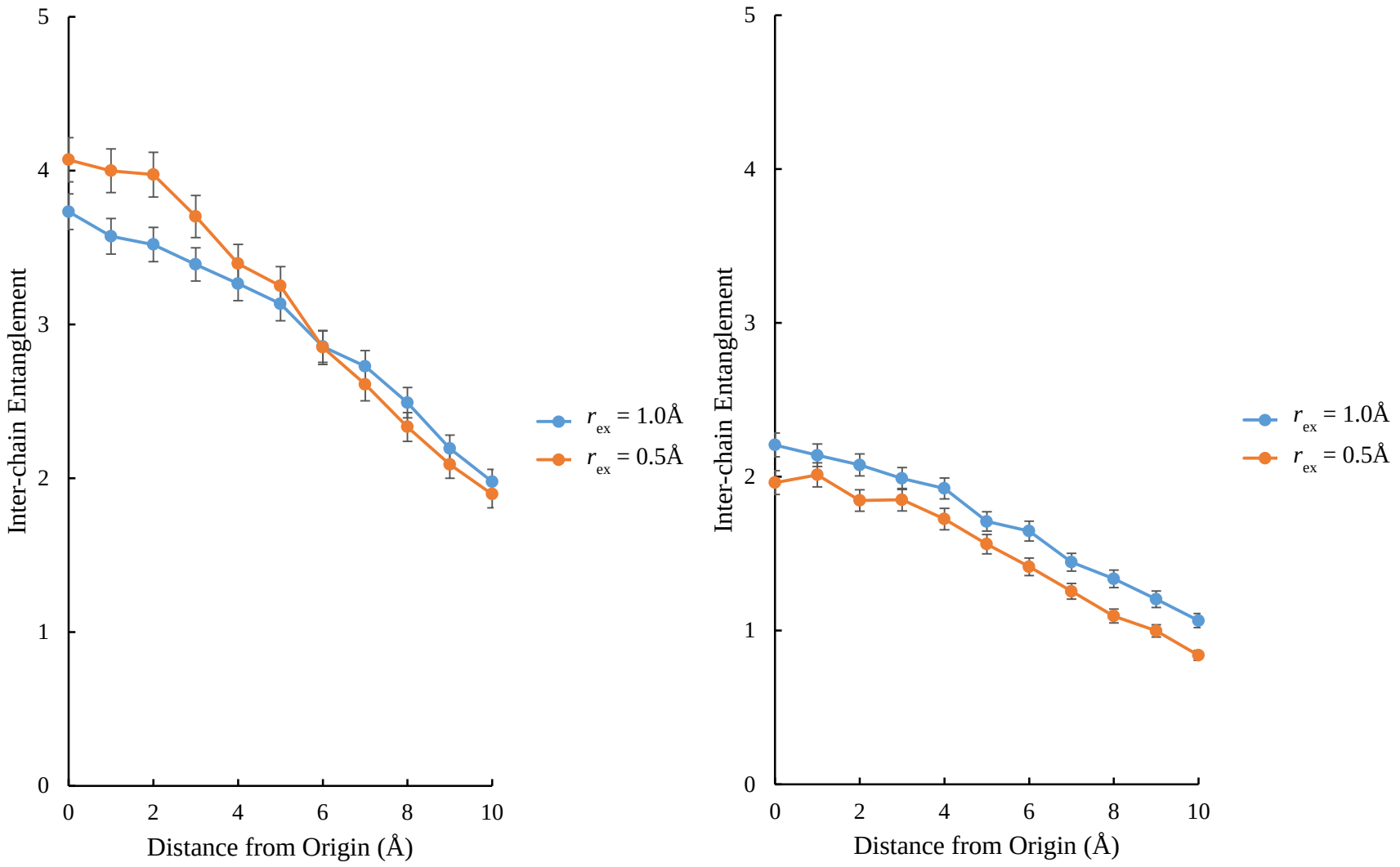

Figure 27: Shear displacement trends at different chain lengths, *n*, on inter-chain entanglement at *h* = 15Å, for, *n* = 40 [left], *n* = 30 [right], (model in Figure 13). Note that the crossover effect for inter-chain entanglement disappears, for a given compression value, if the chains are sufficiently short.

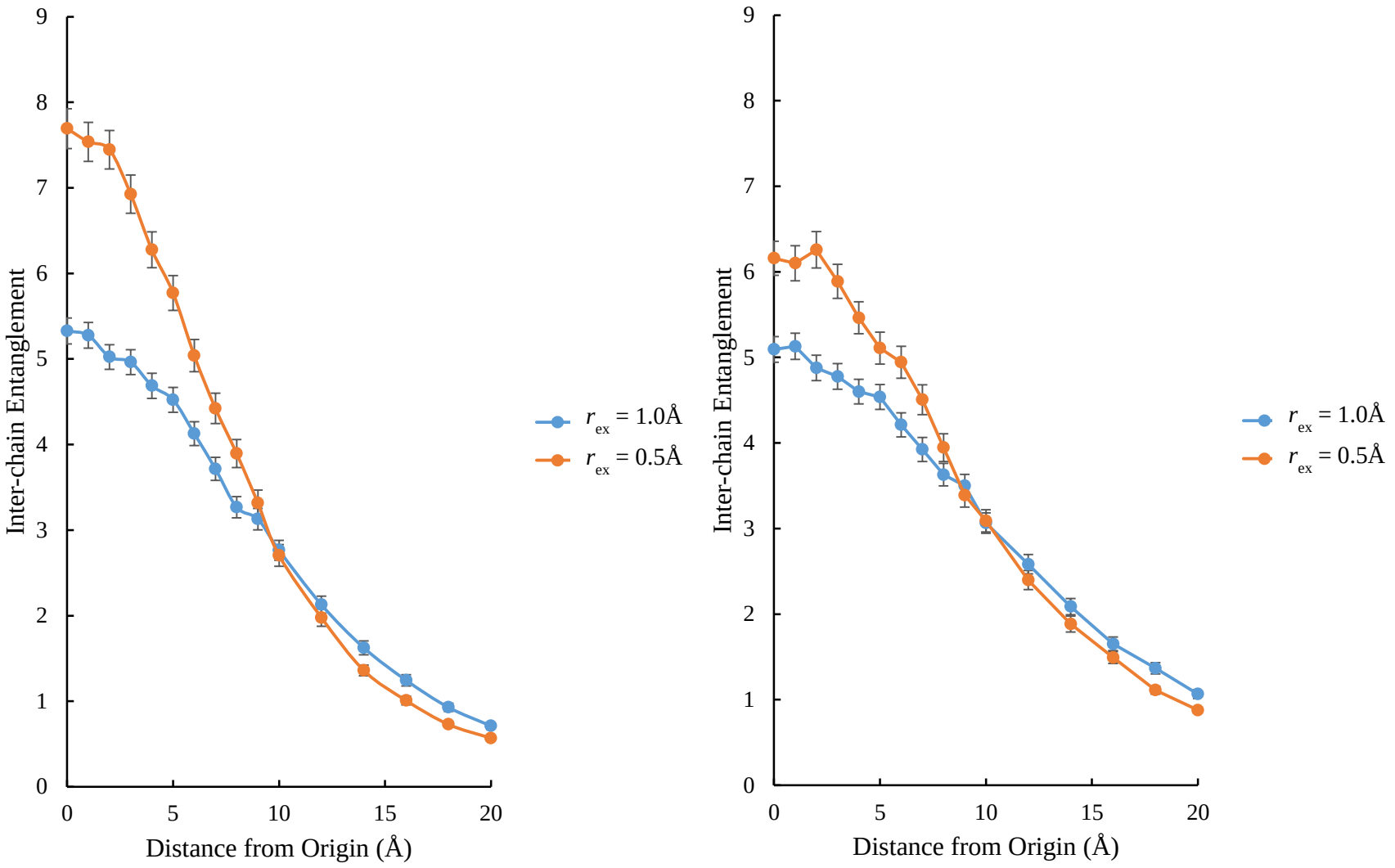

Figure 28: Comparing the effect of shearing of shorter chains at higher compression, *n* = 40 at *h* = 10Å [left], to longer chains at smaller compression, *n* = 50 at *h* = 15Å [right] on inter-chain entanglement (model in Figure 13). Note that short and long chains have approximately the same entanglement behaviour with their neighbour if the compression level is adjusted properly.

3.3. Two Chains with Different Length and Excluded Volume Under Compression

In this section, we present the results for the compression of two distinct chains, *i.e.*, two polymer mushrooms grafted on opposite surfaces, and differing in chain length and excluded volume interaction (model in **Figure 14**). For the sake of simplicity, we will indicate a model used in this context as [n_1 + n_2], where n_1 represents the length of the bottom-grafted chain and n_2 the corresponding length for the top polymer. Similarly, the model will be denoted by [r_{ex} + r_{ex}'], where r_{ex} and r_{ex}' are the (possibly different) radii of excluded volume for the bottom and top chains, respectively.

In order to get insight into the interplay of polymer lengths, **Figure 29** compares the models [50+20], [20+20], and [30+30], all with the same r_{ex} values. At h =15Å, both the [30+30] and [20+20] models exhibit an increase in inter-chain entanglement as the r_{ex} increases due to chain swelling. By switching one 20-bead chain for a longer 50-bead chain, the inter-chain entanglement in the [50+20] case is much larger over the entire range of r_{ex} compared to the identical [20+20] chain case. At smaller r_{ex} (less swollen chains), the [50+20] chains entangle more than the [30+30] chains until r_{ex} = 0.8Å, after which the inter-chain entanglement is comparable between the two. Finally, the trend of increasing inter-chain entanglement as r_{ex} increases is not observed for the [50+20] chains, and instead produces a steady level of relative entanglement. Clearly, the trends in entanglement as chains swell are much more nuanced if the chains have different length. This is consistent with the observation in section **3.2** that chains can sustain a small measure of entanglement at high excluded volume and compression *if* they are sufficiently long to reach each other.

Similarly, **Figure 30** compares the [30+30], [40+40], and [50+30] at h = 15Å, all chains having the same r_{ex} values. When one of the 30-bead chains was replaced with the longer 50-bead chain, the inter-chain entanglement increased significantly compared to the [30+30] case. Unlike the previous figure, the [50+30] system have fewer entanglements than the [40+40] case over the entire ranger of $r_{ex,}$ compared to [50+20] and [30+30]. The longer 50-bead chain had a less dramatic effect on inter-chain entanglements when the other chain was longer (30 beads rather than 20). As mentioned earlier, the [30+30] chains increased in entanglement with increasing r_{ex} while [40+40] chain entanglements plateau, due to the onset of larger chain avoidance (or steric effect) under compression. The inter-chain entanglement for the [50+30] pair is approximately

constant as a function of r_{ex} up to r_{ex} ~ 0.6Å, and then it decreases for r_{ex} > 0.6Å as the chains swell further.

Finally, **Figure 31** compares the systems [40+40], [50+40], and [50+50], where all the chains are computed with the same r_{ex} values, and the high compression value of h = 15Å. As mentioned previously in section **3.1**, the [50+50] system shows a decrease in inter-chain entanglements as the chains swell (increase in r_{ex}) due to chain avoidance, while [40+40] chains exhibit a nearly constant $\langle \overline{N}_{inter} \rangle$ value. When one of the 40-bead chains is replaced with a longer 50-bead chain, the inter-chain entanglement is roughly halfway between the values for the identical chain cases [50+50] and [40+40]. Unlike the trend seen for [40+40], the [50+40] chains distinctly decrease in entanglement as the chains swell, like the longer-chain case [50+50].

Finally, **Figure 32** deals with the n_1 = 50 and n_2 = 30 case, focusing on the effects of the different r_{ex} on inter-chain entanglement. This system represents a first rough approximation for the case of two repulsive polymers with different chemical compositions. For example, the low r_{ex} case can represent polyethylene (with each bead being methylene, -CH_2-) whereas the larger r_{ex}' case can be thought as representing polypropylene (with each bead taking the role of methyl methylene, -$CH(CH_3)$-).

When both chains have small r_{ex} values, we observe a smaller inter-chain entanglement since in this case each chain is rather compact and thus interacts minimally with the other. Likewise, when both chains have larger r_{ex} values, they swell and twist away from one another, resulting thus in fewer inter-chain entanglements. When one chain has a large r_{ex} value (whether it is the 30 or 50 bead chain) and the other has a smaller r_{ex} value, more inter-chain entanglements are possible as the swollen chain overlaps with the more compact chain. When the two chains have different mid-range r_{ex} values, the trend becomes quite complicated. As the **Figure 32** shows, within the statistical noise, there is a range of [r_{ex} + r_{ex}']-models that produce essentially the same level of inter-chain entanglement.

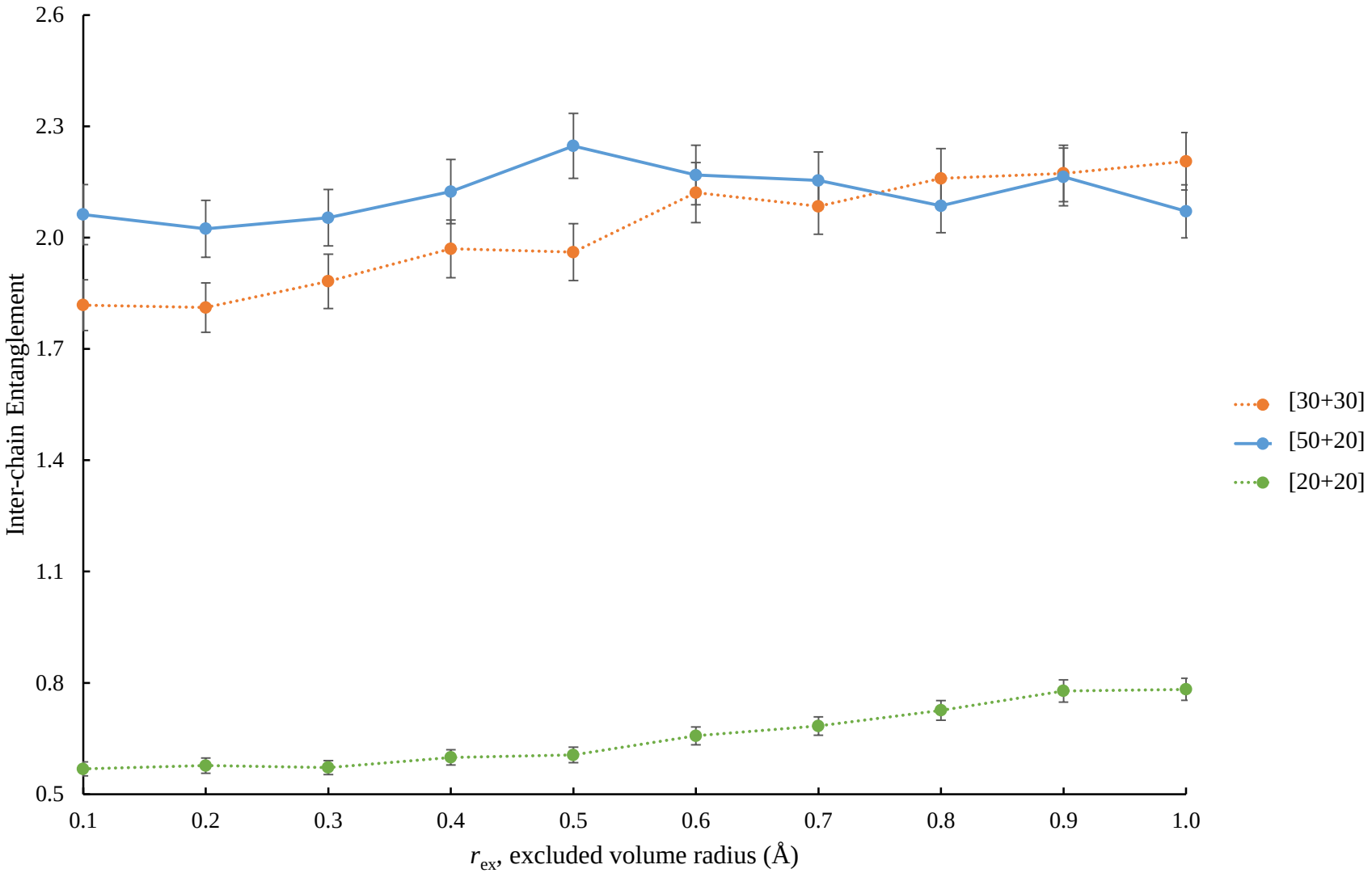

Figure 29: Comparison of two chains with different length and excluded volume lengths, n_1 = 50 and n_2 = 20 beads, with the same r_{ex} on inter-chain entanglement at h = 15Å. The notation [30+30] and [20+20] refers to two systems, one with to n_1 = 30 and n_2 = 30, and the other with n_1 = 20 and n_2 = 20, respectively, where n_1 refers to the bottom chain and n_2 to the top chain (model in Figure 14).

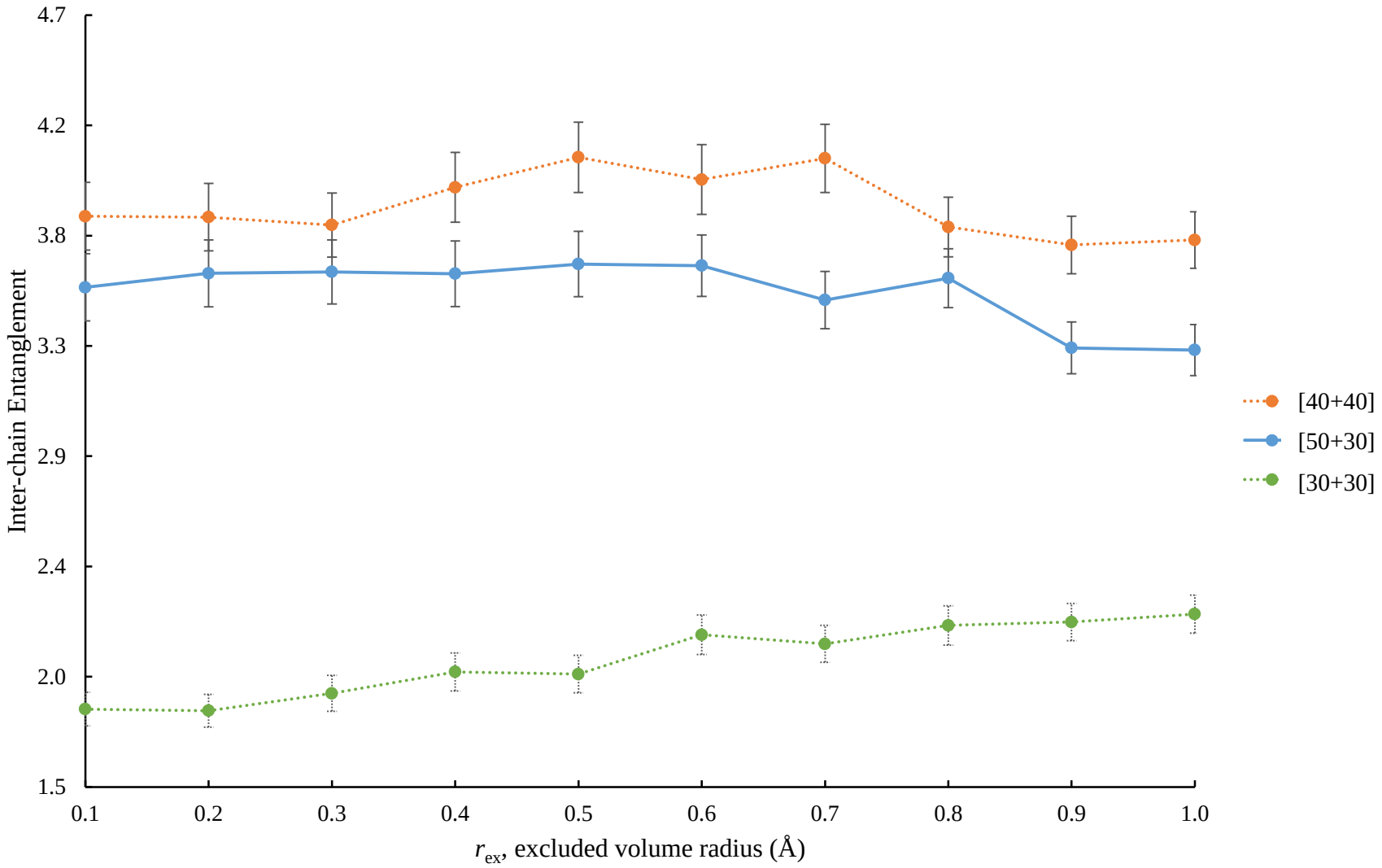

Figure 30: Comparison of two different chain lengths, n_1 = 50 and n_2 = 30 beads, with the same r_{ex} on inter-chain entanglement at h = 15Å. Note that [40+40] and [30+30] refers to two systems, one with n_1 = 40 and n_2 = 40, and the other n_1 = 30 and n_2 = 30, respectively, where n_1 refers to the bottom chain and n_2 to the top chain (model in Figure 14).

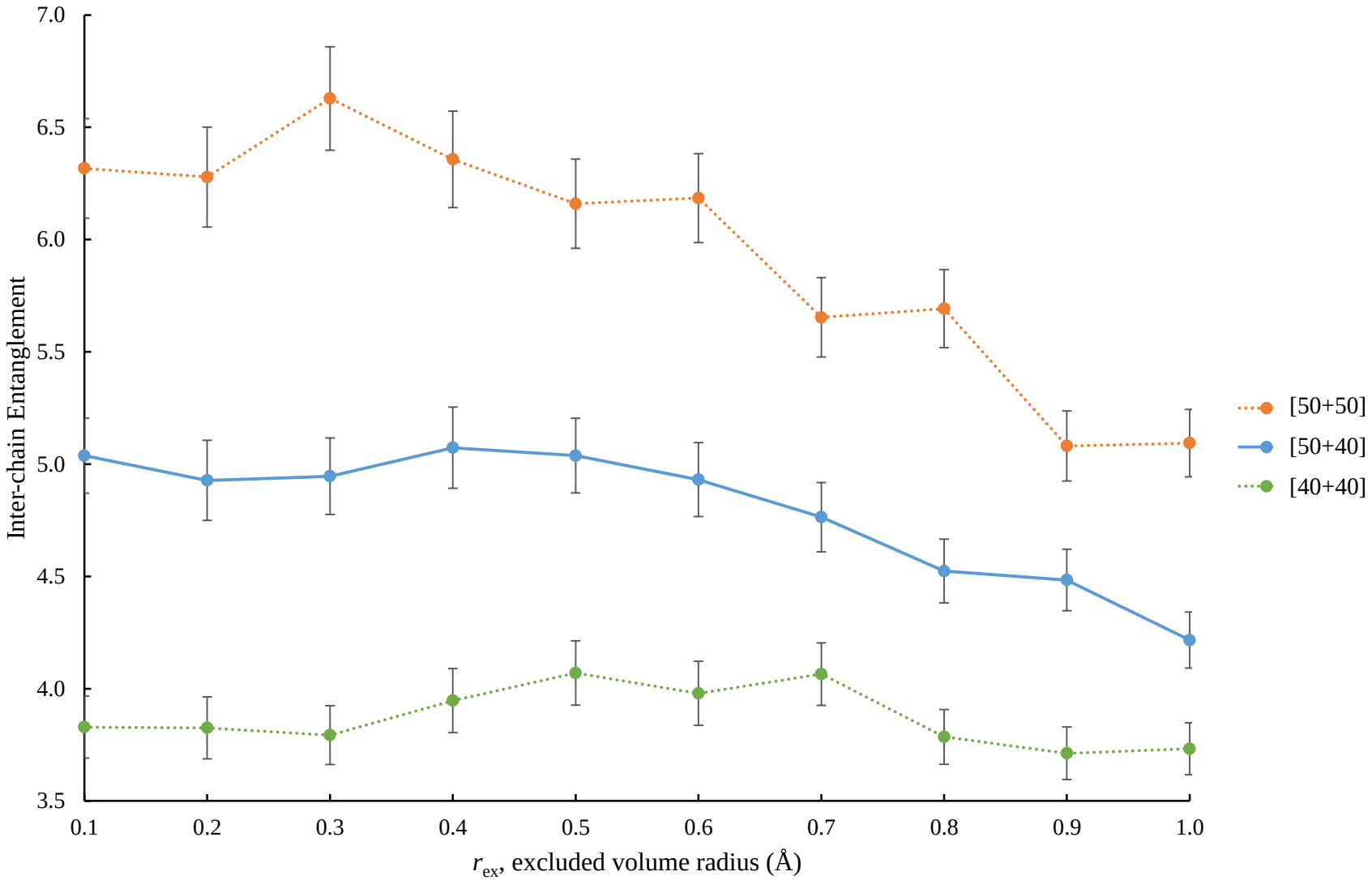

Figure 31: Comparison of two different chain lengths, n_1 = 50 and n_2 = 40 beads, with the same r_{ex} on inter-chain entanglement at h = 15Å. Note that [50+50] and [40+40] refers to two systems, one with n_1 = 50 and n_2 = 50, and the other n_1 = 40 and n_2 = 40, respectively, where n_1 refers to the bottom chain and n_2 to the top chain (model in Figure 14).

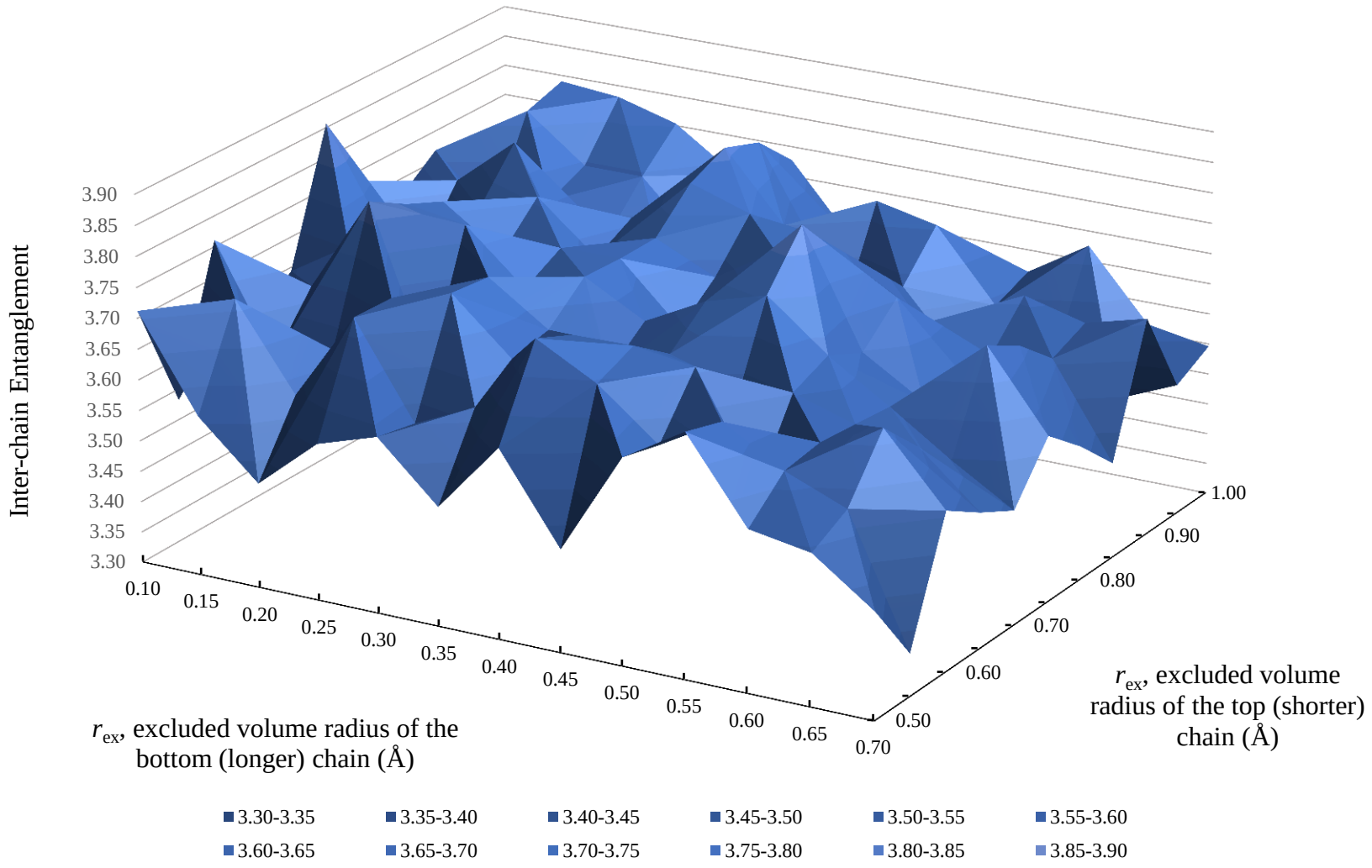

Figure 32: Comparison of two different chain lengths, $n_1 = 50$ and $n_2 = 30$ beads, with different r_{ex} on inter-chain entanglement at $h = 15$Å. The results are rather inconclusive, given the large statistical noise and configurational fluctuations. However, it is clear that there is a range of chain lengths and excluded volumes where two chains with different length and excluded volume can produce equivalent levels of inter-chain entanglement.

3.4. Three Chains Under Compression

In this section, we show the results of mean molecular shape in the case of three identical 50 bead chains under compression at h = 15Å and different packing geometries, as depicted in the models of **Figure 15** and **16**. In addition to studying the effects of crowding by neighbours, we also investigated the trend when symmetry is broken by shifting the location of the anchor bead for the grafted bottom chain.

In **Figure 33**, we compare the radius of gyration (shown in the left) and the intra-chain entanglement (shown on the right) of the three chains in the "linear geometry" arrangement (see **Figure 15** for the rigorous definition). The results show the effect of displacing the bottom chain anchor from D = 6Å to D = 0Å where it rests at the origin (and immediate below bead 1 of the top chains). Note that the anchoring position of the top chains does not change and the distance between their anchors is fixed at D' = 3Å, (see **Figure 15**). First, we observe that as the chains swell, increasing in r_{ex}, the radius of gyration increases accordingly for the chains, while the intra-chain entanglement decreases, consistently with the results seen in sections **3.1**, **3.2**, and **3.3**. On the other hand, we observed that shear displacements have minimal effect on intramolecular structure of each chain, similarly to the simulations performed in section **3.2**. In other words, shifting the bottom chain does not affect the individual shapes under compression, thus suggesting that only their relative positions are affected, possibly via chain avoidance (as if the chains would rigidly rotate away from each other).

Figure 34 shows the results for the "triangular geometry" arrangement of three 50-bead chains under compression at h = 15Å for the radius of gyration (shown in the left) and intra-chain entanglement (shown on the right). The symmetry is broken starting at D = 6Å, an isosceles triangle, and moving to D = 0Å, where we have the bottom chain anchor in the *middle* of the top chains when viewed in a projection perpendicular to the grafting planes (*i.e.*, a "linear geometry"). As in **Figure 33**, the chains swell and distangle when r_{ex} increases; the radius of gyration increases while intra-chain entanglement decreases. Likewise, the shear displacements had minimal effect on intramolecular structure of the chains, producing no distinct trend in either radius of gyration or intra-chain entanglement. The values and trends for radius of gyration and intra-chain entanglement are very similar for the two geometries.

Figure 35 contrasts the properties in **Figure 34** with the inter-chain entanglement between the fixed top chains (1 *and* 2) while the r_{ex} increase and the bottom chains (3) is moved,

i.e., $\langle \overline{N}_{inter} \rangle_{1,2}$ (eq. 2.12). (Note that these results are *only* for the way the two top chains entangle with each other, in the presence of the third chain at the bottom, but not with it). The results for the "linear geometry" are shown on the left and the "triangular geometry" is on the right. For both geometries, we see that as chains swell, the inter-chain entanglement between the two top chains (1 and 2) decreases. Since the anchoring position of the top chains is fixed at $D' = 3$Å, we see that inter-chain (1,2)-entanglement is unaffected by shear displacement. The difference in inter-chain entanglement between the two geometries is negligible. This suggests that either the chain (3) at the bottom moves away from the ones at the top, or that there is sufficient space at this level of compression to accommodate the bottom chain in the space between the two top chains.

Figure 36 contrasts the previous results with the inter-chain entanglement $\langle \overline{N}_{inter} \rangle_{1,3}$ between chains 1 and 3 (see eq. 2.12), for both geometries, as r_{ex} increases and chain (3) moves from $D = 6$Å to $D = 0$Å. Note the $\langle \overline{N}_{inter} \rangle_{1,3}$ is relatively constant for $D < 2$Å, then it decreases as chain (3) moves farther away from chain (1). At $r_{ex} = 0.5$Å, the inter-chain entanglement for both geometries are slightly smaller than that for the less swollen chains ($r_{ex} < 0.5$Å), which are all roughly comparable in value. Examining the linear geometry at $D = 0$Å ($r_{ex} = 0.5$Å), chain (3) is directly underneath chain (1) and, as a result, the inter-chain entanglement is slightly lower than when the chain is moved slightly away (*e.g.*, $D = 1$Å). Comparing the triangular geometry at $D = 0$Å ($r_{ex} = 0.5$Å), chain (3) is approximately 1.5Å away from chain (1) and consequently produces the largest value of inter-chain entanglement at that r_{ex} (see details of the geometries in section **2.3.1**). **Table 1** lists values of inter-chain entanglement for chains 1 and 2 ($\langle \overline{N}_{inter} \rangle_{1,2}$) as well as chains 1 and 3 ($\langle \overline{N}_{inter} \rangle_{1,3}$) with their respective standard deviations for both geometries. It is clear that the anchor position had no significant impact on inter-chain entanglement of three chains. As noted before, there seems to be enough space in these configurations to allow chains to accommodate by rotation and/or avoiding their neighbour. The result is such that, within the immediate neighbourhood, the actual location of the repulsive bottom chain plays little role on the relative entanglements.

Figure 37 summarizes our findings in this section by showing the inter-chain entanglement of chains (2 and 3) for the linear geometry as r_{ex} increases and chain (3) is moved. In the triangular geometry chains, symmetry implies that $\langle \overline{N}_{inter} \rangle_{1,3} \cong \langle \overline{N}_{inter} \rangle_{2,3}$. However, the linear geometry produces non-trivial results for the $\langle \overline{N}_{inter} \rangle_{2,3}$ inter-chain entanglement. At

D = 0Å and 6Å, chain (3) is 3Å away from chain (2), while at D = 3Å chain (3) lies directly underneath chain (2). When the chains are more compact (smaller r_{ex}) chains (2 and 3) interact more at D = 3Å. When the chains are more swollen (larger r_{ex}), they experience the largest inter-chain entanglement for 4Å < D < 5Å; at $D \leq$ 2Å there is added interactions from chain (1) and the inter-chain entanglement is significantly smaller. As noted in section **3.3**, there is a region of (D,r_{ex})-parameters that produce similar entanglement and equivalent configurations.

Table 1: Comparing inter-chain entanglements $\langle \bar{N}_{inter} \rangle_{1,2}$ and $\langle \bar{N}_{inter} \rangle_{1,3}$, when chain (3) is directly between chains (1 and 2), for the two geometries shown in Figure 15, (*i.e.*, "Linear" and "Triangular") displayed with the 95% confidence intervals.

	Inter-chain Entanglement			
r_{ex}, excluded volume radius (Å)	**Line (Chains 1,2)**	**Triangle (Chains 1,2)**	**Line (Chains 1,3)**	**Triangle (Chains 1,3)**
0.1	12.09±0.37	12.37±0.37	6.35±0.23	6.41±0.23
0.2	11.56±0.34	11.62±0.34	6.35±0.23	6.33±0.23
0.3	10.11±0.29	10.26±0.29	6.42±0.23	6.29±0.22
0.4	8.43±0.23	8.55±0.23	6.27±0.21	6.19±0.22
0.5	6.90±0.17	7.01±0.18	6.10±0.21	6.07+0.21

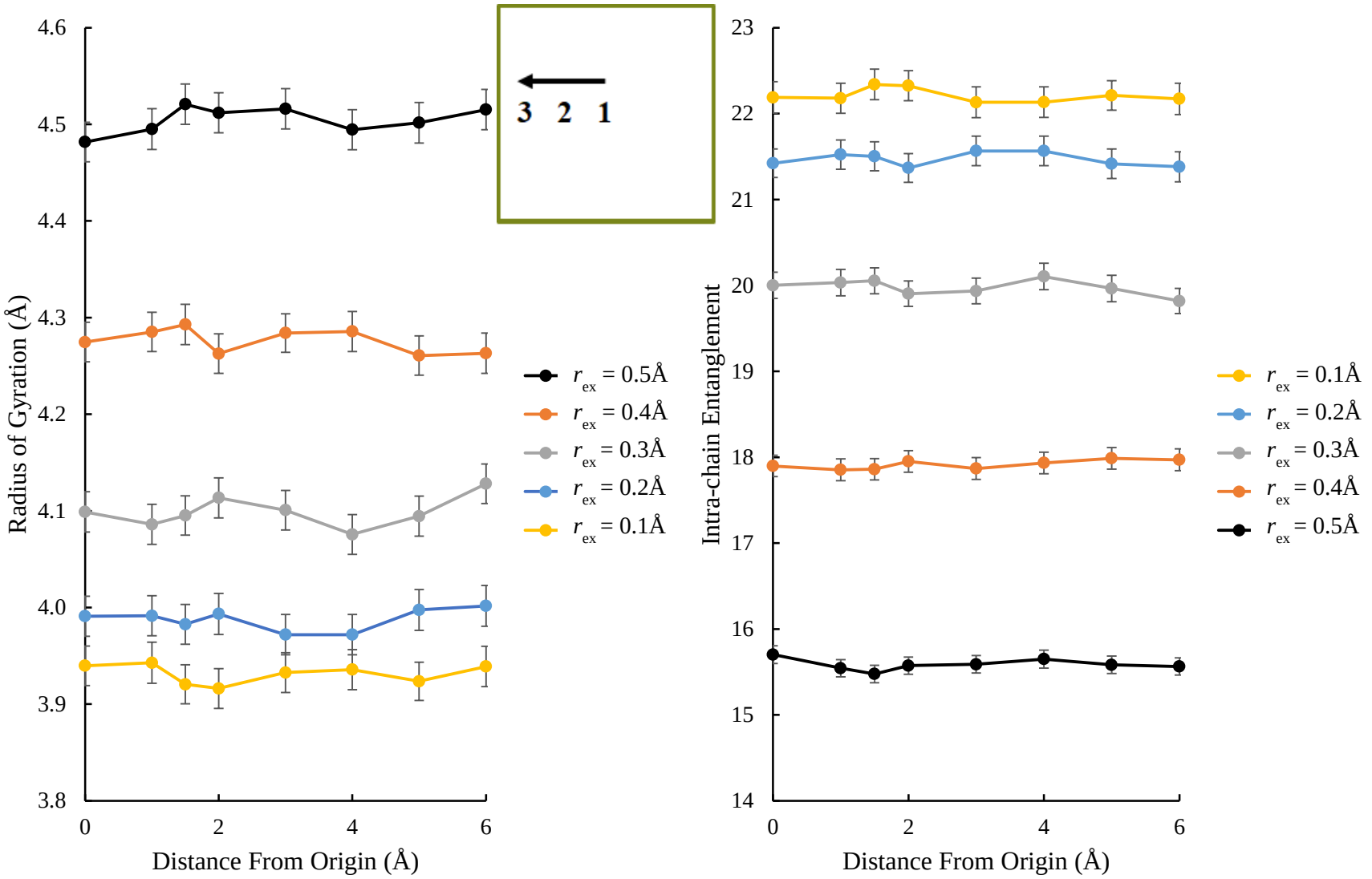

Figure 33: Individual chain shape properties for three chains (n = 50 beads) under compression (h = 15Å) in linear geometry (see insert), [on the left] radius of gyration, [on the right] intra-chain entanglement. D' = 3Å. (model in Figure 15). Recall, $O_{3,Bottom}$ = (0,D,0), $O_{1,Top}$ = (0,0,h), and $O_{2,Top}$ = (0,D',h), where D is varied.

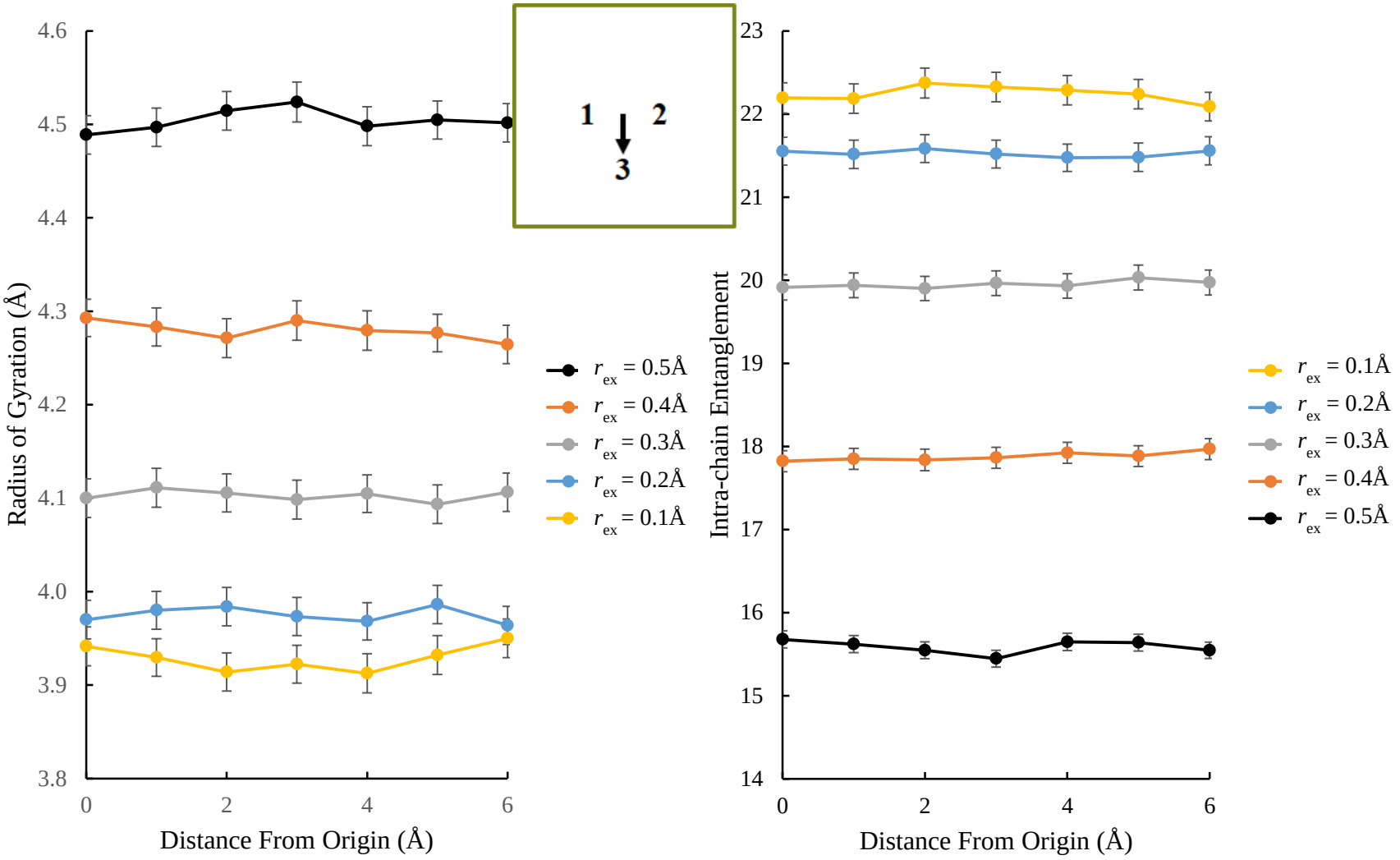

Figure 34: Individual chain shape properties for three chains (n = 50 beads) under compression (h = 15Å) in triangular geometry (see insert), [on the left] radius of gyration, [on the right] intra-chain entanglement. D' = 3Å (model in Figure 15). Recall, $O_{3,Bottom}$ = (D,0,0), $O_{1,Top}$ = (0,-D'/2,h), and $O_{2,Top}$ = (0,+D'/2,h), where D is varied.

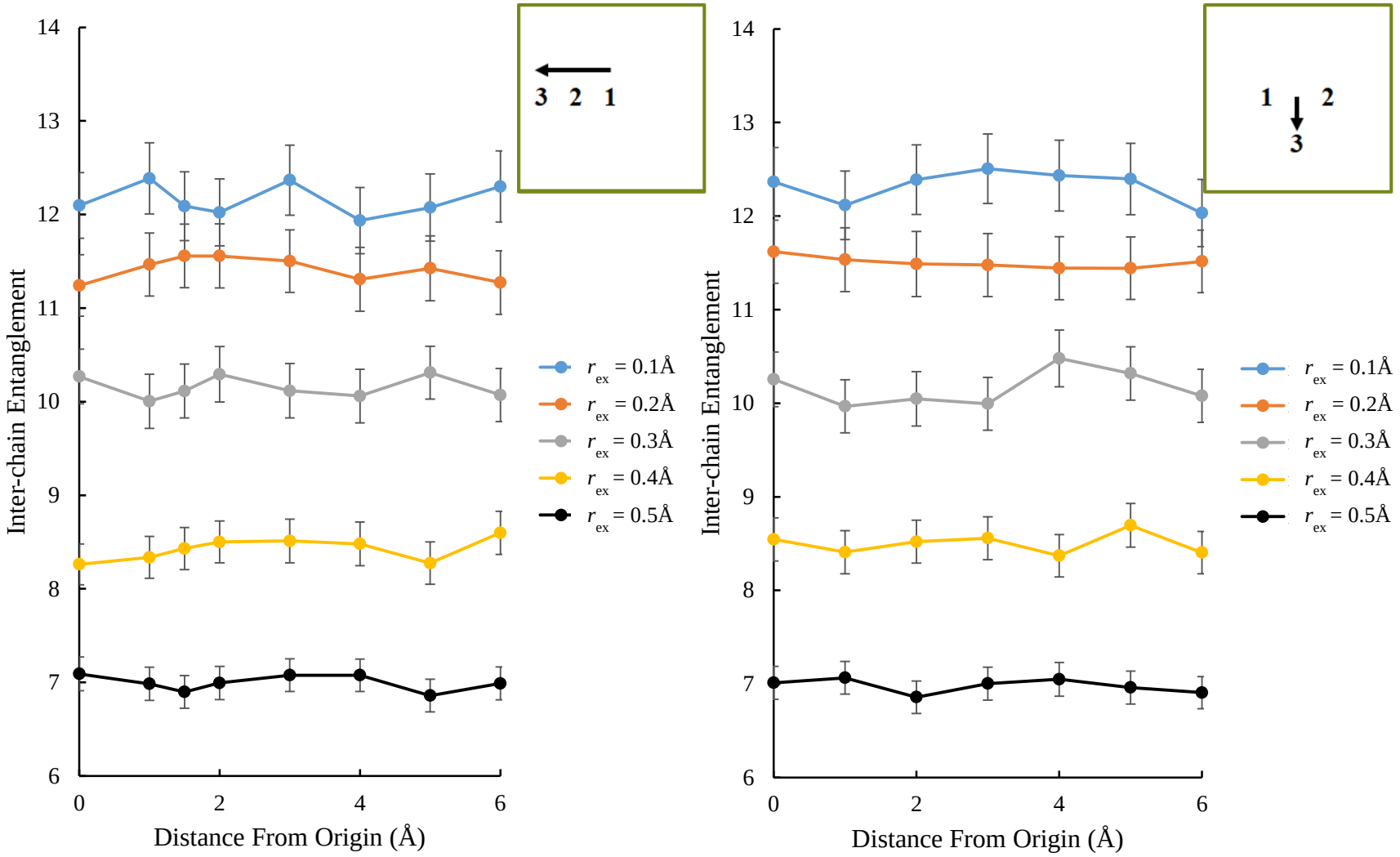

Figure 35: Inter-chain entanglement trends between chains 1 and 2 for three chains (n = 50 beads) under compression (h = 15Å), [on the left] linear geometry, [on the right] triangular geometry. D' = 3Å (model Figure 15). Recall: "Linear" is characterized by $O_{3,Bottom}$ = (0,D,0), $O_{1,Top}$ = (0,0,h), and $O_{2,Top}$ = (0,D',h); while "Triangular" corresponds to $O_{3,Bottom}$ = (D,0,0), $O_{1,Top}$ = (0,-D'/2,h), and $O_{2,Top}$ = (0,+D'/2,h), where D is varied.

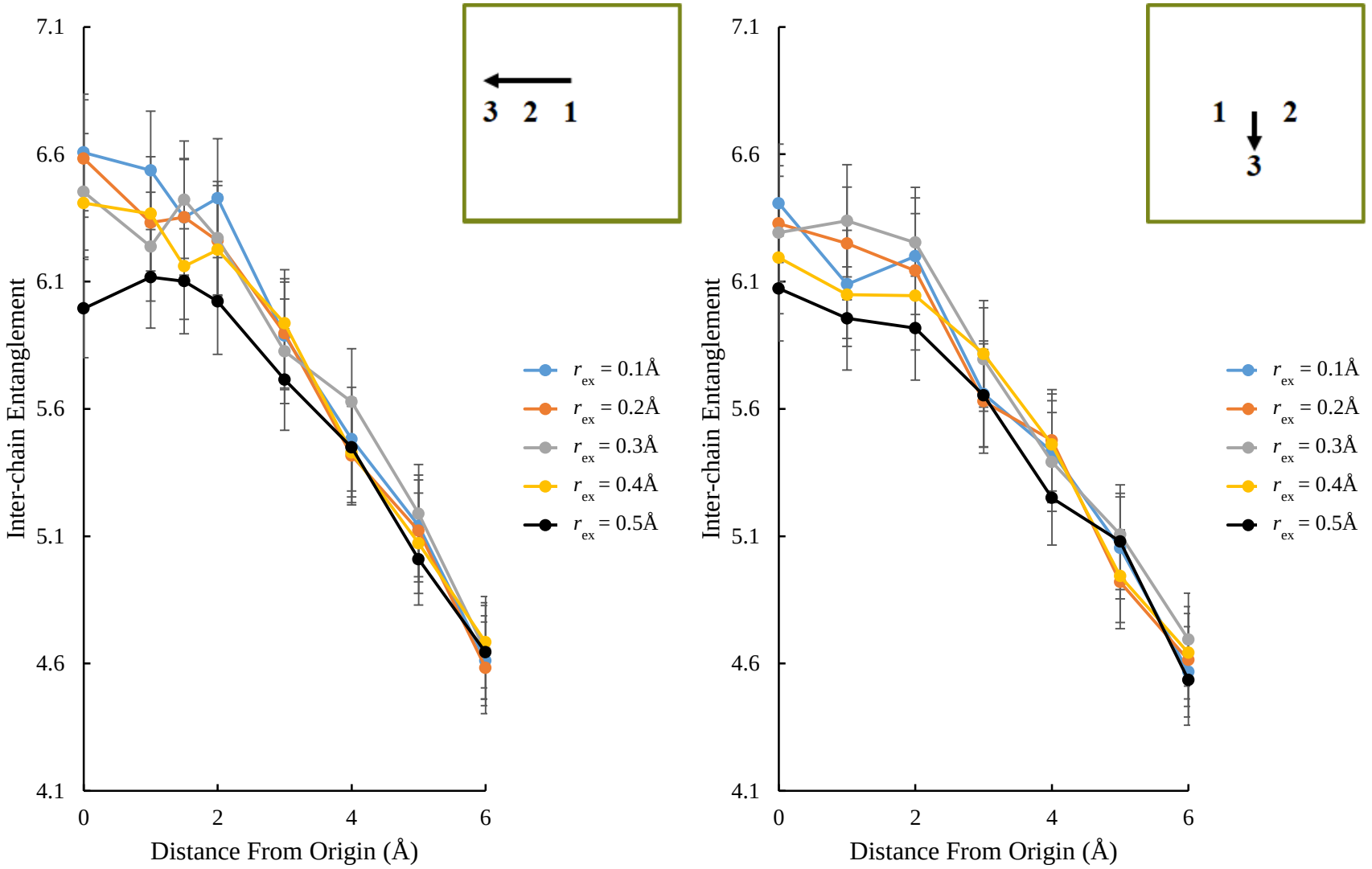

Figure 36: Inter-chain entanglement trends between chains 1 and 3 for three chains (*n* = 50 beads) under compression (*h* = 15Å), [on the left] linear geometry, [on the right] triangular geometry. *D´* = 3Å (model Figure 15). Recall: "Linear" is characterized by $O_{3,Bottom}$ = (0,*D*,0), $O_{1,Top}$ = (0,0,*h*), and $O_{2,Top}$ = (0,*D*',*h*); while "Triangular" corresponds to $O_{3,Bottom}$ = (*D*,0,0), $O_{1,Top}$ = (0,-*D*'/2,*h*), and $O_{2,Top}$ = (0,+*D*'/2,*h*), where *D* is varied.

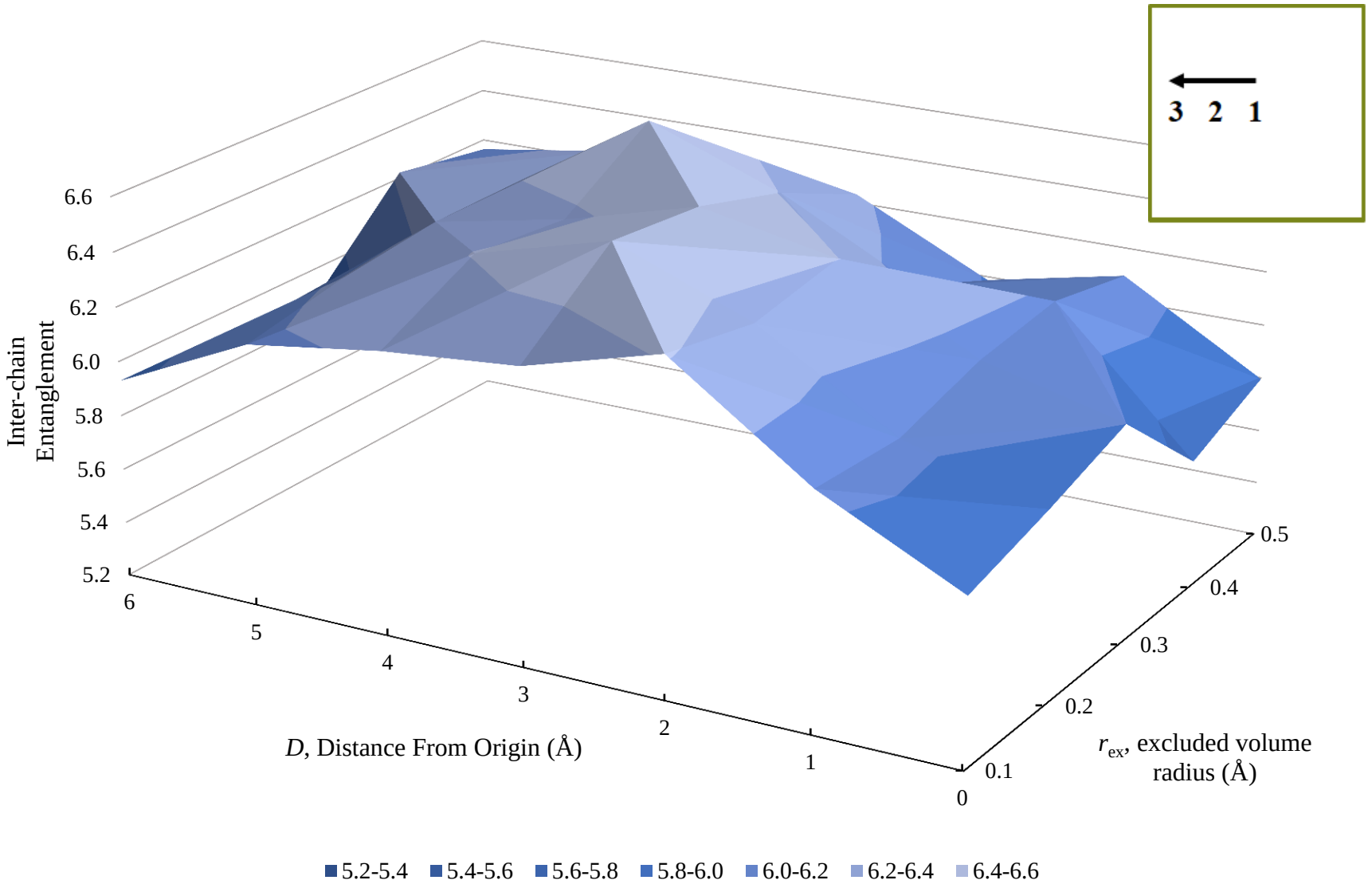

Figure 37: Inter-chain entanglement trend between chains 2 and 3 for three chains (n = 50 beads) under compression (h = 15Å) for linear geometry. D' = 3Å. Despite the statistical noise and configurational fluctuations, we can clearly observe a region of D and r_{ex} values that produce a maximum in $\langle \bar{N}_{inter} \rangle$.

3.5. Seven Chains Under Compression

In the final section of results, we considered seven chains in hexagonal packing, where chain 1 is grafted to the top plane and the remaining chains (chains 2-7) are grafted to the bottom plane (model in **Figure 17**). Each chain comprises of n = 20 beads per chain, and compressed at h = 15Å. We investigated the molecular structure and shape properties of this seven-chain system and compared the results to the work previously conducted by our laboratory ([Harrison, 2014], [Richer *et al*., 2017]), **Figure 38**. In this previous work, we studied seven identical polymer chains grafted to one surface, and examined how steric crowding by neighbours affected the structural and shape properties of the chains, as well as how the chains reoriented themselves when the symmetry of the grafted anchors was broken. This system will constitute the "uncompressed" state, to be used as a reference to compare the results generated from the model shown in **Figure 17**, where we bring chain 1 (top plane) into close proximity of the remaining six chains, while preserving the regular hexagonal coordination during compression.

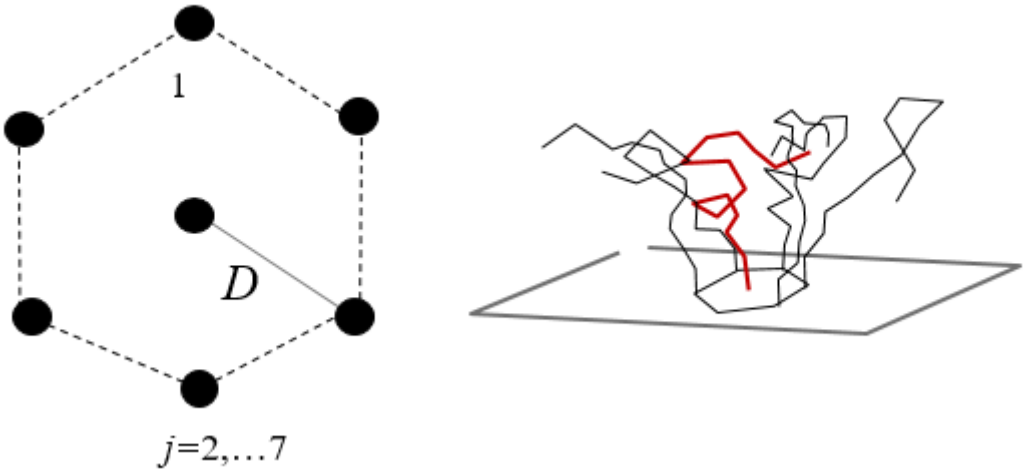

Figure 38: Schematic of the uncompressed seven polymer chain model. This model provides a reference to compare the results for the two-plane system in Figure 17. (The left-hand side diagram shows the anchor geometry on the bottom plane and the model variable *D*).

Figure 39, compares the mean radius of gyration of the seven chains when uncompressed (*i.e.*, seven chains on the same plane, as in **Figure 38**) and under compression (six chains on the bottom plane, one chain on the top plane, **Figure 17**). Note that the shape descriptors are averaged over the ensemble of seven chains. (This approach neglects the fact that the

coordinating chains have different symmetry, and possibly different mean size, than the central chain. However, our interest is to uncover the role of compression and excluded volume over the entire ensemble, not on a subgroup of chains. When addressing the differences between the central chain and the hexagonal neighbours, we use the inter-chain entanglement descriptor.)

Firstly, we observe that as r_{ex} increases so does the radius of gyration of both the compressed and uncompressed chains. When the chains are more compact, the value and approximate trend of radius of gyration is not drastically affected by compression. At larger r_{ex}, the two conditions have similar values of mean chain size, however the compressed chains produce slightly smaller sizes at closer packing. For the more swollen chains (r_{ex} = 0.4Å) at distances less than 6Å, the radius of gyration increases less for the compressed chains, indicating that, due to the repulsion of its close neighbours, the chains are forced to somewhat "collapse" onto themselves by the presence of the confining top plane.

Figure 40 complements the results for the R_g, by showing the change in asphericity (Ω) with the lateral crowding, with and without compression. The results are entirely consistent with those for size in **Figure 39**: prolate forms correlate with larger size, and compression has little role on the shapes, except in the case of a denser lateral packing (D < 5Å), which produces slightly more spheroidal chains under compression. This is likely due to chain avoidance at the higher confinement, which produces more compact, spherical chains under the constraints of the neighbours. This effect is more marked for chain 1 (the one grafted to the top plane), which gets fully confined inside the hexagon under compression.

Figure 41 indicates also that the same conclusions can be extracted in terms of intra-chain entanglements for a given r_{ex}, compression does not affect $\langle \overline{N}_{intra} \rangle$-values: we only observe a decrease for the more swollen chain at D < 6Å, as a result of tighter coordination or larger density of neighbours.

The more insightful observations, however, appear in **Figure 42**, which deals with the inter-chain entanglement of seven chains as r_{ex} increases and the outer chains are moved away from the central chain located either on the top or bottom plane. The inter-chain entanglement trend is drastically different between the compressed (**Figure 17**) and uncompressed conditions (**Figure 38**). Firstly, the number of inter-chain entanglements is significantly lower when the chains are compressed, compared to the uncompressed chains. For the uncompressed chains, inter-chain entanglement decreases when their neighbours are moved away (D-increases); as

expected, the $\langle \overline{N}_{inter} \rangle_{i,j}$ average over all (*i*,*j*)-chain pairs is smaller for more swollen chains (r_{ex} = 0.4Å).

When the chains are compressed, however, a key difference emerges. As in the case of no compression, $\langle \overline{N}_{inter} \rangle_{i,j}$ decreases with *D*, and we see:

$$[\langle \overline{N}_{inter} \rangle_{i,j}(r_{ex})]_{\text{compressed}} < [\langle \overline{N}_{inter} \rangle_{i,j}(r_{ex})]_{\text{noncompressed}} \quad (3.1)$$

due to steric effects and chain avoidance. However, the results in **Figure 42** indicate a reversal in behaviour: for a given *D*-value, the more swollen chains entangle *less* with their neighbours under no compression, but entangle *more* in presence of compression.

The results in **Figures 39**-**41** indicate that the intrinsic chain shapes are not affected by compression, while **Figure 42** shows that their interrelation is affected. A simple explanation for this behaviour finally confirms the emerging picture of chain avoidance: with no compression, the chains are nearly vertical and thus do not entangle between themselves (*i.e.*, they are nearly parallel). As compression sets, chains keep their shapes but are forced to rotate away from the approaching surface and top chain. As a result, the bottom interpenetrates more. This leads to an increase in $\langle \overline{N}_{inter} \rangle_{i,j}$, and the effect increases as chains swell. In no case we see evidence of escape transitions with coil-and-flower configurations, as it was in the case of hexagonally coordinated uncompressed chains. We expect that these "anomalous" configurations will only appear under compression if they have sufficiently high number of neighbouring chains and a non-symmetric arrangement. A small number of chains ($n \leq 3$) or a regular hexagonal arrangement do not produce escape transitions, but rather lead to chains avoidance with "regular" configurations (*i.e.*, with uniform spatial distributions of monomer beads).

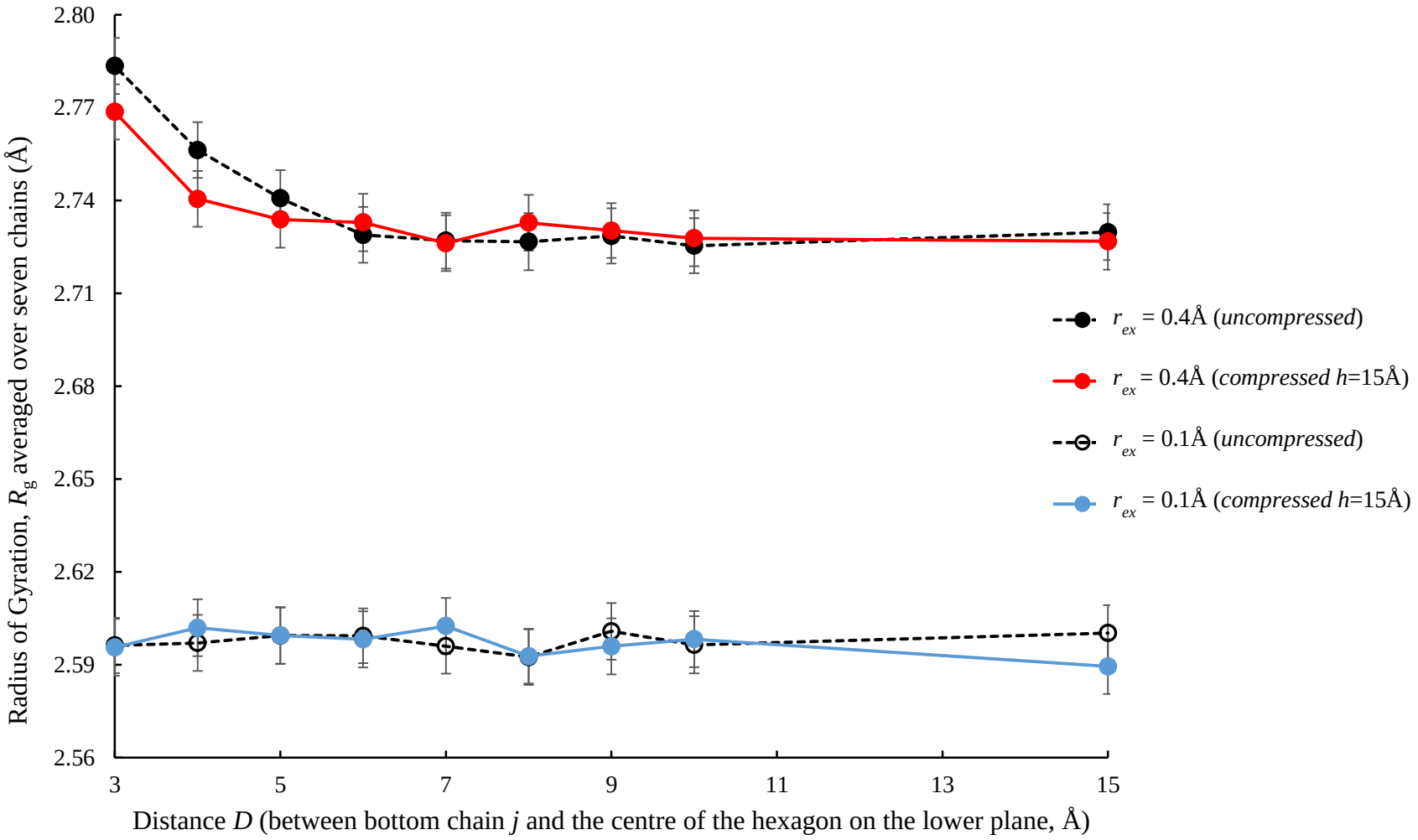

Figure 39: Average radius of gyration over seven chains, *n* = 20 beads per chain, uncompressed chains and chains compressed at *h* = 15Å. (Note that the "compressed" system corresponds to the model in Figure 17, while the "uncompressed" state corresponds to the system in Figure 38).

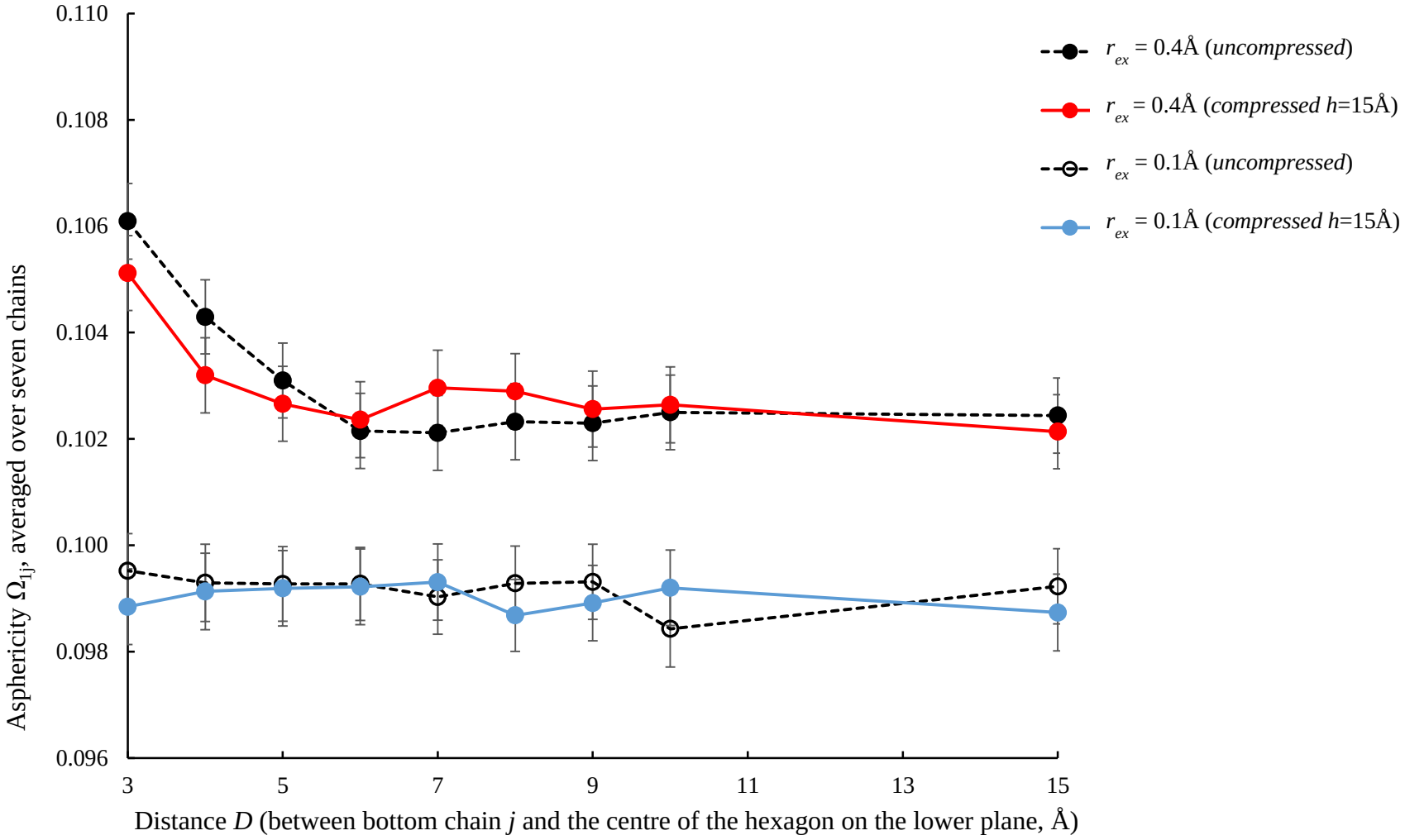

Figure 40: Average asphericity over seven chains, *n* = 20 beads per chain, uncompressed chains and chains compressed at *h* = 15Å. (Note that the "compressed" system corresponds to the model in Figure 17, while the "uncompressed" state corresponds to the system in Figure 38).

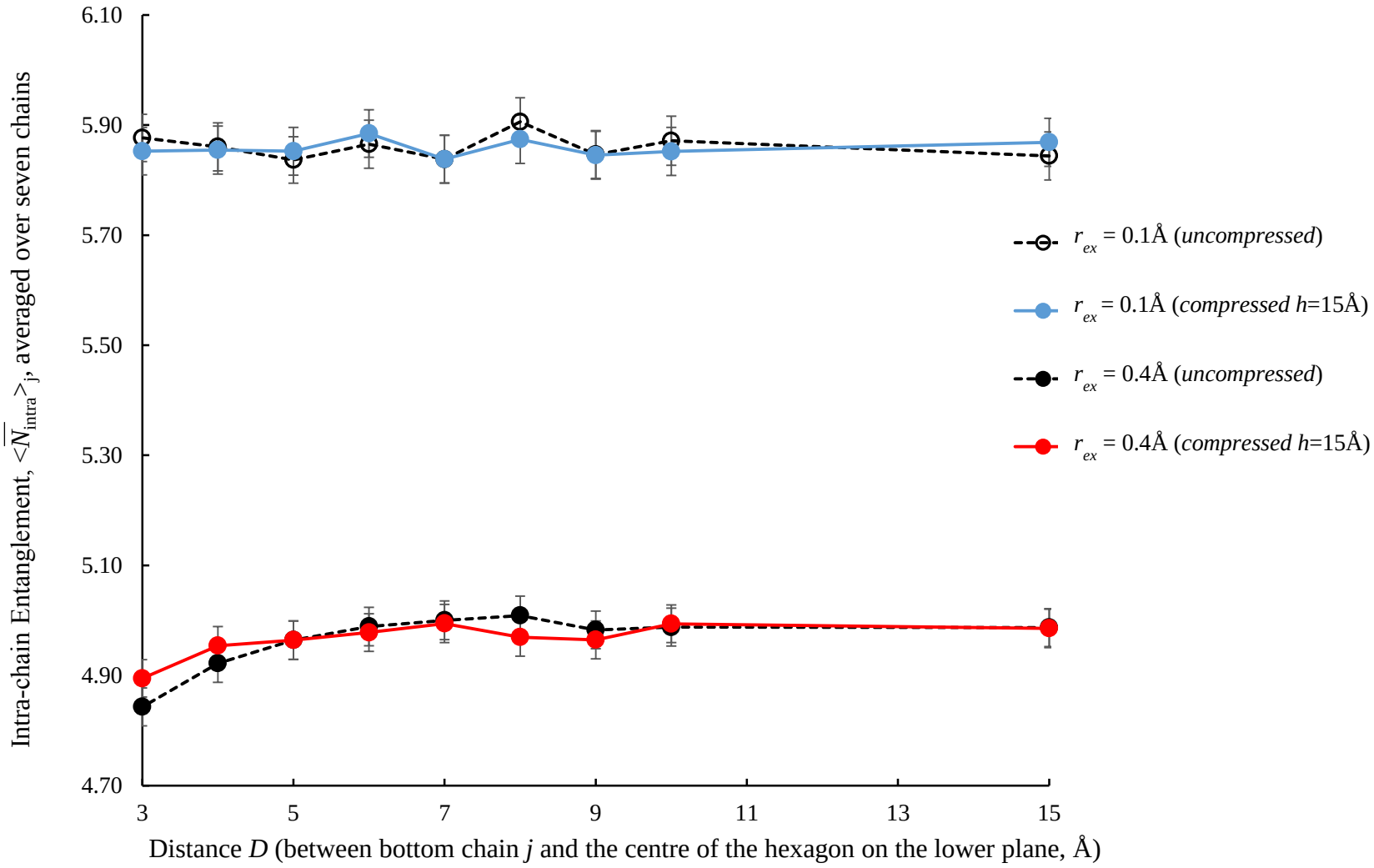

Figure 41: Average intra-chain entanglement over seven chains, *n* = 20 beads per chain, uncompressed chains and chains compressed at *h* = 15Å. (Note that the "compressed" system corresponds to the model in Figure 17, while the "uncompressed" state corresponds to the system in Figure 38).

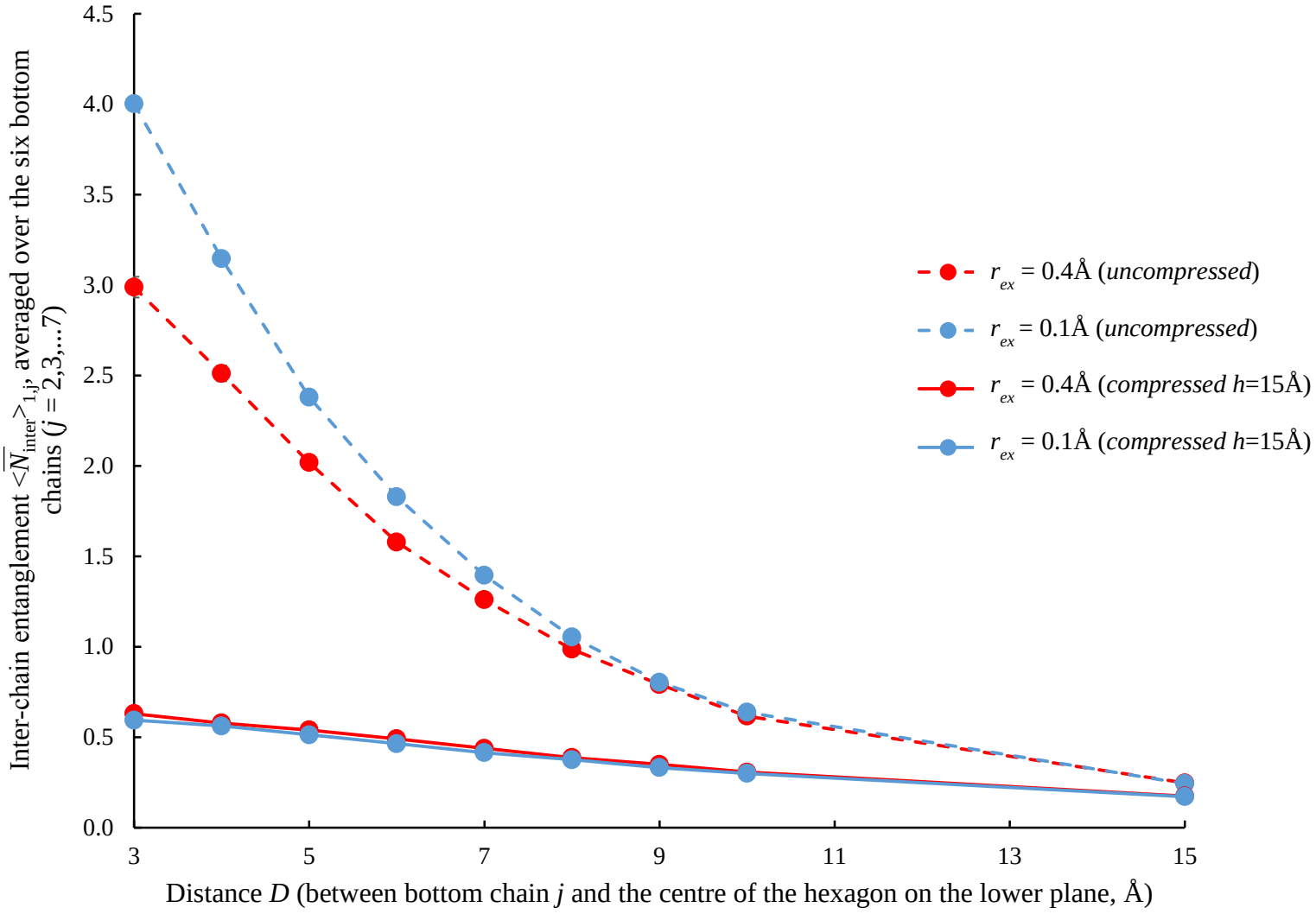

Figure 42: Average inter-chain entanglement over the six bottom chains with chain 1, *n* = 20 beads per chain, uncompressed chains and chains compressed at *h* = 15Å. (Note that the "compressed" system corresponds to the model in Figure 17, while the "uncompressed" state corresponds to the system in Figure 38).

Chapter 4

4. Summary of Observations and Further Discussion

Using the procedure outlined in section 2, we have generated trajectories for a range of low density polymer brushes and analyzed their structural and shape properties. The latter properties were characterized in terms of chain size, anisometry, and entanglement complexity. We have performed exploratory simulations for repulsive hard spheres with a variable plate separation height, chain length, excluded volume (r_{ex}), chain location, and finally the number and geometry of neighbouring chains. Recently [Richer *et al.*, 2017], we have shown that in the absence of compression, reorganizations in grafting geometry can lead to "escape transitions" [Arteca, 1997a] even in repulsive polymers, not caused by the presence of a finite size obstacle, but by the uneven coordination around a grafted chain. These "transitions" involve the formation of configurations with an uneven level of compactness in the chains, *i.e.*, with a swollen "tether". These configurations have the unusual characteristic of having *large size* (due to the tether or stem) and a *large intra-chain entanglement* (due to the "flower", *i.e.*, the compact moiety of an escaped polymer mushroom). Throughout this thesis, we observed a range of reorganizations triggered by the available space between chains, as well as the excluded volume repulsions, but in *no case* observed the formation of the "coil-to-flower" configurations typical of escape transitions. Our results indicate that compression in sparsely-covered polymer brushes modifies their entanglements, but by mechanisms different from escape transitions, *e.g.*, chain avoidance and rotation. Below we summarize our main findings.

4.1. Two Chains Under Compression

Figures 20 and **21** show the molecular shape descriptors of two chains located directly on top of one another, each 50-bead long at a plate separation height of 15Å. **Figure 20** compares how asphericity (Ω) and radius of gyration (R_g) increase with r_{ex}, while **Figure 21** compares how inter- and intra-chain entanglements decrease at dissimilar rates. As r_{ex} increases, the chains swell, becoming larger in mean size and more prolate in shape. Simultaneously, $\langle \overline{N}_{intra} \rangle$ decreases as chains unwind and become less self-entangled. These correlations between $\langle \overline{N}_{intra} \rangle$, R_g, and Ω descriptors are typical on "uniform" configurations, *i.e.*, those which are *not* found in escape transitions.

Whereas the individual chain shape (asphericity, radius of gyration and intra-chain entanglement) produce very clear and distinctive trends as the r_{ex} increases, the intermolecular shape is affected in a subtler way. **Figure 21** suggest that the inter-chain entanglement decreases slightly with increasing r_{ex} due to chain avoidance. As the chains swell, potential closeness (or "steric effects") forces them to twist and bend away from each other. Note that the individual chain shape properties (Ω, R_g, and $\langle \overline{N}_{intra} \rangle$) behave similarly over the entire range of chain lengths considered.

In **Figure 22**, we focus on inter-chain entanglement as r_{ex} increases, as a function of chain length and plate separation heights. At the larger plate separation (h = 30Å), inter-chain entanglement increases with swelling for all the chain lengths. This behaviour indicates that chains come into closer proximity and interpenetrate as they swell. Under weak compression, longer chains find sufficient space to stretch and reach each other thus resulting in larger inter-chain entanglement. At high compression, this is still the case for shorter chains (20 and 30 beads), where $\langle \overline{N}_{inter} \rangle$ increases with r_{ex} due to the chains proximity. However, the longest chains (50 beads) find themselves in the strong triple constraint of higher compression, large excluded volume, and chain length. Under these conditions, long chains do not find the space to swell into each other, and are thus forced to avoid each other, reducing the inter-chain entanglements. The case of 40-bead chains represents the intermediate situation to switch between these two behaviours. In other words, inter-chain entanglement is affected both by swelling and interpenetration but it is at the same time limited by the additional repulsions caused by an increasing chain length.

Figure 23 compares the inter-chain entanglement trends in 50-bead chains to illustrate the level of compression at which chain avoidance becomes the dominant behaviour. At the lowest compression (h = 50Å), there is no significant chain interaction and inter-chain entanglement (*i.e.*, chains cannot reach one another even when swollen). For h = 30Å to h = 20Å, the inter-chain entanglement increases, chains swell and interpenetrate. At h = 17.5Å, the inter-chain entanglement becomes essentially independent of r_{ex} in the same way as it did for the 40-bead chains at h = 15Å (**Figure 22).** At smaller plate separations (h < 17.5Å), chain avoidance becomes the dominant factor, and $\langle \overline{N}_{inter} \rangle$ *decreases* with r_{ex}.

Figure 24 gives us further insight into the proposed above mechanism for the onset of chain avoidance at critical values of compression and chain length. Using the 50-bead chain, we

observe that weak compression plays a little role on mean chain size, producing only a marginal increase, for a given r_{ex}-value. This small difference can be attributed to the fact that chains no longer avoid each other as they do at higher compression, h = 15Å. The effect of compression on intra-chain entanglement is even smaller than that for mean chain size. **Appendix 4, Figure 44**, complements these observations by showing the results for mean asphericity, Ω, for varying compression. For all the plate heights, we observe that chains become more prolate as r_{ex} increases. All these results are consistent with the trend that compression prevents chains from becoming fully elongated along the *z*-axis, and thus any lateral swelling must lead to lower inter-chain entanglement to lower repulsions.

4.2. Two Shifted Chains Under Compression

We gain further understanding on the interplay between entanglement and chain avoidance by studying shear displacement (**Figure 25**). The results show that, over a range of excluded volume interactions, mean chain size is unaffected by displacements. This is confirmed by the selected inserts generated from HyperChem, which illustrate that there are no drastic changes in the size of the individual chains, despite chain avoidance at closer distances (D = 4Å).

Appendix 5 supplements this information by showing the results for the mean radius of gyration during displacement for more swollen chains (r_{ex} = 0.3Å and 0.4Å), as well as the results for asphericity and intra-chain entanglement over a range of radii of excluded volume (**Figures 45-47**). The result support the previous observation: like the radius of gyration, both asphericity and intra-chain entanglement are unaffected by shear displacements. The asphericity, like the radius of gyration, increased in size as the chains swell and become more prolate (*i.e.* less spherical) in shape, while the intra-chain entanglement decreased with r_{ex} as the chains untangle. This behaviour is intrinsic of the chain, and determined by n, r_{ex}, and h, and not by D. We find no evidence of the formation of coil-and-flower configurations induced by a neighbour chain under compression.

Unlike the intramolecular shape descriptors, shear displacements affect the inter-chain entanglement. Whereas the number of overcrossings decreases for all r_{ex} values as the top chain is moved farther away from the origin, the rate of decay depends strongly on excluded volume. There exists a critical distance, approximately $D \cong 9$Å, where the more swollen chains become the ones with the largest inter-chain entanglement (**Figure 26)**. When the chains are grafted

closer together, the swollen chains repel each other, leading to chain avoidance. However, when the chains are farther apart, the chain swelling allows them to interact more which resulted in more entanglement between chains with respect to pairs of separated, less swollen chains.

In the regime of high compactness (h = 15Å), this crossover in inter-chain entanglement during displacement is maintained only over a range of polymer lengths. In **Figure 27** and **Figure 48** (**Appendix 5**) we examine the inter-chain entanglement trends of shorter chains. **Figure 27** compares the entanglement between n = 40 and n = 30 chains, while the supplementary **Figure 48** displays the trend of the shortest chains (n = 20 beads). The 40-bead chains are still long enough to present a crossover to larger $\langle \overline{N}_{inter} \rangle$-values at closer grafting distances ($D \approx$ 6Å, unlike the $D \approx$ 9Å for n = 50 beads). For shorter chains (n = 20 and 30), the less swollen chains (r_{ex} = 0.5Å) always entangled not as much as the more swollen chains (r_{ex} = 1.0Å) since the chains are too short for chain avoidance to be necessary. The crossover, if found at all, would take place at higher confinement (h < 15Å).

Figures 28 and **Figure 49** (**Appendix 5**) complete the analysis by showing the results for the behaviour of shorter chains at higher compression. **Figure 28** deals with 40-bead chains, while **Figure 49** the results for the 30-bead chains, both at h = 10Å. Earlier, we demonstrated that at less compression (h = 15Å), 30-bead chains were too short for chain avoidance to occur and, as a result, entangled more when swollen (r_{ex} = 1.0Å), regardless of shear displacement. **Figure 49** shows that, at high compression (h =10Å), compact chains entangle more when they were grafted sufficiently close to each other (*i.e.* $D \leq$ 8Å), while at greater distances the swollen chains entangled more. The 40-bead chains display the crossover trend at h = 15Å; however, **Figure 28** shows that, at higher compression, the 40-bead chains begin to closely resemble the case of n = 50 at h = 15Å in terms of value and trend, crossing at approximately the same distance ($D \approx$ 9Å). As in previous figures, when the chains are less swollen (r_{ex} = 0.5Å) and sufficiently close to each other, they entangled more. When the chains are swollen (r_{ex} = 1.0Å) and at larger distances they entangled more. As we conjectured before, this crossover appears to take place for all chain lengths if a sufficiently high level of compression can be reached.

4.3. Two Chains with Different Length and Composition Under Compression

We have carried out simulations for two chains with different length and excluded volume located directly on top of one another under compression in order to gain insight into the role of

composition on inter-chain entanglements. **Figure 29** shows the behaviour for n_1 = 50 beads and n_2 = 20 beads, [50+20], when h = 15Å. The results can be contrasted with those for [30+30] and [20+20] in **Figure 22.** When the r_{ex} increased and the chains swell, coming into closer proximity to one another, the chains [30+30] and [20+20] increased in inter-chain entanglement. In contrast, the mixed chains [50+20] produce relatively no upward or downward trend in entanglement. By switching one 20 bead chain for the longer 50 bead chain, the chains come into closer proximity and as a result twist away from each other due to strong repulsion between chains. At $r_{ex} \leq 0.7$Å the [50+20] systems entangle more than the [30+30] and [20+20] chains. However, at r_{ex} = 0.8Å, the chains continue increasing in inter-chain entanglement while the [50+20] chains show little change in $\langle \overline{N}_{inter} \rangle$.

Figure 30 compares the [50+30] case with [30+30] and [40+40] at h = 15Å. The [30+30] case increased in entanglement with increasing r_{ex}, while entanglements flatten in the [40+40] case, due to repulsions between the chains leading to chain avoidance. As before, when one 30 bead chain is replaced with the longer chain, the inter-chain entanglement increased significantly compared to the [30+30] chains. However, the overcrossing number remained smaller than the [40+40] chains over the entire ranger of r_{ex}. The [50+30] chains show little change in $\langle \overline{N}_{inter} \rangle$ up until roughly r_{ex} = 0.6Å. As the chains continue to swell, the inter-chain entanglement decreases with r_{ex} due to repulsions between the chains forcing them to twist away and avoid each other.

Figure 31 shows that [50+40] case, and contrasts it with the [40+40] and [50+50] chains at h = 15Å. When one of the 40-bead chains in replaced with a longer 50-bead chain, the inter-chain entanglement is roughly intermediate between values for the [40+40] and [50+50] chains. As the chains swell, the [40+40] chains show nearly constant $\langle \overline{N}_{inter} \rangle$. In contrast, the [50+40] and [50+50] chains decrease in inter-chain entanglement due to stronger repulsions between the chains leading again to chain avoidance.

In all the previous cases, we considered chains of different length but with the same "chemical composition" (*i.e.*, the same r_{ex} value). **Figure 32** expands our analysis by considering [50+30] chains with different r_{ex} values (*e.g.*, a polyethylene chain with low r_{ex} values and a polypropylene chain with larger r_{ex}). When both chains have small r_{ex} values, we expect fewer inter-chain entanglements since the chains interact minimally. Likewise, we anticipate fewer inter-chain entanglements when both chains have larger r_{ex} values since the chains swell and evade each other to reduce repulsions. When one chain has a larger r_{ex} value and the other has a

smaller r_{ex} value, we expect a larger number of inter-chain entanglements as the more compact chain can reach the swollen chain. Otherwise, we find a wide range of combinations [$n_1 + n_2$] and [$r_{ex} + r_{ex}$'] that can lead to the same level of inter-chain entanglement, as represented in the schemes in **Figure 43**:

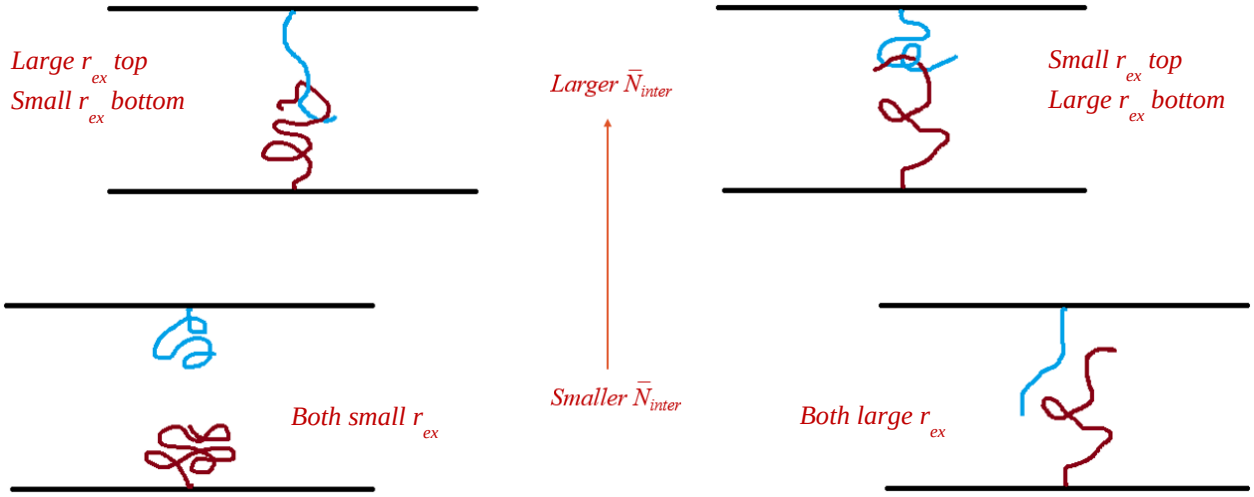

Figure 43: Schematic representation of the effect of chain length and r_{ex} on inter-chain entanglement.

4.4. Three Chains Under Compression

Using three chains, two in the top plane and one on the bottom plane, we studied effects of breaking the symmetry as well as the role of excluded volume under compression. Throughout the three chain simulations, the top two chains (1 and 2) were anchored at fixed positions at 3Å away from each other, while the bottom chain (chain 3) is moved (*cf.* section **2.3.1)**. **Figures 33** and **35**, show the molecular shape descriptors, radius of gyration and intra-chain entanglement of the "linear" and "triangular" geometries, respectively, when the bottom chain (chain 3) is moved from D = 6Å to D = 0Å (see **Figure 15**). **Figure 33** indicates that swelling results in larger mean chain size, and lower intra-chain entanglement. Like the shear displacements involving two chains, breaking the symmetry for the three chains had minimal effect on their intramolecular structure, since the chains are still quite capable of twisting into empty spaces. In no case, however, we find evidence for the formation of coil-and-flower configurations, typical of "escape transitions". The latter are characterized by both large R_g and large $\langle \bar{N}_{intra} \rangle$ values. Our finding

that a large R_g is accompanied by a small $\langle \overline{N}_{intra} \rangle$ points instead simply to the formation of rotated SAWs with uniform spatial distributions of monomer beads.

Figure 34 shows the results for the "triangular" geometry. Like the linear geometry, the shear displacements had minimal effect on intramolecular structure of the chains, producing no distinct trend in either radius of gyration or intra-chain entanglement. By changing the surface coverage to include more than three chains, as well as altering the grafting symmetry, we expect that deformations in the polymer arrangement may lead to the occurrence of escape transitions, whereby a repulsive polymer can partially bend and stretch across the narrow spaces [Arteca, 1997a], probably enhanced by the presence of the compression surface. In the case of low surface coverage, however, there are no such transitions, and the pattern of chain avoidance is independent of the geometrical arrangement (linear or triangular).

The results in **Figure 35** reinforce the emerging picture of structural rearrangements leading to chain avoidance. **Figure 35** compares the inter-chain entanglement between the fixed top chains ($\langle \overline{N}_{inter} \rangle_{1,2}$) as the r_{ex} was altered, and the bottom chain (3) was moved. The difference in inter-chains entanglement between the two geometries is negligible; at such a close distance (3Å), the top chains bend away from each other in order to lower repulsions and avoid easily the bottom chain.

Figure 36 shows the inter-chain entanglement between chains ($\langle \overline{N}_{inter} \rangle_{1,3}$) for both geometries. For the linear geometry, when chain 3 is at D = 0Å, it is directly underneath chain 1. For r_{ex} = 0.5Å, this results in a slight drop in the inter-chain entanglement; since this effect is less noticeable for D = 1Å, it is clearly due to chain avoidance. For the triangular geometry at D = 0Å, chain 3 is at 1.5Å away from both chains 1 and 2, and therefore produces the largest value of inter-chain entanglement. Despite these differences, the change in $\langle \overline{N}_{inter} \rangle_{1,3}$ with D is geometry independent.

Finally, **Figure 37** displays the inter-chain entanglement $\langle \overline{N}_{inter} \rangle_{2,3}$ for the linear geometry, as r_{ex} was altered and chain 3 was displaced. (For the triangular isosceles geometry, obviously we have $\langle \overline{N}_{inter} \rangle_{1,3} = \langle \overline{N}_{inter} \rangle_{2,3}$ by symmetry). At D = 0Å and 6Å, chain 3 is approximately 3Å away from chain 2, while at D = 3Å the two chains (2 and 3) lie directly on top of each other. When the chains are less swollen (smaller r_{ex}), the two chains interact most with each other at D = 3Å since they are at the closest possible distance. As the chains become more swollen (larger r_{ex}), they experience the largest inter-chain entanglement when the chains were

offset slightly, D = 4Å and 5Å. In summary, the linear symmetry distinguishes the interaction (1,3) from the (2,3), but in neither case we observe proper escape transitions.

4.5. Seven Chains Under Compression

For a final insight, we compared the properties of seven identical 20-bead chains in hexagonal packing in two different situations: uncompressed (all seven chains grafted to the same polymer island), and compressed by a second polymer covered surface at h = 15Å. (One chain on the top surface, six chains on the bottom plane, in a regular hexagonal arrangement for the anchors).

The uncompressed case was part of previous research conducted in our lab which looked at the role of surface coverage and geometry on molecular shape ([Harrison, 2014], [Richer *et al*., 2017]). In this thesis, we expand on those simulations and introduce compression, where the center chain (pivot chain) is grafted at the origin on the top plane and the remaining six chains are grafted to the bottom plane in hexagonal formation around the origin. **Figure 39** compares the mean radius of gyration of the two conditions (compressed and uncompressed) as the outer chains are shifted away from the pivot chain, as well as altering the excluded volume. For both the compressed and uncompressed cases, the mean chain size increased at approximately the same rate as r_{ex} increased. The results from the displacement of the outer chains was subtler. The more compact chains (r_{ex} = 0.1Å and 0.2Å) were unaffected by the displacements of the outer chains. The more swollen chains (r_{ex} = 0.3Å and 0.4Å) had similar chain size until D ~ 6Å, at which point the uncompressed chains dramatically increased in size, while the effect was minor on the compressed chains. This difference is due to compression preventing the chains from fully elongating in the z-direction.

Figure 40 shows the same behaviour in terms of asphericity, where configurations with larger R_g-value have also larger Ω-values (more prolate). Both the compressed and uncompressed conditions produced similar values of asphericity when the coordinating (hexagonal) chains were farther away. When the chains were grafted closely together (D ~ 6Å), the uncompressed chains increased more sharply in asphericity than the compressed chains. The results for the intra-chain entanglements (**Figure 41**) are also consistent with the emerging picture: when the swollen chains were grafted closely together (D ~ 6Å), the chains decrease sharply in self-entanglements

as they stretch and twist to lower repulsions by neighbouring chains, the effect being more marked under compression.

Once again, it is when we look at the inter-chain entanglements, $\langle \overline{N}_{inter} \rangle$, that we observe the clearer picture of the role of compression on the interrelation between the chain (**Figure 42**). With and without compression, as the chains move farther away from each other, they are less able to interact and interpenetrate. However, the number of inter-chain entanglements is significantly smaller for the compressed chains. We conclude therefore that in this arrangement, compression does not induce a coil-and-flower transition, but rather forces the chains to "rotate" away from each other to lower repulsions, while conserving their intrinsic shapes (similar to those under no compression).

It is conjectured that the occurrence of "proper" escape transitions will require the presence of high (*e.g.*, hexagonal) coordination, but in broken symmetry, as in the case of uncompressed chains [Richer *et al*., 2017].

Chapter 5

5. Conclusions and Further Work

In this thesis, we used Monte Carlo simulations to study the changes in molecular shape for adsorbed polymers under compression. The structural and shape properties of the chains were described in terms of chain size, anisometry, and entanglement complexity. We studied how chains swell and interpenetrate under various conditions of compression, excluded volumes, and chain lengths. The resulting picture shows that, under high compression, chains interpenetrate as excluded volume increases, leading to an increase in inter-chain entanglement. This effect is more pronounced for longer chain lengths. On the other hand, when chains are shifted away from the other, at constant confinement and excluded volumes, their inter-chain entanglement diminishes. The diminished inter-chain entanglement with larger shear displacement also occurred when the number of chains increased. This indicates that repulsive chains are reoriented with respect to neighbours as they avoid each other. In all cases, we find *critical values* for length, compression, and neighbour density, where we observe a crossover in the relation between $\langle \overline{N}_{inter} \rangle$ and the radius of excluded volume. The key pattern is as follows:

a) Under compression, and for a given number of anchored neighbours, short chains entangle more as they swell compared with longer chains. This indicates a critical chain length to switch from chain interpenetration to chain avoidance.
b) Under compression, and for a given chain length, there is a critical level of crowding that influences how the repulsive polymers entangle among themselves as they swell. We observe a similar switch from low entanglement at high density and extensive swelling, to larger entanglement for chains with smaller excluded-volume interaction.

When examining the effect of compression and excluded volumes on the intra-molecular structure of the chains, we observe that R_g, Ω, and $\langle \overline{N}_{intra} \rangle$ are affected by chain length, swelling, the number and location of neighbouring chains, but much less by confinements (all other control parameters being the same). This indicates that compression does not affect the intrinsic internal structure of these repulsive chains but rather the interrelation with the others.

In conclusion, unlike the intra-molecular shape descriptors, the inter-chain entanglement descriptor proved to be a valuable tool for observing chain avoidance. The strong correlation between large R_g (and large Ω) with small $\langle \overline{N}_{intra} \rangle$ values shows that there are no uneven

distributions of monomers in terms of compactness, hence no proper escape transitions. The behaviour of $\langle \overline{N}_{inter} \rangle$ indicate that the dominant mechanisms by which chains respond to compression, once equilibrium is achieved, is by a somewhat "rigid" chain rotation, in order to minimize chain repulsion.

While the set of shape descriptors (R_g, Ω, $\overline{N}_{intra}$, $\overline{N}_{inter}$) are sufficient for the needs of this thesis, other properties could also be incorporated into the analyses. Among the many available shape descriptor in the literature (*e.g.*, see [Mezey, 1993], [Arteca, 1996a]), some characterize local shape instead of the globular one. These approaches can be useful for differentiating configurations with a uniform distribution of monomers in space (*e.g.*, a compact polymer mushroom) versus configurations with non-uniform distributions (*e.g.*, the coil-and-flower conformers typical of escape transitions). Descriptors to this effect can include the radial distribution of monomers [Allen & Tildesley, 1991], the behaviour of the R_g/R_e ratio (*cf.* Fig. 9) as a function the distance from the centre of mass [Arteca, 1996c] or as function of the monomer position in the chain [Arteca, 1997c], as well as the local ("zoomed") self-entanglements (as opposed the global, full-chain, entanglements) [Arteca, 1993]. Similarly, one could characterize chain avoidance by comparing the relative orientation of the main axes of inertia for individual chains, as opposed to simply using the principal moments of inertia to compute the asphericity (eq. (2.7)).

As well, there are several interesting model systems where these techniques could be applied, gaining further insight into the structure and function of confined macromolecules. We can briefly outline some aread of primising future work:

1) The first project could continue investigating interactions of two *larger* polymer islands (*i.e.*, a modal for lubrication) focusing specifically on the effects of geometry, density of polymer packing, as well as excluded volume interactions. In particular, it would be important to determine the conditions for two polymer covered surfaces to have sufficiently different geometrical arrangements so that they can create the proper constraints that lead to the onset of escape transitions under compression.

2) The second project could focus on heteropolymers, *i.e.*, the possibility of different excluded volume interactions *within* each chain (this thesis exclusively focused on

homopolymers). Investigating heteropolymers presents interesting options for the arrangement of the monomers (*e.g.*, alternating copolymers, block copolymers, random copolymers), as well as allowing the possibility of cross-linking and other polymer topologies.

3) All the simulations considered in this thesis dealt with the case of repulsive homopolymers, where the formation of escaped configurations is not trivial. In the presence of attraction, regions of a homopolymer can be fully stabilized in a compact blob [Subramanian *et al*., 1995], [Klushin and Skvortsov, 2011], and thus escape transitions can take place more easily. The situation would be, however, less trivial in the presence of a very complicated pattern of interactions, *e.g.*, in the case of heteropolymers with a few dominant "native conformations" (*e.g.*, proteins and nucleic acids). Given that improper protein folding and aggregation are essential in gaining insight into the cellular and molecular mechanisms of neurodegenerative diseases such as Alzheimer's disease, Parkinson's disease, amyotrophic lateral sclerosis (ALS), as well as other prion diseases [Bratko & Blanch, 2001], [Javidpour, 2012], it would be valuable to understand how their molecular shapes change under conditions of strong confinement and crowding such as those found inside the cell.

References

Abbou, J., Anne, A., & Demaille, C. (2006). Accessing the dynamics of end-grafted flexible polymer chains by atomic force-electrochemical microscopy. Theoretical modeling of the approach curves by the elastic bounded diffusion model and Monte Carlo simulations. Evidence for compression-induced lateral chain escape. *J. Chem. Phys. B, 110*, 22664-22675.

Acierno, D., & Ziabicki, A. (1977). Statistical theory of entanglement density in linear polymers and fiber systems. III. Three-dimensional entanglement of rigid and flexible chains. *J. Chem. Phys.*, *67*, 2892-2896.

Allen, M. P., & Tildesley, D. J. (1991). Computer simulation of liquids. Oxford University Press. Electronic version.

Arteca, G. A. (1993). Small- and large-scale global shape features in macromolecular backbones. *J. Math. Chem. 12*, 37–51.

Arteca, G. A. (1994). Scaling behaviour of some molecular shape descriptors of polymer chains and protein backbones. *Phys. Rev. E, 49*, 2417–2428.

Arteca, G. A. (1996a). Molecular shape descriptors. In: K.B. Lipkowitz and D.B. Boyd (eds.), *Rev. Computat. Chem., vol. 9, chapt. 5*. VCH Publishers, New York, USA.

Arteca, G. A. (1996b). Molecular shape transitions in grafted polymers under geometrical confinement. *Int. J. Quantum Chem., 30*, 1515–1523.

Arteca, G. A. (1996c). Different molecular size scaling regimes for inner and outer regions of proteins. *Phys. Rev. E 54*, 3044–3047.

Arteca, G. A. (1997a). Shape transitions in polymer mushrooms compressed by a finite-size obstacle. *Int. J. Quantum Chem., 65*, 519–530.

Arteca, G. A. (1997b). Self-similarity in entanglement complexity along the backbones of compact proteins. *Phys. Rev. E 56*, 4516–4520.

Arteca, G. A. (1999). Path-Integral calculation of the mean number of overcrossings in an entangled polymer network. *J. Chem. Inf. Comput. Sci., 39*, 550–557.

Arteca, G. A. (2002). Analytical estimation of scaling behavior for the entanglement complexity of a bond network. *J. Chem. Inf. Comput. Sci.*, *42*, 326–330.

Arteca, G. A. (2003). A measure of folding complexity for D-dimensional polymers. *J. Chem. Inf. Comput. Sci.*, *43*, 63–67.

Arteca, G. A., Edvinsson, T., & Elvingson, C. (2001). Compaction of grafted wormlike chains under variable confinement. *Phys. Chem. Chem. Phys.*, *3*, 3737–3741.

Arteca, G. A., & Tapia, O. (1999). Characterization of fold diversity among proteins with the same number of amino acid residues. *J. Chem. Inf. Comput. Sci.*, *39*, 642–649.

Arteca, G. A., & Tapia, O. (2001a). Structural transitions in neutral and charged proteins in vacuo. *J. Mol. Graph. Model*., 19, 102-118.

Arteca, G. A., Reimann, C. T., & Tapia, O. (2001b). Proteins in vacuo: denaturing and folding mechanisms studied with computer simulated molecular dynamics. *Mass Spect. Rev.*, *20*, 402–422.

Avalle, M., Belingardi, G., & Montanini, R. (2001). Characterization of polymeric structural foams under compressive impact loading by means of energy-absorption diagram. *Int. J. Impact. Eng*., 25, 455-472.

Baiesi, M., Orlandini, E., & Whittington, S. G. (2009). Interplay between writhe and knotting for swollen and compact polymers. *J. Chem. Phys*., 131, 154902(1-9).

Baumgartner, A., & Muthukumar, M. (1987). A trapped polymer chain in random porous media. *J. Chem. Phys.*, *87*, 3082-3088.

Berendsen, H. J. C., Postma, J. P. M., van Gunsteren, W. F., DiNola, A., Haak, J. R. (1984). Molecular dynamics with coupling to an external bath. *J. Chem. Phys.*, *81*, 3684-3690.

Bhattacharjee, S. M., Giacometti, A., & Maritan, A. (2013). Flory theory for polymers. *Cond. Mat. Stat. Mech.*, 1–47.

Bishop, M., & Michels, J. P. J. (1986). Scaling in two-dimensional linear and ring polymers. *J. Chem. Phys.*, *85*, 1074–1076.

Bishop, M., & Saltiel, C. J. (1988). Universal properties of linear and ring polymers. *J. Chem. Phys.*, *89*, 1159–1162.

Bratko, D., & Blanch, H. W. (2001). Competition between protein folding and aggregation: A three-dimensional lattice-model simulation. *J. Chem. Phys*, *114*, 561–569.

Brittain, W. J., & Minko, S. (2007). A structural definition of polymer brushes. *J. Polym. Sci. Polym. Chem.*, *45*, 3505–3512.

Bruna, M., & Chapman, S. J. (2012). Excluded-volume effects in the diffusion of hard spheres. *Phys. Rev. E*, 85: 011103(1-6).

Carlsson, T., Arteca, G. A, Sundberg, J., & Elvingson, C. (2011a). Off-equilibrium response of grafted polymer chains subject to a variable rate of compression. *Phys. Chem. Chem. Phys.*, *13*, 11757–11765.

Carlsson, T., Kamerlin, N., Arteca, G. A, & Elvingson, C. (2011b). Brownian dynamics of a compressed polymer brush model. Off-equilibrium response as a function of surface coverage and compression rate. *Phys. Chem. Chem. Phys.*, *13*, 16084–16094.

Chen, C., & Fwu, Y. (2000). Monte Carlo simulations of polymer brushes. *Phys. Rev. E*, *63*: 011506(1–10).

Chib, S., & Greenberg, E. (1995). Understanding the Metropolis-Hastings algorithm. *Am. Stat. Assoc.*, *49*, 327-335.

Coles, J. M., Chang, D. P., & Zauscher, S. (2010). Molecular mechanisms of aqueous boundary lubrication by mucinous glycoproteins. *Curr. Op. Coll. Interf. Sci*., 15, 406–416.

Craiu, R. V. (2011). Tuning of Markov chain Monte Carlo algorithms using copulas. *U.P.B. Sci. Bull., Series A*, *73*, 5–12.

Cui, W., Su, C. F., Merlitz, H., Wu, C. X., & Sommer, J. U. (2014). Structure of dendrimer brushes: Mean-field theory and MD simulations. *Macromolecules*, *47*, 3645–3653.

Curk, T., Martinez-Veracoechea, F. J., Frenkel, D., & Dobnikar, J. (2014). Nanoparticle organization in sandwiched polymer brushes. *Nano Lett.*, *14*, 2617–2622.

Dimitrov, D. I., Klushin, L. I., Skvortsov, A., Milchev, A., & Binder, K. (2009). The escape transition of a polymer : A unique case of non-equivalence between statistical ensembles. *Eur. Phys. J. E*, *29*, 9–25.

de Gennes, P. (1979). Scaling Concepts in Polymer Physics. Cornell University Press, Ithaca, USA.

Edens, L. E., Brozik, J. A, & Keller, D. J. (2012). Coarse-grained model DNA: structure, sequences, stems, circles, hairpins. *J. Phys. Chem. B, 116*, 14735–14743.

Edvinsson, T., Elvingson, C., & Arteca, G. A. (2000). Variations in molecular compactness and chain entanglement during the compression of grafted polymers. *Macrom. Theory Simul., 9*, 398–406.

Edvinsson, T., Elvingson, C., & Arteca, G. A. (2002). Effect of compression on the molecular shape of polymer mushrooms with variable stiffness. *J. Chem. Phys., 116*, 9510-9517.

Edwards, S. F. (1965). The statistical mechanics of polymers with excluded volume. *Proc. Phys. Soc., 85*, 613–624.

Egorov, S. A, Hsu, H.-P., Milchev, A., & Binder, K. (2015). Semiflexible polymer brushes and the brush-mushroom crossover. *Soft Mat.*, 1–13.

Elliott, I. G., Kuhl, T. L., & Faller, R. (2013). Compression of high grafting density opposing polymer brushes using molecular dynamics simulations in explicit solvent. *J. Phys. Chem. B, 117*, 4134–4141.

Espinosa-Marzal, R. M., Nalam, P. C., Bolisetty, S., & Spencer, N. D. (2013). Impact of solvation on equilibrium conformation of polymer brushes in solvent mixtures. *Soft Matt., 9*, 4045–4057.

Fehske, H., Schneider, R., & Weiße, A. (2008). Computational Many-Particle Physics. Springer, Berlin, Germany. Electronic version.

Flory, G. (1953). Principles of Polymer Chemistry. Cornell University Press, Ithaca, USA.

Fresnais, J., Berret, J.-F., Qi, L., Chapel, J.-P., Castaing, J.-C., Sandre, O., Frka-Petesic, B., Perzynski, R., Oberdisse, J., & Cousin, F. (2008). Universal scattering behavior of coassembled nanoparticle-polymer clusters. *Phys. Rev. E, 78*, 040401(1-4).

Graham, I. S., Piché, L., & Grant, M. (1997). Model for dynamics of structural glasses. *Phys. Rev. E, 55*, 2132–2144.

Grest, G. S., & Murat, M. (1993). Structure of grafted polymeric brushes in solvents of varying auality : A molecular dynamics study. *Macromolecules*, *26*, 3108–3117.

Grosberg, A. Yu., & Khokhlov, A. R. (1997). Giant molecules. Academic Press, San Diego, USA.

Guffond, M. C., Williams, D. R. M., & Sevick, E. M. (1997). End-tethered polymer chains under AFM tips: Compression and escape in theta solvents. *Langmuir*, *13*, 5691–5696.

Häggström, O. (2002). Finite Markov chains and algorithmic applications. Cambridge University Press, Cambridge, UK. Electronic version.

Harmandaris, V. A., Adhikari, N. P., Van Der Vegt, N. F. A., & Kremer, K. (2006). Hierarchical modeling of polystyrene: From atomistic to coarse-grained simulations. *Macromolecules, 39*), 6708–6719.

Harper, C. A., (2002). Handbook of plastics, elastomers, and composites. McGraw Hill, New York, USA.

Harrison, J. (2014). Self-Entanglement in adsorbed clusters of repulsive polymers. Laurentian University (Honours Bachelor of Science in Chemistry thesis), Sudbury, Canada.

Hastings, W. K. (1970). Monte Carlo sampling methods using Markov chains and their applications. *Biometrika, 57*, 97-109.

Haw, S. & Mosey, N. (2012). Tribochemistry of aldehydes sheared between (0001) surfaces of α-alumina from first-principles molecular dynamics. *J. Phys. Chem. C, 116*, 2132-2145.

Hoover, W. G., Ross, M., Johnson, K. W., Henderson, D., Barker, J. A., & Brown, B. C. (1970). Soft sphere equation of state. *J. Chem. Phys.*, *52*, 4931–4941.

Hsu, H. P., Paul, W., & Binder, K. (2014). Pulling single adsorbed bottle-brush polymers off a flat surface: A Monte Carlo simulation. *Macromolecules*, *47*, 427–437.

Hull, D., & Clyne, T. W. (1996). An introduction to composite materials. 2nd Ed. Cambridge University Press, Cambridge, UK.

Hypercube, Inc. (2007). HyperChemTM 8.0.4. http://hyper.com/.

Javidpour, L. (2012). Computer simulations of protein folding. *Comput. Sci. Eng.*, *14*, 97–103.

Jorgensen, W. and Tirado-Rives, J. (1996). Monte Carlo vs molecular dynamics for conformational sampling. *J. Phys. Chem., 100*, 14508-14513.

Kneller, J. M., Elvingson, C., & Arteca, G. A. (2005). Shape transitions induced by mechanical external stretching of grafted self-attractive wormlike chains. *Chem. Phys. Lett., 407*, 384–390.

Kumbar, M. (1973). Hydrodynamic properties of supercoiled linear polymer molecules. *J. Chem. Phys., 58*, 2874–2881.

Lai, P. Y., & Binder, K. (1992). Structure and dynamics of polymer brushes near the theta point - a Monte-Carlo simulation. *J. Chem. Phys., 97*, 586–595.

Larson, R. G., Hu, H., Smith, D. E., & Chu, S. (1999). Brownian dynamics simulations of a DNA molecule in an extensional flow field. *J. Rheol*., 43, 267–304.

L'Écuyer, P. (1990). Random numbers for simulations. *Commun. ACM*., 33, 85-98.

Lee, S. G., Pascal, T. A., Koh, W., Brunello, G. F., Goddard, W. A. I., & Jang, S. S. (2012). Deswelling mechanisms of surface-grafted poly(NIPAAm) brush: Molecular dynamics simulation approach. *J. Phys. Chem. C, 116*, 15974–15985.

Lemak, A. S., Balabaev, N. K., Karnet, Y. N., & Yanovsky, Y. G. (1998). The effect of a solid wall on polymer chain behavior under shear flow. *J. Chem. Phys., 108*, 797–806.

Lennard-Jones, J. (1924). On the determination of molecular fields. II. From the equation of state of a gas. *P. Roy. Soc. A*., 106, 463-477.

Li, F., & Pincet, F. (2007). Confinement free energy of surfaces bearing end-grafted polymers in the mushroom regime and local measurement of the polymer density. *Langmuir, 23*, 12541–12548.

Liao, W.-P., Elliott, I. G., Faller, R., & Kuhl, T. L. (2013). Normal and shear interactions between high grafting density polymer brushes grown by atom transfer radical polymerization. *Soft Matter, 9*, 5753-5761.

Madras, N. & Slade, G. (1993). The Self-avoiding walk. Birkhäuser, Boston, USA.

Marko, J. (2009). Linking topology of tethered polymer rings with applications to chromosome segregation and estimation of the knotting length. *Phys. Rev. E*, 79: 051905(1-16).

Marsaglia, G. (1972). Choosing a point from the surface of a sphere. *Ann. Math. Stat.*, 43, 645-646.

McHugh, S., & Johnston, M. (1977). Surface shear stress, strain, and shear displacement for screw dislocations in a vertical slab with shear modulus contrast. *Geophys. J. R. Astr. Soc.*, 49, 715-722.

Metropolis, N., Rosenbluth, A. W., Rosenbluth, M. N., Teller, A. H., & Teller, E. (1953). Equation of state calculations by fast computing machines. *J. Chem. Phys., 21*, 1087-1092.

Mezey, P.G. (1993). Shape in Chemistry: An introduction to molecular shape and topology. VCH Publishers. New York, USA.

Milchev, A, Yamakov, V., & Binder, K. (2007). Escape transition of a compressed polymer mushroom under good solvent conditions. *Europhys. Lett., 47*, 675–680.

Milchev, A., & Binder, K. (2014). Polymer absorption in dense polymer brushes vs . polymer adsorption on the brush-solvent interface. *Europhys. Lett., 106*, 58001(1-6).

Minko, S. (2006). Responsive polymer brushes. *J. Macromol. Sci. Polym. Rev., 46*, 397–420.

Misra, G. S. (1993). Introductory polymer chemistry. New Age International Publishers.

Mökkönen, H., Ikonen, T., Ala-Nissila, T., & Jónsson, H. (2015). Transition-state theory approach to polymer escape from a one dimensional potential well. *J. Chem. Phys., 142*, 1–22.

Müller-Plathe, F. (2002). Coarse-graining in polymer simulation: From the atomistic to the mesoscopic scale and back. *Chem. Phys. Chem., 3*, 754-769.

Pande, V. S., Sorin, E. J., & Christopher, D. (2008). Computer simulations of protein folding, 161–187.

Paturej, J., Milchev, A., Egorov, S. A., & Binder, K. (2013). The escape transition of a compressed star polymer: Self-consistent field predictions tested by simulation. *Macromolecules, 46*, 8009–8016.

Press, W. H., Teukolsky, S. A., Vetterling, W. T., & Flannery, B. P. (1992). Numerical recipes in Fortran 77. Cambridge University Press. Cambridge, UK.

Prigozhin, M. B., Scott, G. E., & Denos, S. (2014). Mechanical modeling and computer simulation of protein folding. *J. Chem. Educ.*, *91*, 1939-1941.

Richer. M., Harrison, J. E., & Arteca, G. A. (2017). Entanglement complexity and escape transitions in grafted polymer islands. *To be published.*

Rudnick, J., & Gaspari, G. (1986). The asphericity of random walks. *J. Phys*. *A.*,19, L(191-193).

Sheng, Y.-J., & Liao, C.-S. (2003). The effect of topological constraint on the theta temperature of a knotted polymer. *J. Chem. Phys.*, *118*, 4748–4753.

Skvortsov, A. M., Klushin, L. I., & Leermakers, F. A. M. (2006). On the escape transition of a tethered Gaussian chain; exact results in two conjugate ensembles. *Macromol. Symp.*, *237*, 73–80.

Stellman, S. D., & Gans, P. J. (1972). Efficient computer simulation of polymer conformation. I. Geometric properties of the hard-sphere model. *Macromol.*, *5*, 516–526.

Teraoka, I. (2002). Polymer solutions: An introduction to physical properties. John Wiley & Sons, New York, USA. Electronic version.

Todeschini, R., & Consonni, V. (2000). Descriptors from molecular geometry, 1004–1033.

Velichko, Y. S., Yoshikawa, K., & Khokhlov, A. R. (1999). Effect of twisting on the behavior of a double-stranded polymer chain: A Monte Carlo simulation. *J. Chem. Phys.*, *111*, 9424–9433.

Viot, P., Beani, F., & Lataillade, J.-L. (2005). Polymeric foam behaviour under dynamic compressive loading. *J. Mater. Sci*., 40, 5829-5837.

Vollhardt & Schore. (2011). Organic chemistry: Structure and function. 6th Ed. W. H. Freeman and Company, New York, USA.

Wajnryb, E., Szymczak, P., & Cichocki, B. (2004). Brownian dynamics: divergence of mobility tensor. *Physica A*, *335*, 339–358.

Weir, M. P., & Parnell, A. J. (2011). Water soluble responsive polymer brushes. *Polym*, *3*, 2107–2132.

Yamakawa, H. (1971). Modern theory of polymer solutions. Harper and Row, New York, USA. Electronic Version.

Yamakawa, H., & Yoshizaki, T. (2003). A Monte Carlo study of effects of chain stiffness and chain ends on dilute solution behavior of polymers. I. Gyration-radius expansion factor. *J. Chem. Phys.*, *118*, 2911-2918.

Young, R. J., & Lovell, P. A. (2011). Introduction to polymers. 3rd Ed. CRC Press, Boca Ratón, USA.

Zhao, B., & Brittain, W. J. (2000). Polymer brushes: surface-immobilized macromolecules. *Prog. Polym. Sci.*, *25*, 677–710.

Ziabicki, A. (1976). Statistical theory of entanglement density in linear polymers and fiber systems. I. General considerations. *J. Chem. Phys.*, *64*, 4100–4106.

Appendices

Appendix 1: Monte Carlo Trajectory Generating Program

This program (*MC_polymer-trajectory_generator_2-plates_Lecuyer_siv2_Gustavo_v5_TEST.f*) generates the configurations for the repulsive end-grafted chains (section **2.3.2**). Note that the subroutine used in the random number generation was not included. The random number generation uses a L'Écuyer random number generator with Bays-Durham shuffle.

```
C ***************************************************************************
C                                                                            *
C                    (Program under development; experimental use)           *
C                    (c)  COPYRIGHT BY: G.A. ARTECA, 1993-2017               *
C                    This version was modified by Jessica Harrison, 2014-2017*
C                                                                            *
C  NO PART OF THIS CODE MAY BE COPIED OR REDISTRIBUTED WITHOUT THE           *
C  WRITTEN PERMISSION OF THE COPYRIGHT OWNER.                                *
C                                                                            *
C  THE COPYRIGHT OWNER DOES NOT TAKE ANY RESPONSIBILITY FOR ANY              *
C  ERRORS IN THE CODE OR DOCUMENTATION.                                      *
C                                                                            *
C          Department of Chemistry and Biochemistry                          *
C          Laurentian University                                             *
C          Sudbury, Ontario, Canada P3E 2C6.                                 *
C                                                                            *
C ***************************************************************************
      IMPLICIT REAL*8 (A-H,O-Z)
      CHARACTER*160 COMMAND,trajectory_file
      CHARACTER*1 Restart_answer
      CHARACTER*3 Wall_answer,junk
      INTEGER*4 i2_seed
C  Note that the initial dimensions are up to 20 chains with 101 monomer beads each (including the
C  anchor) on both the top and bottom plate
      DIMENSION X(20,0:100),Y(20,0:100),Z(20,0:100)
      DIMENSION X2(20,0:100),Y2(20,0:100),Z2(20,0:100)
      READ(5,*)COMMAND
```

```
      OPEN(UNIT=49,FILE=COMMAND,STATUS='UNKNOWN')
      read(49,*)n_chainb
      read(49,*)n_conf
      read(49,*)n_traj
      read(49,*)n_lengthb
      read(49,*)r_bondb
      read(49,*)r_exclb
C  ENTER ISEED FOR THE RANDOMIZER < 900 000 000
      read(49,*)i2_seed
      read(49,*)trajectory_file
      read(49,8000)Restart_answer
      read(49,8001)Wall_answer
8000  format(a1)
8001  format(a3)
      if(Wall_answer.eq.'YES')then
            read(49,*)height_L
            read(49,*)n_chaint
            read(49,*)n_lengtht
            read(49,*)r_bondt
            read(49,*)r_exclt
      else if(Wall_answer.eq.' NO')then
            read(49,*)junk
                  height_L=1000.d0
            read(49,*)junk
                  n_chaint=0
            read(49,*)junk
                  n_lengtht=0
            read(49,*)junk
                  r_bondt=0
            read(49,*)junk
                  r_exclt=0
      endif
C  Reading anchor points for the n_chaint grafted polymers (corresponding to bead number 0!)
C  Bottom plate
```

```
      do ij=1,n_chainb
            read(49,*)X(ij,0),Y(ij,0),Z(ij,0)
      enddo

C  Top plate
7112  do ij=1,n_chaint
            read(49,*)X2(ij,0),Y2(ij,0),Z2(ij,0)
      enddo
      close(49)
      write(6,*)'Done with reading anchor beads: ',n_chainb,
     1  ' and ',n_chaint,' chains.'

C  Warm-up for the random no. generator
      do k=1,11
            rr=ran_2(i2_seed)
      enddo
      ERROR=1.D-14
      PI=DACOS(-1.D0)
C  Start building the trajectories. Inside every trajectory, chains are built one at a time, always checking
C  for excluded volume (r_excl). In naive MC, rejection is absolute. Points are placed on the sphere of
C  radius r_bondb using Marsaglia's algorithm. Statistics of accepted and rejected configurations
            an_rejected=0.
            k_progress_index=0
            i_progress = 10
            n_accepted=n_traj*n_conf

C  Initializations:
      OPEN(UNIT=40,FILE=trajectory_file,STATUS='UNKNOWN')
      j_traj_count = 0
      float_max_rejected = 10.D+14

C  Opening the first trajectory
7004        j_traj_count = j_traj_count + 1
            j_conf_count = 0
```

```
C  Opening the first conformation of n_chains
7005            j_conf_count = j_conf_count + 1

C   Building first bead along the z-direction from the chain anchor Initializing all beads except the anchors
C   (read) [and re-initializing if the config has been rejected]
7002    do 7021 ki=1,n_chainb
          do 7022 kj=1,n_lengthb
                x(ki,kj)=0.d0
                y(ki,kj)=0.d0
                z(ki,kj)=0.d0
7022        continue
7021    continue
                j_chain_count = 0
7003            j_chain_count = j_chain_count + 1
        x(j_chain_count,1)=x(j_chain_count,0)
        y(j_chain_count,1)=y(j_chain_count,0)
        z(j_chain_count,1)=z(j_chain_count,0) + r_bondb
        do 7010 j_bead = 2,n_lengthb
5553    rand1=ran_2(i2_seed)
                rand2=ran_2(i2_seed)

C  Marsaglia's algorithm: randomized point on the unit sphere, with centre at (0,0,0)
      rand11=1.d0-2.d0*rand1
      rand22=1.d0-2.d0*rand2
      xxx=rand11**2+rand22**2
      if(xxx.gt.1.d0)go to 5553
      xv=2.d0*rand11*dsqrt(1.d0-xxx)
      yv=2.d0*rand22*dsqrt(1.d0-xxx)
      zv=(1.d0-2.d0*xxx)
      x(j_chain_count,j_bead) = x(j_chain_count,j_bead-1) + r_bondb*xv
      y(j_chain_count,j_bead) = y(j_chain_count,j_bead-1) + r_bondb*yv
      z(j_chain_count,j_bead) = z(j_chain_count,j_bead-1) + r_bondb*zv
```

```
C  Checking whether the new bead is below the adsorbing plane z=0
        if(z(j_chain_count,j_bead).lt.0.)an_rejected=an_rejected+1.d0
        float_n_rejected = an_rejected
                if(float_n_rejected.gt.float_max_rejected)go to 7040
                        if(z(j_chain_count,j_bead).lt.0.)go to 7002
                        if(Wall_answer.eq.' NO')go to 7020

C  Checking whether the new bead is above the upper confining plane
        if(z(j_chain_count,j_bead).gt.height_L)THEN
                an_rejected=an_rejected+1.d0
                float_n_rejected = an_rejected
                if(float_n_rejected.gt.float_max_rejected)go to 7040
                        if(z(j_chain_count,j_bead).gt.height_L)go to 7002
        endif

C  Controlling excluded volume with previous (nonbonded) beads. If dist is smaller than r_excl for any
C  bead, the entire set of chains (i.e., the conformation of n-chains) is rebuilt.
7020    do j2_bead = 0, j_bead-2
          aa=(x(j_chain_count,j2_bead)-x(j_chain_count,j_bead))
          bb=(y(j_chain_count,j2_bead)-y(j_chain_count,j_bead))
          cc=(z(j_chain_count,j2_bead)-z(j_chain_count,j_bead))
          dist=dsqrt(aa*aa+bb*bb+cc*cc)
                if(dist.lt.r_exclb)an_rejected=an_rejected+1.d0
                float_n_rejected = an_rejected
                        if(float_n_rejected.gt.float_max_rejected)go to 7040
                        if(dist.lt.r_exclb)go to 7002
         enddo

C  Checking for excluded volume with the previously built (completed) chains
        if(j_chain_count.eq.1)go to 7010
        do j2_chain_count=1,j_chain_count-1
          do j3_bead=0,n_lengthb
                aa=(x(j2_chain_count,j3_bead)-x(j_chain_count,j_bead))
                bb=(y(j2_chain_count,j3_bead)-y(j_chain_count,j_bead))
```

```
                cc=(z(j2_chain_count,j3_bead)-z(j_chain_count,j_bead))
                dist=dsqrt(aa*aa+bb*bb+cc*cc)
                        if(dist.lt.r_exclb)an_rejected=an_rejected+1.d0
                        float_n_rejected = an_rejected
                           if(float_n_rejected.gt.float_max_rejected)go to 7040
                           if(dist.lt.r_exclb)go to 7002
             enddo
          enddo

C  Close successfully the loop for the chain being built and checked
7010      continue

C  Move to build the next bottom chain within the same conformation
          if(j_chain_count.eq.n_chainb)go to 7102
          go to 7003

C  Building first bead along the z-direction from the chaint anchor. Initializing all beads to zero, except
C  the anchors (read) [and re-initializing if the config has been rejected]
7102      do 7121 ki=1,n_chaint
             do 7122 kj=1,n_lengtht
                   X2(ki,kj)=0.d0
                   Y2(ki,kj)=0.d0
                   Z2(ki,kj)=0.d0
7122          continue
7121      continue
                   k_chain_count = 0
7103               k_chain_count = k_chain_count + 1
          X2(k_chain_count,1)=X2(k_chain_count,0)
          Y2(k_chain_count,1)=Y2(k_chain_count,0)
          Z2(k_chain_count,1)=Z2(k_chain_count,0) - r_bondt
          do 7110 k_bead = 2,n_lengtht

5554      rand1=ran_2(i2_seed)
                   rand2=ran_2(i2_seed)
```

```
C  Marsaglia's algorithm: randomized point on the unit sphere, with centre at (0,0,0)
          rand11=1.d0-2.d0*rand1
          rand22=1.d0-2.d0*rand2
          xxx=rand11**2+rand22**2
          if(xxx.gt.1.d0)go to 5554
          xv=2.d0*rand11*dsqrt(1.d0-xxx)
          yv=2.d0*rand22*dsqrt(1.d0-xxx)
          zv=(1.d0-2.d0*xxx)
          X2(k_chain_count,k_bead) = X2(k_chain_count,k_bead-1) + r_bondt*xv
          Y2(k_chain_count,k_bead) = Y2(k_chain_count,k_bead-1) + r_bondt*yv
          Z2(k_chain_count,k_bead) = Z2(k_chain_count,k_bead-1) + r_bondt*zv

C  Checking whether the new bead is below the adsorbing plane z=0
          if(Z2(k_chain_count,k_bead).lt.0.)an_rejected=an_rejected+1.d0
          float_n_rejected = an_rejected
                    if(float_n_rejected.gt.float_max_rejected)go to 7040
                              if(Z2(k_chain_count,k_bead).lt.0.)go to 7102

C  Checking whether the new bead is above the upper confining plane
          if(Z2(k_chain_count,k_bead).gt.height_L)THEN
         an_rejected=an_rejected+1.d0
         float_n_rejected = an_rejected
                    if(float_n_rejected.gt.float_max_rejected)go to 7040
                              if(Z2(k_chain_count,k_bead).gt.height_L)go to 7102
          ENDIF

C  Controlling excluded volume with previous (nonbonded) beads. If dist is smaller than r_excl for any
C  bead, the entire set of chains (i.e., the conformation of n-chains) is rebuilt.
7120      do k2_bead = 0, k_bead-2
                    aa=(X2(k_chain_count,k2_bead)-X2(k_chain_count,k_bead))
                    bb=(Y2(k_chain_count,k2_bead)-Y2(k_chain_count,k_bead))
                    cc=(Z2(k_chain_count,k2_bead)-Z2(k_chain_count,k_bead))
                    dist=dsqrt(aa*aa+bb*bb+cc*cc)
```

```
            if(dist.lt.r_exclt)an_rejected=an_rejected+1.d0
            float_n_rejected = an_rejected
                  if(float_n_rejected.gt.float_max_rejected)go to 7040
                  if(dist.lt.r_exclt)go to 7102
      enddo

C  Checking for excluded volume with the previously built (completed) chains
      if(k_chain_count.eq.1)go to 7110
      do k2_chain_count=1,k_chain_count-1
         do k3_bead=0,n_lengtht
            aa=(X2(k2_chain_count,k3_bead)-X2(k_chain_count,k_bead))
            bb=(Y2(k2_chain_count,k3_bead)-Y2(k_chain_count,k_bead))
            cc=(Z2(k2_chain_count,k3_bead)-Z2(k_chain_count,k_bead))
            dist=dsqrt(aa*aa+bb*bb+cc*cc)
            if(dist.lt.r_exclt)an_rejected=an_rejected+1.d0
            float_n_rejected = an_rejected
                  if(float_n_rejected.gt.float_max_rejected)go to 7040
                  if(dist.lt.r_exclt)go to 7102
         enddo
      enddo

C  Checking for excluded volume with the previously built bottom plate
      do j_chain_count=1,n_chainb
         do j_bead=1,n_lengthb
      aa=(X(j_chain_count,j_bead)-X2(k_chain_count,k_bead))
      bb=(Y(j_chain_count,j_bead)-Y2(k_chain_count,k_bead))
      cc=(Z(j_chain_count,j_bead)-Z2(k_chain_count,k_bead))
      dist=dsqrt(aa*aa+bb*bb+cc*cc)
      if(dist.lt.max(r_exclb,r_exclt))then
            an_rejected=an_rejected+1.d0
            float_n_rejected = an_rejected
            if(float_n_rejected.gt.float_max_rejected)go to 7040
                  if(Restart_answer.eq.'1') go to 7002
                  else if(Restart_answer.eq.'2') then
```

```
                    go to 7102
                    endif
          enddo
        enddo

C  Close successfully the loop for the chain being built and checked
7110    continue

C  Move to build the next chain within the same conformation
        if(k_chain_count.eq.n_chaint)go to 7006
        go to 7103

C  Finished with building a single config with n_chains, each with n_length beads. Ready to dump the
C  coordinates in the output file
7006    do jj=1,n_chainb
          do ii=0,n_lengthb
        write(40,8003)X(jj,ii),Y(jj,ii),Z(jj,ii)
          enddo
        enddo
8003    format(3(F11.6,1x))
7106    do jj=1,n_chaint
          do ii=0,n_lengtht
        write(40,8103)X2(jj,ii),Y2(jj,ii),Z2(jj,ii)
          enddo
        enddo
8103    format(3(F11.6,1x))

C  Move to the next conformation in the same trajectory
        if(j_conf_count.eq.n_conf)go to 7007
        k_progress_index = k_progress_index + 1

C  Estimation of progress
              jaz=100*k_progress_index/n_accepted
        if(jaz.eq.i_progress)write(6,*)'reached =',jaz,' %'
```

```
          if(jaz.eq.i_progress)i_progress=i_progress+10
          go to 7005

C  Move to the next trajectory
7007      if(j_traj_count.eq.n_traj)go to 7008
                    k_progress_index = k_progress_index + 1

C  Estimation of progress
          jaz=100*k_progress_index/n_accepted
          if(jaz.eq.i_progress)write(6,*)'reached =',jaz,' %'
          if(jaz.eq.i_progress)i_progress=i_progress+10
          go to 7004
7040      write(6,*)' Aborted because of too many rejections'
7008      close(40)
          write(6,*)' Total number of config created: ',
         1  k_progress_index+1,' Number rejected: ',an_rejected

          end
```

Appendix 2: Molecular Shape Analysis Program

This program (*allxs-scan-trajectory_inter-intra_overcrossings_Gustavo_v4_GENERALIZED.f*) reads the output from the previous program and then calculates the radius of gyration, asphericity, and intra-chain entanglement for each chain as well as the average values and statistical fluctuations in the MC set (section **2.3.2**). The subroutines used in asphericity and eccentricity calculations as well as the random number generation are not included in the following code. Calculations of real and complex roots of polynomials was done using the Lin-Bairstow method.

```
C ***************************************************************************
C       allxs.FOR: scan version to run on trajectory. files                    *
C  UPPSALA 1998: This version incorporates also the aspher-scan.f into a single tabulation.  *
C          (Program under development; experimental use)                      *
C                                                                             *
C        (c)  BY: G.A. ARTECA, 1993-1998, 1998-2017                           *
C                                                                             *
C            Department of Chemistry and Biochemistry                         *
C            Laurentian University                                            *
C            Sudbury, Ontario, Canada P3E 2C6.                                *
C ***************************************************************************
C  Default dimensions:
C  Number of monomers:          100.
C  Number of crossings:         1000.
C  Number of chains:            20.
      IMPLICIT REAL*8 (A-H,O-Z)
      CHARACTER*160 COMMAND,trajectory_file,analysis_file,analysis_file2
      CHARACTER*3 Answer
      INTEGER*4 i2_seed,dummy
      common F(0:30),B(0:30),DBU(0:30),DBV(0:30)

C  Note that beads are counted from bead 1 = anchor (old bead 0)
      DIMENSION X(20,100),Y(20,100),Z(20,100),
     1  Xshift(20,100),Yshift(20,100),Zshift(20,100),
     2  xcom(20),ycom(20),zcom(20),xx(20,100),yy(20,100),zz(20,100),
```

```
     3    VIX(100),VIY(100),VIZ(100),n_length(7),
     4    NCROSS(300),QCROSS(300,3),sum(0:300),irange(10,2),
     5    sum_ref(0:300),rspan(20),ree(20),rg(20),anav_ii(20),
     6    aspher(20),ecc(20),amax(20),nmax(20)

          READ(5,*)COMMAND
          OPEN(UNIT=49,FILE=COMMAND,STATUS='UNKNOWN')
          read(49,*)n_chain
                anchain=n_chain
          read(49,*)n_conf
          read(49,*)n_traj
          do ilengths=1,n_chain
                read(49,*)n_length(ilengths)
          enddo
          read(49,*)r_bond
          read(49,*)i_pivot_chain
          read(49,8001)Answer
8001      format(a3)
          read(49,*)trajectory_file
          read(49,*)analysis_file
          read(49,*)analysis_file2

C  Enter seed for the randomized projections.
          read(49,*)i2_seed
          read(49,*)itotal
          read(49,*)u0
          read(49,*)v0
          CLOSE(49)

C  Introducing a counter for configurations to follow the % of progress later
                kij=0
                i_progress = 10
          open(unit=50,file=trajectory_file,status='unknown')
          open(unit=51,file=analysis_file,recl=140,status='unknown')
```

```
      write(51,*)'       ---------- Configurational properties
     1 averaged over all chains ----------'
      write(51,*)' '
      write(51,*)' Conf    Rg    SD_Rg    Ree    SD_Ree    Asp    SD_Asp
     1 Nav_i  SD_Navi  N*  SD_N*   Rg_piv   Ree_piv   Asp_piv  Nav_piv'

      open(unit=52,file=analysis_file2,recl=140,status='unknown')
      write(52,*)'       ---------- Individual chain properties',
     1 ' ----------'
      write(52,*)' '
      write(52,*)'Conf  Rg1  Rg2   Rg3   Rg4  Rg5  Rg6  Rg7   Asp1 ',
     1 ' Asp2  Asp3   Asp4   Asp5  Asp6  Asp7  Nav_1  Nav_2  Nav_3  ',
     2 ' Nav_4  Nav_5  Nav_6   Nav_7'

            ERROR=1.D-14
            PI=DACOS(-1.D0)

C  N_length is the number of monomer beads per chain. N_chain is the number of chains per
C  configuration. N_conf*N_traj is the number of configurations
      floated_itotal = itotal

C  Total number of atoms
            Nat_tot=0
      do ilengths=1,n_chain
            Nat_tot=Nat_tot+N_length(ilengths)
      enddo
      Anat_tot=Nat_tot
      n_config = n_conf*n_traj

C  Reading the current configuration: (N_length*N_chain) beads. Index kij is the double counter for the
C  total number of configurations (either in the same trajectory or in different ones).
1020        kij = kij + 1
      do i=1,N_chain
        do j=1,n_length(i)
```

```
            read(50,*)X(i,j),Y(i,j),Z(i,j)
          enddo
        enddo
        do 1111 i=0,300
        sum(i)=0.d0
1111    continue

C  Determine the geometrical centre of the entire conformation (to be the centre of the sphere used for
C  projections): xc,yc,zc. Determine the geometrical centre for each chain (xcom,ycom,zcom)
        XC=0.D0
        YC=0.D0
        ZC=0.D0
        do i=1,N_chain
            xcom(i)=0.d0
            ycom(i)=0.d0
            zcom(i)=0.d0
        enddo
        do 2 i=1,N_chain
          DO 2 J=1,N_length(i)
            XC=XC+X(I,J)
            YC=YC+Y(I,J)
            ZC=ZC+Z(I,J)
            xcom(i)=xcom(i)+x(i,j)
            ycom(i)=ycom(i)+y(i,j)
            zcom(i)=zcom(i)+z(i,j)
2       continue
C  Global (all-chain) centroid
        XC=XC/Anat_tot
        YC=YC/Anat_tot
        ZC=ZC/Anat_tot

C  Individual chain centroids
        do i=1,N_chain
            anat=n_length(i)
```

```
                xcom(i)=xcom(i)/anat
                ycom(i)=ycom(i)/anat
                zcom(i)=zcom(i)/anat
        enddo

C  Every chain is now shifted to its individual c.o.m. to compute the intra-chain overcrossings, and all
C  chains are shifted to the global centre of mass for the Nav-global. XX,YY,ZZ: global shifting.
        do 3 i=1,N_chain
          do 3 j=1,N_length(i)
                Xshift(i,J)=X(i,J)-xcom(i)
                Yshift(i,J)=Y(i,J)-ycom(i)
                Zshift(i,J)=Z(i,J)-zcom(i)
                XX(i,J)=X(i,J)-xc
                YY(i,J)=Y(i,J)-yc
                ZZ(i,J)=Z(i,J)-zc
3       continue

C  Find the radius of the smallest sphere, centered at the new origin, which encloses all chains completely
C  (and related properties). Find also the same parameters (rspan,ree,rg) for individual chains.
        R=DSQRT(XX(1,1)**2+YY(1,1)**2+ZZ(1,1)**2)
        DO 4 I=1,N_Chain
        rspan(i)=dsqrt(xshift(i,1)**2+yshift(i,1)**2+zshift(i,1)**2)
        DO 4 J=2,N_length(i)
                S=DSQRT(XX(i,J)**2+YY(i,J)**2+ZZ(i,J)**2)
                sc=DSQRT(Xshift(i,J)**2+Yshift(i,J)**2+Zshift(i,J)**2)
                IF(S.GT.R)R=S
                if(sc.gt.rspan(i))rspan(i)=sc
4       CONTINUE

C  Global Radius of gyration, Rgyr
        rgyr=0.d0
        do 3330 i=1,N_chain
          DO 3330 J=1,N_length(i)
3330     rgyr=rgyr+(xx(i,J)**2+yy(i,j)**2+zz(i,j)**2)
```

```
      rgyr=dsqrt(rgyr/anat_tot)

C  Radius of gyration and ree for individual chains. (These include the pivot chains with index
C  i_pivot_chain)
      do i=1,N_chain
      rg(i)=0.d0
        DO J=1,N_length(i)
            rg(i)=rg(i)+(xshift(i,j)**2+yshift(i,j)**2+zshift(i,j)**2)
        enddo
        rg(i)=dsqrt(rg(i)/anat)
        ree(i)=(xshift(i,1)-xshift(i,N_length(i)))**2
        ree(i)=ree(i)+(yshift(i,1)-yshift(i,N_length(i)))**2
        ree(i)=ree(i)+(zshift(i,1)-zshift(i,N_length(i)))**2
        ree(i)=dsqrt(ree(i))
      enddo

C  Averaged (and std dev) radius of gyration per chain: rg_av,rg_sd
      rg_av=0.d0
      rg_sd=0.d0
      do i=1,N_chain
            rg_av=rg_av+rg(i)
      enddo
      rg_av=rg_av/anchain
      do i=1,N_chain
            rg_sd=rg_sd+(rg(i)-rg_av)**2
      enddo
      rg_sd=dsqrt(rg_sd/anchain)

C  Averaged (and std dev) end-end distance per chain: ree_av,ree_sd
      ree_av=0.d0
      ree_sd=0.d0
      do i=1,N_chain
            ree_av=ree_av+ree(i)
      enddo
```

```
      ree_av=ree_av/anchain
      do i=1,N_chain
            ree_sd=ree_sd+(ree(i)-ree_av)**2
      enddo
      ree_sd=dsqrt(ree_sd/anchain)

C  Asphericity, Asp, and eccentricity, ecc, per chain
      call asphericity(n_length,n_chain,xshift,yshift,zshift,
     1  u0,v0,aspher,ecc)

C  Estimation of progress
      jaz=100*kij/n_config
      if(jaz.eq.i_progress)write(6,*)'reached =',jaz,' %'
            if(jaz.eq.i_progress)i_progress=i_progress+10

C _____________________________________________________
C  Beginning the analysis of intra-chain overcrossings
C _____________________________________________________
            k_chain = 0
1010  k_chain = k_chain + 1
      r_chain=rspan(k_chain)
3335  DO 33355 IRAND=1,ITOTAL
5553  RAND1=ran_2(I2_SEED)
      RAND2=ran_2(I2_SEED)

C  Marsaglia's algorithm.
      rand11=1.d0-2.d0*rand1
      rand22=1.d0-2.d0*rand2
      xxx=rand11**2+rand22**2
      if(xxx.gt.1.d0)go to 5553
      xv=2.d0*r_chain*rand11*dsqrt(1.d0-xxx)
      yv=2.d0*r_chain*rand22*dsqrt(1.d0-xxx)
      zv=r_chain*(1.d0-2.d0*xxx)
2015  continue
```

```
202     AN=DSQRT(XV**2+YV**2+ZV**2)

C  The viewing direction is normalized to the radius of the sphere.
        AN=r_chain/AN
        XV=AN*XV
        YV=AN*YV
        ZV=AN*ZV

C  Project every point of the backbone to the plane, tangent to the sphere and perpendicular to the viewing
C  direction.
350     IF(DABS(XV).LT.ERROR)GO TO 10
        C1=((YV/XV)**2+1.D0)
        C2=YV*ZV/XV**2
        C3=((ZV/XV)**2+1.D0)
        DETER=C1*C3-C2**2
        IF(DABS(DETER).LT.ERROR)GO TO 2002

        DO 5 J=1,N_length(k_chain)
                CY=Yshift(k_chain,J)-YV*Xshift(k_chain,J)/XV
    1           +(Rspan(k_chain)/XV)**2*YV
                CZ=Zshift(k_chain,J)-ZV*Xshift(k_chain,J)/XV
    1           +(Rspan(k_chain)/XV)**2*ZV
                IF(DABS(CY).LT.ERROR.AND.DABS(CZ).LT.ERROR)WRITE(6,*)
    1           ' BEWARE OF HOMOGENEOUS SYSTEMS!'
                ANUM=CY*C3-C2*CZ
                VIY(J)=ANUM/DETER
                ANUM2=C1*CZ-C2*CY
                VIZ(J)=ANUM2/DETER
5       VIX(J)=(Rspan(k_chain)**2-YV*VIY(J)-ZV*VIZ(J))/XV
        GO TO 40
2002    DO 2003 J=1,N_length(k_chain)
                ANUM3=(Xshift(k_chain,J)-XV)*
    1           (Rspan(k_chain)**2/XV-Xshift(k_chain,J))
    2           +(CY/C1-Yshift(k_chain,J))*(Yshift(k_chain,J)-YV)
```

```
     3          -Zshift(k_chain,J)*(Zshift(k_chain,J)-ZV)
     4          -YV*(Xshift(k_chain,J)-XV)*CY/(XV*C1)
                DENOM=ZV*(Xshift(k_chain,J)-XV)/XV+
     1          C2*(Yshift(k_chain,J)-YV)/C1-(Zshift(k_chain,J)-ZV)-
     2          YV*(Xshift(k_chain,J)-XV)*CY/(XV*C1)
                IF(DABS(DENOM).LT.ERROR)STOP
                VIZ(J)=ANUM3/DENOM
                VIY(J)=(CY-C2*VIZ(J))/C1
2003    VIX(J)=(Rspan(k_chain)**2-YV*VIY(J)-ZV*VIZ(J))/XV
        GO TO 40
10      IF(DABS(YV).LT.ERROR)GO TO 20
        C4=((ZV/YV)**2+1.D0)
        DO 6 J=1,N_length(k_chain)
                VIX(J)=Xshift(k_chain,J)
                VIZ(J)=(Zshift(k_chain,J)
     1          +(Rspan(k_chain)/YV)**2*ZV-ZV*Yshift(k_chain,J)/YV)/C4
                VIY(J)=(Rspan(k_chain)**2-ZV*VIZ(J))/YV
6       CONTINUE
        GO TO 40
20      IF(DABS(ZV).LT.ERROR)STOP
        DO 7 J=1,N_length(k_chain)
                VIX(J)=Xshift(k_chain,J)
                VIY(J)=Yshift(k_chain,J)
7       VIZ(J)=Rspan(k_chain)**2/ZV
40      CONTINUE

C  At this point, the backbone is transformed in a planar curve, in general with self-crossings stores in the
C  VIX,... vectors. The next section computes the vector of crossings indices, which gives the graph-
C  theoretical characterization of the projected curve.
                ICROSS=0
                NCROSS(ICROSS+1)=0

C  Start here the computation of vectors CROSS Crossings are checked between a segment and all the
C  following,
```

```
C  except for the very next linked to it (they cannot overcross, of course).  The orientation of the
C  overcrossing is decided by computing the scalar product with the viewing direction for the vector
C  product of the overcrossed segments.  The handedness is finally evaluated after computing the
C  distances of the overcrossed points to the actual crossing on the tangent sphere.
      DO 500 I=1,N_length(k_chain)-3
        DO 501 IP=I+2,N_length(k_chain)-1

C  Crossing analyzed: i-->i+1 with ip-->ip+1
      DET=-(VIX(I+1)-VIX(I))*(VIY(IP+1)-VIY(IP))+
     1  (VIX(IP+1)-VIX(IP))*(VIY(I+1)-VIY(I))
      IF(DABS(DET).GT.ERROR)GO TO 510

C  Overcrossings cannot be computed for this view, since all points lie on a x=const or y=const plane.
C  Equations are solved for other pairs of variables.
      IF(DABS(VIX(I+1)-VIX(I)).LT.ERROR.AND.DABS(
     1  VIX(IP+1)-VIX(IP)).LT.ERROR)GO TO 5101
      IF(DABS(VIY(I+1)-VIY(I)).LT.ERROR.AND.DABS(
     1  VIY(IP+1)-VIY(IP)).LT.ERROR)GO TO 5102
      GO TO 501
5101  DET=-(VIZ(I+1)-VIZ(I))*(VIY(IP+1)-VIY(IP))+
     1  (VIZ(IP+1)-VIZ(IP))*(VIY(I+1)-VIY(I))
      IF(DABS(DET).LT.ERROR)GO TO 501
      AN1=-(VIZ(IP)-VIZ(I))*(VIY(IP+1)-VIY(IP))+(VIZ(IP+1)
     1  -VIZ(IP))*(VIY(IP)-VIY(I))
      AN2=-(VIZ(IP)-VIZ(I))*(VIY(I+1)-VIY(I))+(VIZ(I+1)
     1  -VIZ(I))*(VIY(IP)-VIY(I))
      GO TO 5013
5102  DET=-(VIX(I+1)-VIX(I))*(VIZ(IP+1)-VIZ(IP))+
     1  (VIX(IP+1)-VIX(IP))*(VIZ(I+1)-VIZ(I))
      IF(DABS(DET).LT.ERROR)GO TO 501
      AN1=-(VIX(IP)-VIX(I))*(VIZ(IP+1)-VIZ(IP))+(VIX(IP+1)
     1  -VIX(IP))*(VIZ(IP)-VIZ(I))
      AN2=-(VIX(IP)-VIX(I))*(VIZ(I+1)-VIZ(I))+(VIX(I+1)
     1  -VIX(I))*(VIZ(IP)-VIZ(I))
```

```
      GO TO 5013
510   AN1=-(VIX(IP)-VIX(I))*(VIY(IP+1)-VIY(IP))+(VIX(IP+1)
     1  -VIX(IP))*(VIY(IP)-VIY(I))
      AN2=-(VIX(IP)-VIX(I))*(VIY(I+1)-VIY(I))+(VIX(I+1)
     1  -VIX(I))*(VIY(IP)-VIY(I))
5013  T=AN1/DET
      TP=AN2/DET

C  Note that the possibility of overlap between segments not nearest neighbours at their terminal or head
C  points is permitted.
      IF((0.D0.LE.T.AND.T.LE.1.D0).AND.(0.D0.LE.TP.AND.TP.LE.1.D0))
     1  GO TO 511
      GO TO 501

C  Computing the coordinates of the crossing point on the tangent plane.  Note: the number of
C  overcrossings maximum is set to 300!
511             IC=ICROSS+1
      if(ic.gt.300)go to 5012
      QCROSS(IC,1)=VIX(I)+T*(VIX(I+1)-VIX(I))
      QCROSS(IC,2)=VIY(I)+T*(VIY(I+1)-VIY(I))
      QCROSS(IC,3)=VIZ(I)+T*(VIZ(I+1)-VIZ(I))

C  Computing components of the q-->I+1 and q-->IP.
      VJX=VIX(I+1)-QCROSS(IC,1)
      VJY=VIY(I+1)-QCROSS(IC,2)
      VJZ=VIZ(I+1)-QCROSS(IC,3)
      VKX=VIX(IP)-QCROSS(IC,1)
      VKY=VIY(IP)-QCROSS(IC,2)
      VKZ=VIZ(IP)-QCROSS(IC,3)

C  Computing the components of the vector product J X K.
      VPX=(VJY*VKZ-VJZ*VKY)
      VPY=(-VJX*VKZ+VJZ*VKX)
      VPZ=(VJX*VKY-VJY*VKX)
```

```
C  Checking for near parallelism (i.e., coincidence) between the overcrossing segments. PROD: Scalar
C  product with the viewing vector (normal to the tangent plane).  If the product is negative, then the
C  vectors are antiparallel, thus the J X K is clockwise oriented.
        PMOD=DSQRT(VPX**2+VPY**2+VPZ**2)
        PROD=VPX*XV+VPY*YV+VPZ*ZV
        IF(DABS(PROD).GT.ERROR)GO TO 512
        GO TO 501

C  Computing the distances of the projected points within the segments to the point in the tangent plane.
512     ICROSS=ICROSS+1

C  Checking here if the newly found crossing is degenerate to any previously computed one.  Degeneracy
C  level is put to be the same as the accuracy in the coordinates, i.e. 0.002 Aangstroem.
505     CONTINUE
501     CONTINUE
500     CONTINUE
5012    if(icross.gt.300) go to 5011
        sum(icross)=sum(icross)+1
        go to 33355
5011    write(6,*) ' There are more crossings than expected'

C  Note: in this version "5011" is never used since a number of overcrossings larger than 300 is stored in
C  summ(300).
33355   CONTINUE

C  Note that the results are evaluated over one hemisphere.
        do 3111 ij=0,300
                sum(ij)=sum(ij)/floated_itotal
3111    continue
        anav_ii(k_chain)=0.d0
        do 3120 ij=0,300
                aij=ij
3120    anav_ii(k_chain)=anav_ii(k_chain)+aij*sum(ij)
```

```
      amax(k_chain)=0.d0
      nmax(k_chain)=0
      do 3130 ij=0,300
            if(sum(ij).gt.amax(k_chain))go to 3140
            go to 3130
3140  amax(k_chain)=sum(ij)
      nmax(k_chain)=ij
3130  continue
C  Checking if all the chains in the configuration are computed
      if(k_chain.eq.N_chain)go to 1030
      go to 1010

C  Average intra-chain crossings over all n_chains (a_navii), and standard deviation in intra-chains
C  (sd_navii) (also adding the information for the asphericity)
1030  av_navii = 0.d0
      av_aspher = 0.d0
      av_nmax = 0.d0
      do kii=1,N_chain
            av_nmax = av_nmax + nmax(kii)
            av_navii = av_navii + anav_ii(kii)
            av_aspher = av_aspher + aspher(kii)
      enddo
      av_nmax = av_nmax/anchain
      av_navii = av_navii/anchain
      av_aspher = av_aspher/anchain
      sd_navii = 0.d0
      sd_nmax = 0.d0
      sd_aspher = 0.d0
      do kii=1,N_chain
            floated_nmax = nmax(kii)
            sd_navii = sd_navii + (anav_ii(kii) - av_navii)**2
            sd_nmax = sd_nmax + (floated_nmax - av_nmax)**2
            sd_aspher = sd_aspher + (aspher(kii) - av_aspher)**2
      enddo
```

```
      sd_navii = dsqrt(sd_navii/anchain)
      sd_nmax = dsqrt(sd_nmax/anchain)
      sd_aspher = dsqrt(sd_aspher/anchain)
3150  write(51,9011)kij,rg_av,rg_sd,ree_av,ree_sd,av_aspher,
     1  sd_aspher,av_navii,sd_navii,av_nmax,sd_nmax,rg(i_pivot_chain),
     2  ree(i_pivot_chain),aspher(i_pivot_chain),anav_ii(i_pivot_chain)
9011  FORMAT(1x,I4,1x,F7.3,2X,F6.3,2X,F7.3,2X,F6.3,2X,F6.4,2X,F6.4,1x,
     1  F7.3,1x,F6.2,1x,F7.3,1x,F7.3,1x,F7.3,2x,F7.3,2x,F6.4,1x,F7.3)
      write(52,9012)kij,rg(1),rg(2),rg(3),rg(4),rg(5),rg(6),rg(7),
     1  aspher(1),aspher(2),aspher(3),aspher(4),aspher(5)aspher(6),
     2  aspher(7),anav_ii(1),anav_ii(2),anav_ii(3),anav_ii(4),
     3  anav_ii(5),anav_ii(6),anav_ii(7)
9012  Format(1x,I4,14(F7.3,1x),1x,7(F8.4,2x))

C  Check if there's any other configuration or trajectory to include
      IF(kij.EQ.n_config)GO TO 3336
      GO TO 1020
3336  close(50)
      close(51)
      END
```

Appendix 3: Inter-chain Entanglement Calculations Program Code

This program (*allxs-scan-trajectory_version_with_interchain_overcrossings_for_the_pivot_Gustavo_v3_GENERALIZED.f*) reads the output from the trajectory generating program, **Appendix 1** and then evaluates the mean inter-chain entanglement between each chain and the specified pivot chain (section **2.3.2**). The random number generation subroutine was not included in the following code.

```
C ***************************************************************************
C          allxs.FOR: scan version to run on traject. files                 *
C        UPPSALA 1998: This version incorporates also the                   *
C                  aspher-scan.f into a single tabulation.                  *
C                                                                           *
C        (Program under development; experimental use)                      *
C         (c)  BY: G.A. ARTECA, 1993-1998, 1998-2017                        *
C                                                                           *
C             Department of Chemistry and Biochemistry                      *
C             Laurentian University                                         *
C             Sudbury, Ontario, Canada P3E 2C6.                             *
C ***************************************************************************
C Default dimensions:
C Number of monomers:              100.
C Number of crossings:             300.
C Number of chains:                20.
C Number of neighbour chains:      6.
      IMPLICIT REAL*8 (A-H,O-Z)
      CHARACTER*160 COMMAND,trajectory_file,analysis_file
      INTEGER*4 i2_seed

C  Note that beads are counted from bead 1 = anchor (old bead 0). Dimensions to 20 chains in total and for
C  up to 6 selected neighbours (7 counting the pivot chain).
      DIMENSION X(20,100),Y(20,100),Z(20,100),
     1  xpse(6,100),ypse(6,100),zpse(6,100),
     2  xx(100),yy(100),zz(100),
     3  VIX(100),VIY(100),VIZ(100),
```

```
     4    QCROSS(300,3),sum(6,0:300),
     5    anav_ij(6),n_length(7),
     6    ind_neigh(0:6),amax(6),nmax(6)

          write(6,*)' Enter the command file with all data (in quotes)'
          READ(5,*)COMMAND
          OPEN(UNIT=49,FILE=COMMAND,STATUS='UNKNOWN')
           read(49,*)n_chain
          read(49,*)n_conf
          read(49,*)n_traj
          do ilengths=1,n_chain
                    read(49,*)n_length(ilengths)
          enddo
          read(49,*)i_pivot_chain
                    ipiv=i_pivot_chain
          write(6,*)'Print index of chain acting as pivot: ',ipiv
          read(49,*)trajectory_file
          read(49,*)analysis_file

C  Enter seed for the randomized projections.
          read(49,*)itotal
          read(49,*)i2_seed

C  i_neighbours designates how many neighbour chains to i_pivot_chain will be analysed (up to 6
C  neighbours initially)
          read(49,*)i_neighbours
          do jind=1,i_neighbours
                    read(49,*)ind_neigh(jind)
          enddo

C  pivot chain is stored as index "0" in ind_neigh
                    ind_neigh(0)=ipiv
          CLOSE(49)
C  Introducing a counter for configurations to follow the
```

```
C  % of progress later
                kij=0
                i_progress = 10
        open(unit=50,file=trajectory_file,status='unknown')
        open(unit=51,file=analysis_file,status='unknown')
        write(51,*)'       ---------- Configurational interchain
    1   overcrossings averaged over all chains ----------'
        write(51,*)' '
        write(51,*)'Conf i1 Nav_ij1  i2  Nav_ij2 ...
    1   Nij_av SD_Nij   N*_av  SD_N* '

                ERROR=1.D-14
                PI=DACOS(-1.D0)

C  N_length1 is the number of monomer beads per chain (ipiv). N_length2 is the number of monomer
C  beads per neighbour. N_chain is the number of chains per configuration. N_conf*N_traj is the number
C  of configurations
        floated_itotal = itotal
        aneigh=i_neighbours
        n_config = n_conf*n_traj

C  Reading the current configuration kij: (N_length*N_chain) beads
1020            kij = kij + 1
        do i=1,n_chain
                ncl=n_length(i)
                do j=1,ncl
                        read(50,*)X(i,j),Y(i,j),Z(i,j)
                enddo
        enddo

C  Construction of i_neighbour pseudochains
                index=1
1022    do i=1,n_length(ipiv)
                xpse(index,i)=x(ipiv,i)
```

```
                ypse(index,i)=y(ipiv,i)
                zpse(index,i)=z(ipiv,i)
        enddo
        do ii=(n_length(ipiv)+1),
     1  (n_length(ipiv)+n_length(ind_neigh(index)))
                xpse(index,ii)=x(ind_neigh(index),ii-n_length(ipiv))
                ypse(index,ii)=y(ind_neigh(index),ii-n_length(ipiv))
                zpse(index,ii)=z(ind_neigh(index),ii-n_length(ipiv))
        enddo
        if(index.eq.i_neighbours)go to 1021
        index=index+1
        go to 1022

C  Index kij is the double counter for the total number of configurations (either in the same trajectory or in
C  different ones)
1021    do 1111 j=1,i_neighbours
           do 1111 i=0,300
                sum(j,i)=0.d0
1111    continue

C  Determine the geometrical centre of the pseudochain conformation (to be the centre of the sphere used
C  for projections): xc,yc,zc. Begin the scanning of pseudochains for the current kij config.
                index_nei = 1
1023    xc=0.d0
        yc=0.d0
        zc=0.d0

C  Centre of mass for pseudochain
        natp=n_length(ipiv)+n_length(ind_neigh(index_nei))
        anatp=natp
        DO 2 J=1,natp
                xc=xc+xpse(index_nei,j)
                yc=yc+ypse(index_nei,j)
                zc=zc+zpse(index_nei,j)
```

```
2       continue
        xc=xc/anatp
        yc=yc/anatp
        zc=zc/anatp

C  Current pseudochain is now shifted to the c.o.m.
        do 3 j=1,natp
                XX(J)=xpse(index_nei,j)-xc
                YY(J)=ypse(index_nei,j)-yc
                ZZ(J)=zpse(index_nei,j)-zc
3       continue

C  Find the radius of the smallest sphere, centered at the new origin, which encloses the pseudochain
C  completely. This R-span will then be used to computed the interchain crossings.
        Rspan=DSQRT(XX(1)**2+YY(1)**2+ZZ(1)**2)
        DO 4 J=2,natp
                S=DSQRT(XX(J)**2+YY(J)**2+ZZ(J)**2)
                IF(S.GT.Rspan)Rspan=S
4       CONTINUE
C  Estimation of progress
        jaz=100*kij/n_config
        if(jaz.eq.i_progress)write(6,*)'reached =',jaz,' %'
        if(jaz.eq.i_progress)i_progress=i_progress+10

C _____________________________________________________
C Beginning the analysis of interchain overcrossings with respect to the ipiv chain and its designated
C  neighbours. All calculations use now only XX,YY,ZZ
C _____________________________________________________
C  k_neigh counter for the number of neighbouring chains, up to i_neighbours. Chains are listed in
C  ind_neigh(with index=k_neigh), with ind_neigh(0) being the ipiv chain index. Project only the pivot
C  chain's beads and its selected neighbours to compute overcrossings. (Remember that ind_neight(0) is
C  the pivot chain!)
3335    DO 33355 IRAND=1,itotal
5553    RAND1=ran_2(I2_SEED)
```

```
      RAND2=ran_2(I2_SEED)

C  Marsaglia's algorithm: sphere centred at c.o.m. for ipiv
      rand11=1.d0-2.d0*rand1
      rand22=1.d0-2.d0*rand2
      xxx=rand11**2+rand22**2
      if(xxx.gt.1.d0)go to 5553
      xv=2.d0*Rspan*rand11*dsqrt(1.d0-xxx)
      yv=2.d0*Rspan*rand22*dsqrt(1.d0-xxx)
      zv=Rspan*(1.d0-2.d0*xxx)
2015  continue
202   AN=DSQRT(XV**2+YV**2+ZV**2)

C  The viewing direction is normalized to the radius of the sphere.
      AN=Rspan/AN
      XV=AN*XV
      YV=AN*YV
      ZV=AN*ZV

C  Project every point of the selected backbones to the tangent plane and perpendicular to the viewing
C  direction: focusing only on the pivot chain and its selected neighbours
350   IF(DABS(XV).LT.ERROR)GO TO 10
      C1=((YV/XV)**2+1.D0)
      C2=YV*ZV/XV**2
      C3=((ZV/XV)**2+1.D0)
      DETER=C1*C3-C2**2
      IF(DABS(DETER).LT.ERROR)GO TO 2002
      DO 5 J=1,natp
            CY=YY(J)-YV*XX(J)/XV+(Rspan/XV)**2*YV
            CZ=ZZ(J)-ZV*XX(J)/XV+(Rspan/XV)**2*ZV
            IF(DABS(CY).LT.ERROR.AND.DABS(CZ).LT.ERROR)WRITE(6,*)
     1      ' BEWARE OF HOMOGENEOUS SYSTEMS!'
            ANUM=CY*C3-C2*CZ
            VIY(J)=ANUM/DETER
```

```
                ANUM2=C1*CZ-C2*CY
                VIZ(J)=ANUM2/DETER
5       VIX(J)=(Rspan**2-YV*VIY(J)-ZV*VIZ(J))/XV
        GO TO 40
2002    DO 2003 J=1,natp
                ANUM3=(XX(J)-XV)*(Rspan**2/XV-XX(J))
     1          +(CY/C1-YY(J))*(YY(J)-YV)-ZZ(J)*(ZZ(J)-ZV)
     2          -YV*(XX(J)-XV)*CY/(XV*C1)
                DENOM=ZV*(XX(J)-XV)/XV+
     1          C2*(YY(J)-YV)/C1-(ZZ(J)-ZV)-YV*(XX(J)-XV)*CY/(XV*C1)
                IF(DABS(DENOM).LT.ERROR)STOP
                VIZ(J)=ANUM3/DENOM
                VIY(J)=(CY-C2*VIZ(J))/C1
2003    VIX(J)=(Rspan**2-YV*VIY(J)-ZV*VIZ(J))/XV
        GO TO 40
10      IF(DABS(YV).LT.ERROR)GO TO 20
        C4=((ZV/YV)**2+1.D0)

        DO 6 J=1,natp
                VIX(J)=XX(J)
                VIZ(J)=(ZZ(J)+(Rspan/YV)**2*ZV-ZV*YY(J)/YV)/C4
                VIY(J)=(Rspan**2-ZV*VIZ(J))/YV
6       CONTINUE
        GO TO 40
20      IF(DABS(ZV).LT.ERROR)STOP
        DO 7 J=1,natp
                VIX(J)=XX(J)
                VIY(J)=YY(J)
7               VIZ(J)=Rspan**2/ZV
40      CONTINUE

C  At this point, the backbones are transformed in a planar curve, in general with self-crossings stores in
C  the VIX,... vectors. The next section computes the vector of crossings indices, which gives the graph-
C  theoretical characterization of the projected curve. Start here the computation of vectors CROSS Index
```

```
C  I (do 500) scans the beads in the pivot chain Index IP (do 501) scans the beads of  neighbour chains.
                    ICROSS=0
          DO 500 I=1,(n_length(ipiv)-1)
            DO 501 IP=(n_length(ipiv)+1),(natp-1)

C  Crossing analyzed: i-->i+1 (in ipiv) with ip-->ip+1 (in neighbours). Note that one skips the case I:1-->2
C  and IP:1-->2 because these two bonds are parallel (and perpendicular to the surface). All other cases are
C  included.
          if(I.eq.1.and.IP.eq.(n_length(ipiv)+1))Go to 501
          DET=-(VIX(I+1)-VIX(I))*(VIY(IP+1)-VIY(IP))+
     1    (VIX(IP+1)-VIX(IP))*(VIY(I+1)-VIY(I))
          IF(DABS(DET).GT.ERROR)GO TO 510

C  Overcrossings cannot be computed for this view, since all points lie on a x=const or y=const plane.
C  Equations are solved for other pairs of variables.
          IF(DABS(VIX(I+1)-VIX(I)).LT.ERROR.AND.DABS(
     1    VIX(IP+1)-VIX(IP)).LT.ERROR)GO TO 5101
          IF(DABS(VIY(I+1)-VIY(I)).LT.ERROR.AND.DABS(
     1    VIY(IP+1)-VIY(IP)).LT.ERROR)GO TO 5102
          GO TO 501
5101      DET=-(VIZ(I+1)-VIZ(I))*(VIY(IP+1)-VIY(IP))+
     1    (VIZ(IP+1)-VIZ(IP))*(VIY(I+1)-VIY(I))
          IF(DABS(DET).LT.ERROR)GO TO 501
          AN1=-(VIZ(IP)-VIZ(I))*(VIY(IP+1)-VIY(IP))+
     1    (VIZ(IP+1)-VIZ(IP))*(VIY(IP)-VIY(I))
          AN2=-(VIZ(IP)-VIZ(I))*(VIY(I+1)-VIY(I))+
     1    (VIZ(I+1)-VIZ(I))*(VIY(IP)-VIY(I))
          GO TO 5013
5102      DET=-(VIX(I+1)-VIX(I))*(VIZ(IP+1)-VIZ(IP))+
     1    (VIX(IP+1)-VIX(IP))*(VIZ(I+1)-VIZ(I))
          IF(DABS(DET).LT.ERROR)GO TO 501
          AN1=-(VIX(IP)-VIX(I))*(VIZ(IP+1)-VIZ(IP))+
     1    (VIX(IP+1)-VIX(IP))*(VIZ(IP)-VIZ(I))
          AN2=-(VIX(IP)-VIX(I))*(VIZ(I+1)-VIZ(I))+
```

```
     1    (VIX(I+1)-VIX(I))*(VIZ(IP)-VIZ(I))
          GO TO 5013
510       AN1=-(VIX(IP)-VIX(I))*(VIY(IP+1)-VIY(IP))+
     1    (VIX(IP+1)-VIX(IP))*(VIY(IP)-VIY(I))
          AN2=-(VIX(IP)-VIX(I))*(VIY(I+1)-VIY(I))+
     1    (VIX(I+1)-VIX(I))*(VIY(IP)-VIY(I))
5013      T=AN1/DET
          TP=AN2/DET

C  Note that the possibility of overlap between segments not nearest neighbours at their terminal or head
C  points is permitted.
          IF((0.D0.LE.T.AND.T.LE.1.D0).AND.(0.D0.LE.TP.AND.TP.LE.1.D0))
     1    GO TO 511
          GO TO 501

C  Computing the coordinates of the crossing point on the tangent plane. Note: the number of
C  overcrossings maximum is set to 300!
511                 IC=ICROSS+1
          if(ic.gt.300)go to 5012
          QCROSS(IC,1)=VIX(I)+T*(VIX(I+1)-VIX(I))
          QCROSS(IC,2)=VIY(I)+T*(VIY(I+1)-VIY(I))
          QCROSS(IC,3)=VIZ(I)+T*(VIZ(I+1)-VIZ(I))

C  Computing components of the q-->I+1 and q-->IP.
          VJX=VIX(I+1)-QCROSS(IC,1)
          VJY=VIY(I+1)-QCROSS(IC,2)
          VJZ=VIZ(I+1)-QCROSS(IC,3)
          VKX=VIX(IP)-QCROSS(IC,1)
          VKY=VIY(IP)-QCROSS(IC,2)
          VKZ=VIZ(IP)-QCROSS(IC,3)

C  Computing the components of the vector product J X K.
          VPX=(VJY*VKZ-VJZ*VKY)
          VPY=(-VJX*VKZ+VJZ*VKX)
```

```
      VPZ=(VJX*VKY-VJY*VKX)

C  Checking for near parallelism (i.e., coincidence) between the overcrossing segments. C PROD: Scalar
C  product with the viewing vector (normal to the tangent plane). If the product is negative, then the
C  vectors are antiparallel, thus the J X K is clockwise oriented
      PMOD=DSQRT(VPX**2+VPY**2+VPZ**2)
      PROD=VPX*XV+VPY*YV+VPZ*ZV
      IF(DABS(PROD).GT.ERROR)GO TO 512
      GO TO 501
512           ICROSS=ICROSS+1

C  Checking here if the newly found crossing is degenerate to any previously computed one.
501   CONTINUE
500   CONTINUE
5012  if(icross.gt.300) go to 5011

C  Summing the number of crossings at the current view between the pivot chain and the current
C  neighbour.
      sum(index_nei,icross)=sum(index_nei,icross)+1.d0
      go to 33355
5011  write(6,*) ' There are more crossings than expected'
      stop

C  Finished with scanning all possible crossings within the current pseudochain at the current projection.
C  We move to the next projection point on the enclosing sphere.
33355 CONTINUE
      do 3111 ij=0,300
           sum(index_nei,ij)=sum(index_nei,ij)/floated_itotal
3111  continue
      anav_ij(index_nei)=0.d0
      do 3120 ij=0,300
           aij=ij
           anav_ij(index_nei)=anav_ij(index_nei)+
     1     aij*sum(index_nei,ij)
```

```
3120    continue
        amax(index_nei)=0.d0
        nmax(index_nei)=0
        do 3130 ij=0,300
                if(sum(index_nei,ij).gt.amax(index_nei))go to 3140
                go to 3130
3140    amax(index_nei)=sum(index_nei,ij)
        nmax(index_nei)=ij
3130    continue

C  Proceed now to construct the analysis for the next pseudochain
                index_nei=index_nei+1
        if(index_nei.gt.i_neighbours)go to 33356
        go to 1023

C  Average intra-chain crossings over all n_chains (a_navii), and standard deviation in intra-chains
C  (sd_navii) also adding the information for the asphericity.

33356   av_navij = 0.d0
        av_nmax = 0.d0
        do jnei=1,i_neighbours
                av_nmax = av_nmax + nmax(jnei)
                av_navij = av_navij + anav_ij(jnei)
        enddo
        av_nmax = av_nmax/aneigh
        av_navij = av_navij/aneigh
        sd_navij = 0.d0
        sd_nmax = 0.d0
        do jnei=1,i_neighbours
                floated_nmax = nmax(jnei)
                sd_navij = sd_navij + (anav_ij(jnei) - av_navij)**2
                sd_nmax = sd_nmax + (floated_nmax - av_nmax)**2
        enddo
```

```
      sd_navij = dsqrt(sd_navij/aneigh)
      sd_nmax = dsqrt(sd_nmax/aneigh)
      if(i_neighbours.eq.1)go to 4441
      if(i_neighbours.eq.2)go to 4442
      if(i_neighbours.eq.3)go to 4443
      if(i_neighbours.eq.4)go to 4444
      if(i_neighbours.eq.5)go to 4445
      if(i_neighbours.eq.6)go to 4446
      write(6,*)' Check the number of declared neighbours!'
      stop

4441  write(51,9011)kij,ind_neigh(1),anav_ij(1)
9011  format(I4,1x,I2,1x,F7.3)
      go to 4447
4442  write(51,9012)kij,ind_neigh(1),anav_ij(1),ind_neigh(2),
   1  anav_ij(2),av_navij,sd_navij,av_nmax,sd_nmax
9012  format(I4,1x,I2,1x,F7.3,2x,I2,1x,F7.3,
   1  54x,F7.3,1x,F6.3,2x,F7.3,1x,F6.3)
      go to 4447
4443  write(51,9013)kij,ind_neigh(1),anav_ij(1),ind_neigh(2),
   1  anav_ij(2),ind_neigh(3),anav_ij(3),
   2  av_navij,sd_navij,av_nmax,sd_nmax
9013  format(I4,1x,I2,1x,F7.3,2x,I2,1x,F7.3,
   1  2x,I2,1x,F7.3,
   2  40x,F7.3,1x,F6.3,2x,F7.3,1x,F6.3)
      go to 4447
4444  write(51,9014)kij,ind_neigh(1),anav_ij(1),ind_neigh(2),
   1  anav_ij(2),ind_neigh(3),anav_ij(3),ind_neigh(4),anav_ij(4),
   2  av_navij,sd_navij,av_nmax,sd_nmax
9014  format(I4,1x,I2,1x,F7.3,2x,I2,1x,F7.3,
   1  2x,I2,1x,F7.3,2x,I2,1x,F7.3,
   2  28x,F7.3,1x,F6.3,2x,F7.3,1x,F6.3)
      go to 4447
4445  write(51,9015)kij,ind_neigh(1),anav_ij(1),ind_neigh(2),
```

```
     1    anav_ij(2),ind_neigh(3),anav_ij(3),ind_neigh(4),anav_ij(4),
     2    ind_neigh(5),anav_ij(5),
     3    av_navij,sd_navij,av_nmax,sd_nmax
 9015    format(I4,1x,I2,1x,F7.3,2x,I2,1x,F7.3,
     1    2x,I2,1x,F7.3,2x,I2,1x,F7.3,2x,I2,1x,F7.3,
     2    16x,F7.3,1x,F6.3,2x,F7.3,1x,F6.3)
          go to 4447
 4446    write(51,9016)kij,ind_neigh(1),anav_ij(1),ind_neigh(2),
     1    anav_ij(2),ind_neigh(3),anav_ij(3),ind_neigh(4),anav_ij(4),
     2    ind_neigh(5),anav_ij(5),ind_neigh(6),anav_ij(6),
     3    av_navij,sd_navij,av_nmax,sd_nmax
 9016    format(I4,1x,I2,1x,F7.3,2x,I2,1x,F7.3,
     1    2x,I2,1x,F7.3,2x,I2,1x,F7.3,2x,I2,1x,F7.3,
     2    2x,I2,1x,F7.3,4x,F7.3,1x,F6.3,2x,F7.3,1x,F6.3)
          go to 4447

C  Check if there's any other configuration or trajectory to include
 4447    IF(kij.EQ.n_config)GO TO 3336
          GO TO 1020
 3336    close(50)
          close(51)
          END
```

Appendix 4: Two Chains Under Compression for Model in Figure 12

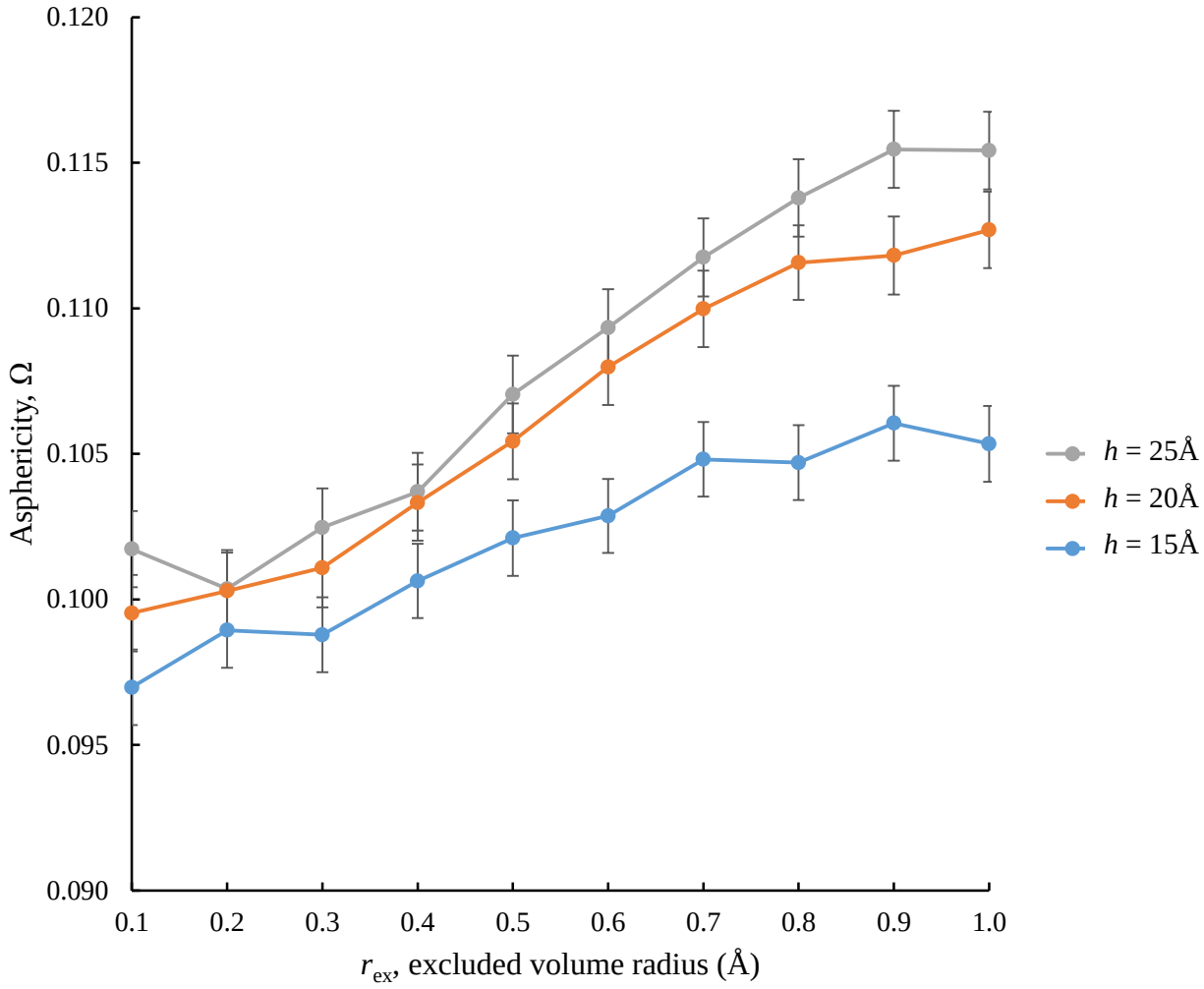

Figure 44: Asphericity of *n* = 50 beads per chain at various plate separation distances

The above figure is supplemental to section **3.1**, and examines how decreasing compression and increasing r_{ex} alters the shape of two chains grafted on opposite planes, and facing each other. For the three separations between plates, we observe that the asphericity increases with r_{ex}, indicating that the chains are swelling and becoming more prolate in shape. At lower compression (h = 20 and 25Å), the chains are somewhat more prolate than at h = 15 Å. This is likely due to the fact that larger compression brings the chains into closer proximity to each other, thus preventing the chains from becoming fully elongated along the z-axis, and instead twisting and bending onto themselves in order to lower repulsions. In all cases, we see a slowing down in the increase of Ω as a function of r_{ex}, which indicates that, in the presence of

compression, the configurational space is so highly reduced to prevent the swelling of a chain when the other one is too close.

Appendix 5: Two Shifted Chains Under Compression for Model in Figure 13

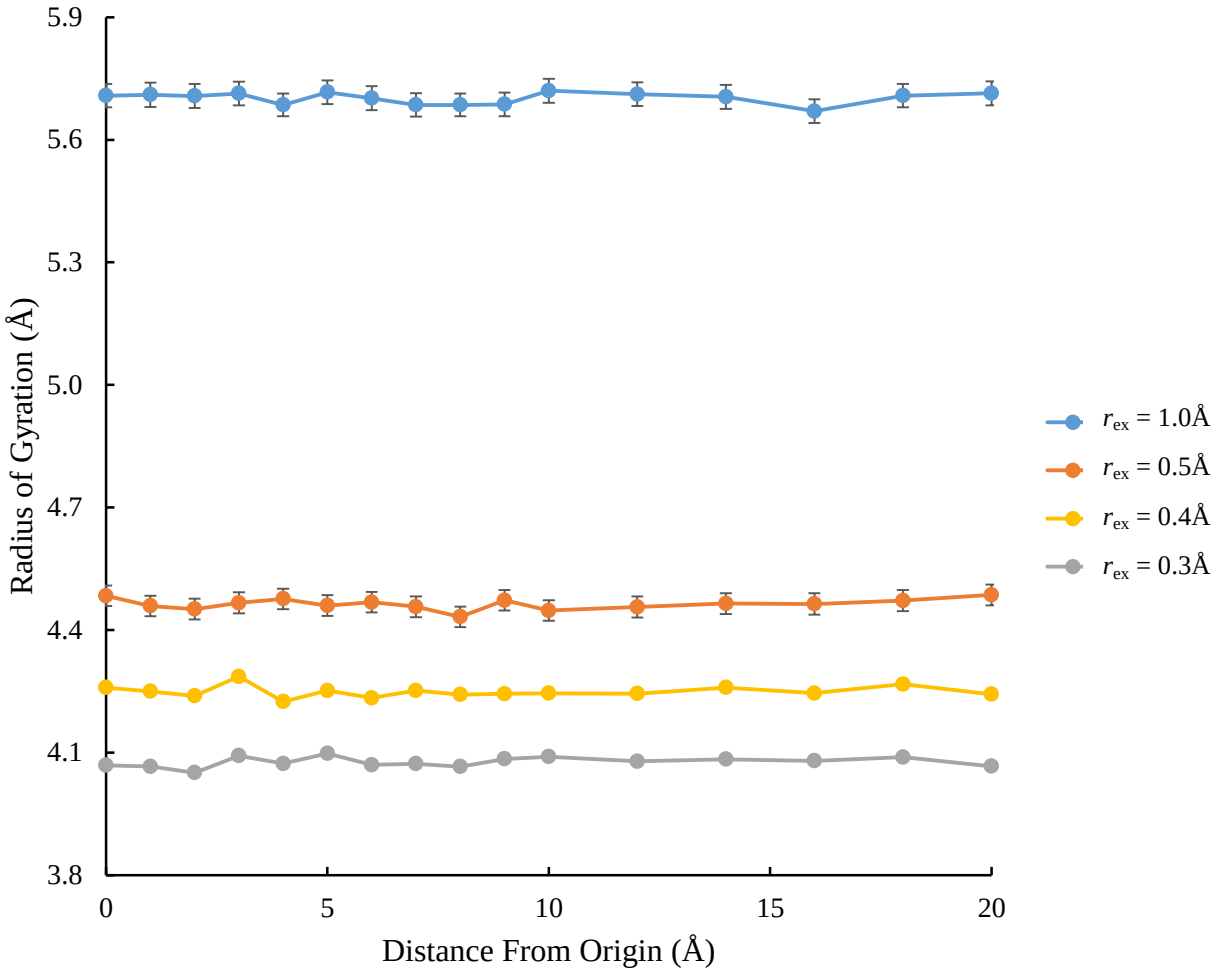

Figure 45: Radius of gyration of *n* = 50 beads per chain at *h* = 15Å at different r_{ex}-values.

The above figure is supplemental to section **3.2** and is an extension of **Figure 25** which compared the effects of shear displacement of compact on radius of gyration for chains with small and large excluded volume interaction (r_{ex} = 0.5Å and 0.1Å, respectively). As noted earlier, the intramolecular structure is unaffected by shear displacements; however, it is affected by excluded volume. Less swollen chains, such as those with r_{ex} = 0.3Å, resulted in the smallest mean chain size. As r_{ex} increases, the mean chain size increased accordingly.

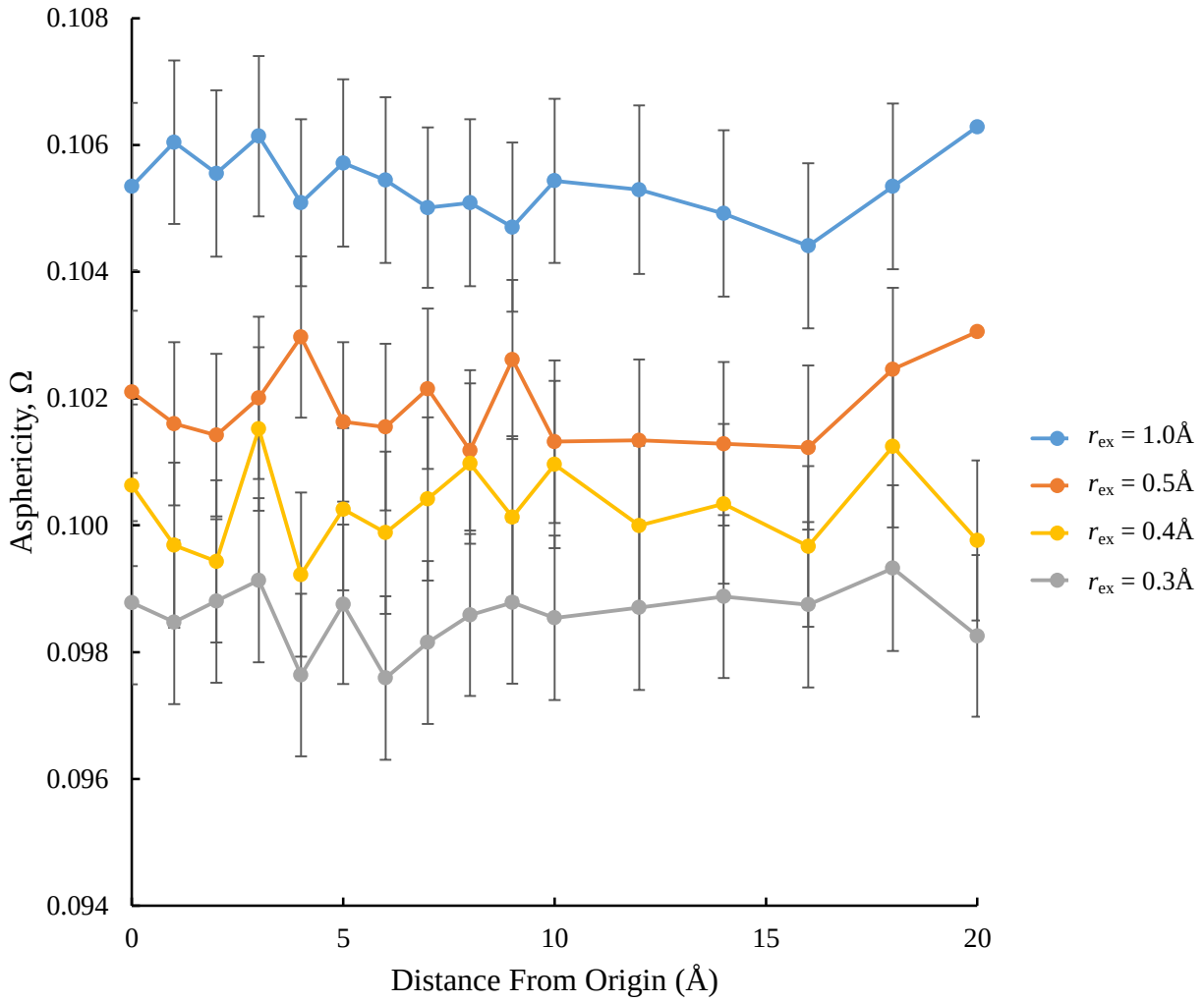

Figure 46: Asphericity of n = 50 beads per chain at h = 15Å at different r_{ex}-values (model in Figure 13).

The above figure supplements **Figure 45**, by comparing the effects of shear displacement on asphericity for chains with different levels of swelling. Like the radius of gyration, the structure is affected significantly by r_{ex}. As the chains increase in size (**Figure 45**), they also become more prolate (*i.e.*, less spherical) in shape.

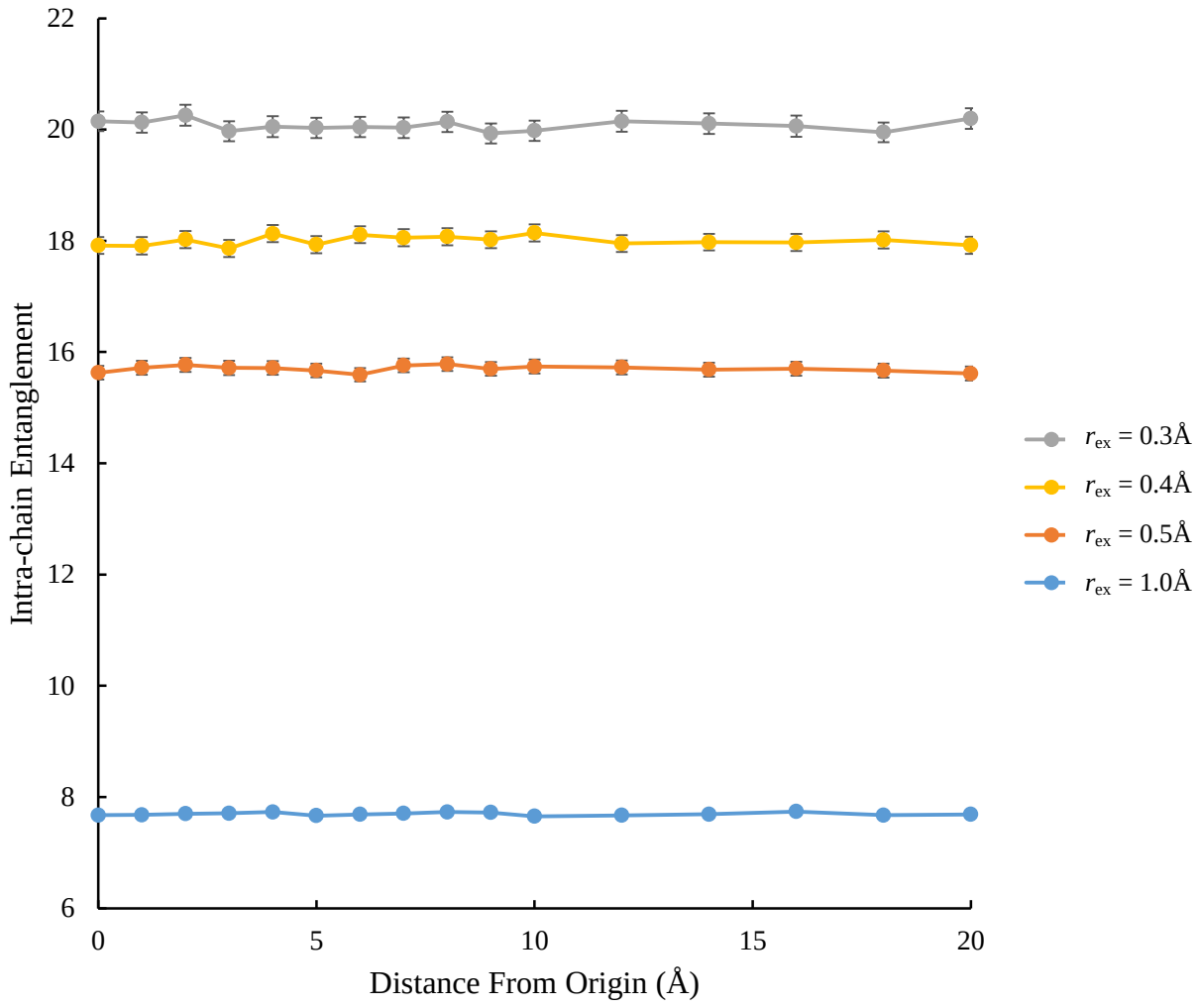

Figure 47: Intra-chain entanglement of n = 50 beads per chain at h = 15Å at different r_{ex}-values (model in Figure 13).

The above figure (like **Figure 46**) supplements **Figure 45**, by comparing the effects of shear displacement of intra-chain entanglement as a function of r_{ex}. As chains swell and stretch, they also untangle, leading to a decrease in intra-chain entanglement. As noted earlier, the intramolecular structure is unaffected by shear displacements, *i.e.*, despite the compression, the two chains find sufficient space to avoid each other by something resembling a rapid somewhat "rigid" rotation.

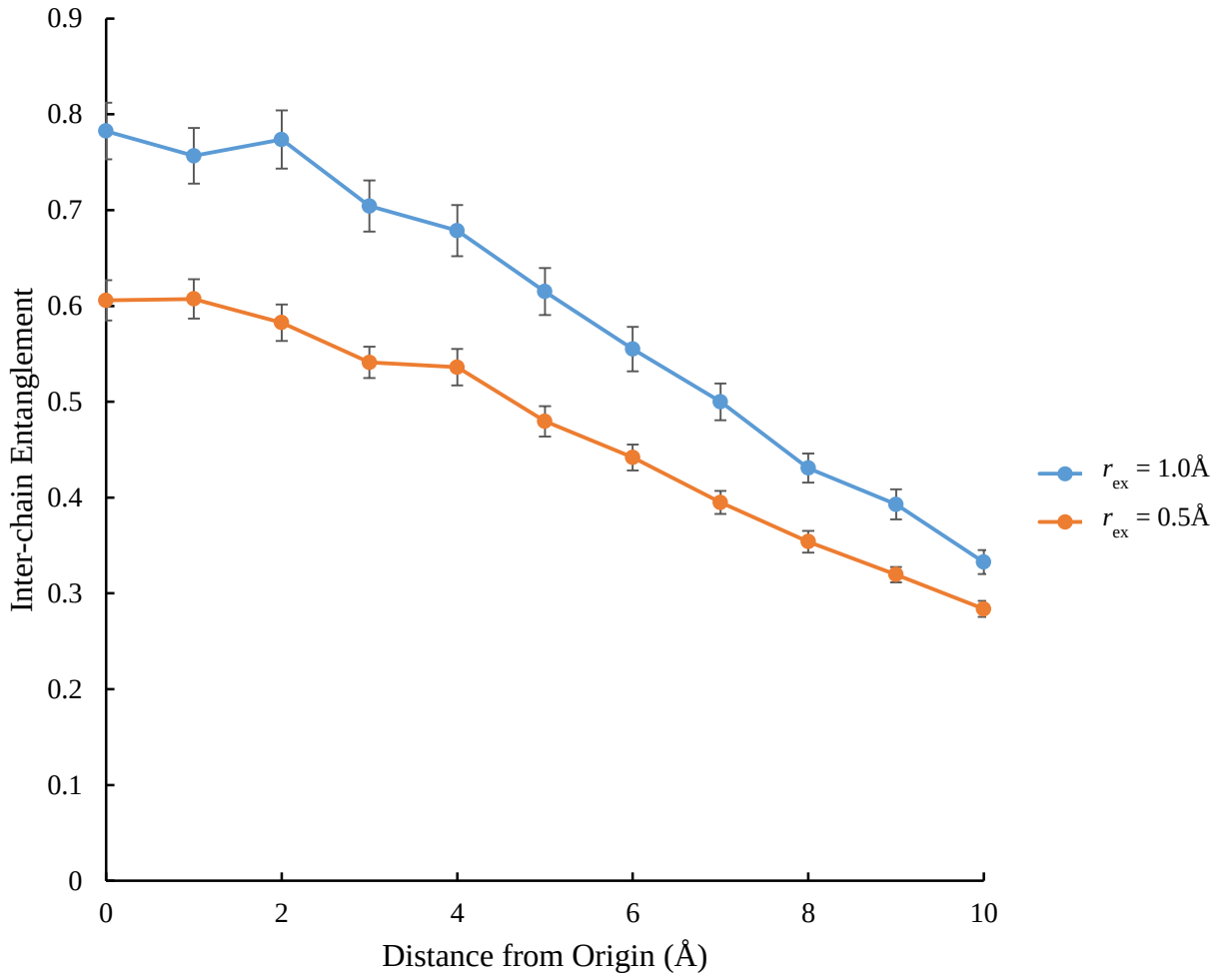

Figure 48: Inter-chain entanglement for two chains *n* = 20 beads per chain and *h* = 15Å, as a function of their relative displacement (model in Figure 13).

Figure 48 supplements section **3.2** and examines the effects of shear displacements on inter-chain entanglement for short chains (*n* = 20 beads per chains) at high compression. As in the case of the 30-bead chains (**Figure 27**), the less swollen chains (r_{ex} = 0.5Å) always entangle less than the more swollen chains (r_{ex} = 1.0Å), if the chains are sufficiently short.

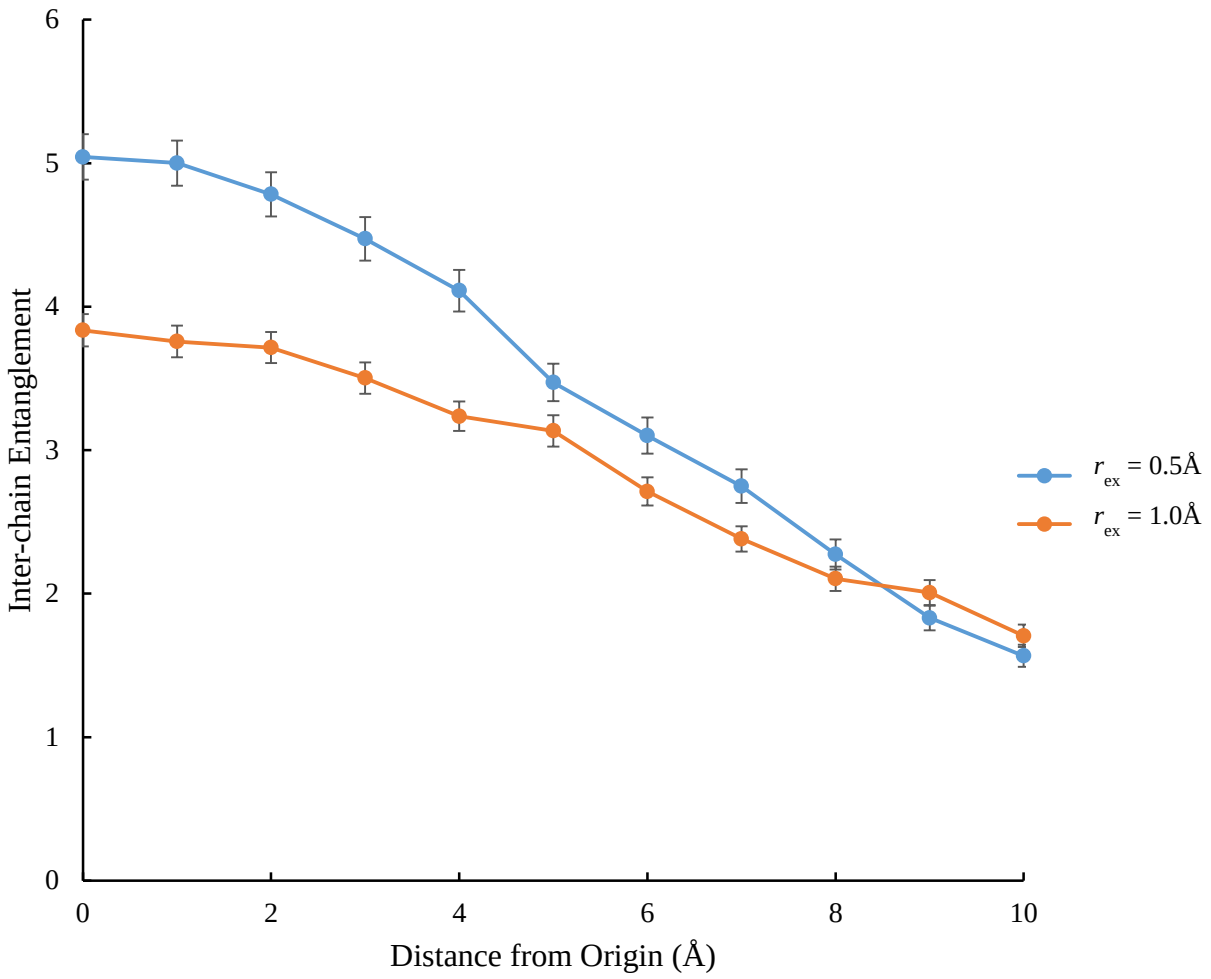

Figure 49: Inter-chain entanglement for two chains *n* = 30 beads per chain and *h* = 10Å, as a function of their relative displacement (model Figure 13).

The above figure supplements section **3.2** and examines the effects of shear displacements on inter-chain entanglement for shorter chains (*n* = 30 beads per chains) at high compression. Previously, in **Figure 27**, we showed that at *h* = 15Å, a 30-bead chain was too short for chain avoidance to occur and, as a result, did not display a crossover trend of more compact and swollen chains. When we increased the compression to *h* =10Å, the compact chains entangled more when they were grafted sufficiently close to each other (*i.e.*, $D \leq 8$Å), while at greater distances only the swollen chains entangled more.